DOE/ET-0065/2

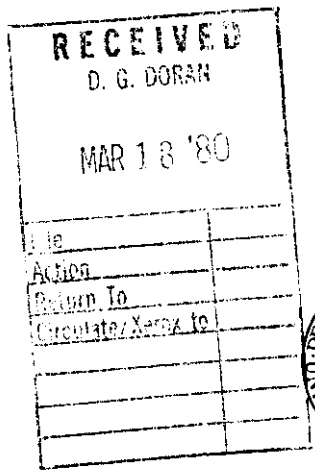

Damage Analysis and Fundamantal Studies

Quarterly Progress Report
January-March, 1978

May 1979

U.S. Department of Energy
Assistant Secretary for Energy Technology
Office of Fusion Energy

Department of Energy
Technical Information Center
PO. Box 62
Oak Ridge, Tennessee 37830

NOTICE OF CHANGE NUMBER ——— DATE 9-11-79

ITEM IDENTIFICATION:

DOE/ET-0065/2

Report No	Date of Report	Classification
DOE/ET-0065/3 DOE/ET-0065/4	May 1979	U

Author(s)

Originating Agency U. S. Department of Energy, Assistant Secretary for Energy Technology. Office of Fusion Energy

Title DAMAGE ANALYSIS AND FUNDAMENTAL STUDIES

INSTRUCTIONS:

The three reports above were issued with errors on the cover and title page in regard to the period of work covered by the reports. As printed all of the report titles indicate the incorrect period January-March 1978. The correct report periods should read as follows:

DOE/ET 0065/2 April - June 1978
DOE/ET 0065/3 July - September 1978
DOE/ET 0065/4 October - December 1978

Also the title contains a typographical error with "Fundamental" misspelled as "Fundamantal."

This is authority to make changes in documentary holdings as described above, and in records pertinent thereto. Changes in classification, security markings. etc., shuuld be made in accordance with the apprupriate DOE Security and Classification instructions.

Thomas B Abernathy

Thomas B. Abernathy, Chief
Document Control and
Evaluation Branch
Technical Information Center

Form TI-FL-14 (10-77)

DOE/ET-0065/2
uc-20. 20c

Qamage Analysis and Fundamantal Studies

Quarterly Progress Report
January-March, 1978

May 1979

U.S. Department of Energy
Assistant Secretary for Energy Technology
Office of Fusion Energy
Washington, DC 20545

Available from:

National Technical Information Service (NTIS)
U.S. Department of Commerce
5285 Port Royal Road
Springfield, Virginia 22161

Price: Printed Copy: $ 9.25
Microfiche: $ 3.00

FOREWORD

This report is the second in a series of Quarterly Technical Progress Reports on *"Damage Analysis and Fundamental Studies"* (DAFS) which is one element of the Fusion Reactor Materials Program, conducted in support of the Magnetic Fusion Energy Program of the U. S. Department of Energy. Other elements of the Materials Program are:

- *Alloy Development for Irradiation Performance (ADIP)*
- *Plasma-Materials Interaction (PMI)*
- *Special Purpose Materials (SPM).*

The DAFS program element is a national effort composed of contributions from a number of National Laboratories and other government laboratories, universities, and industrial laboratories. It was organized by the Materials and Radiation Effects Branch, Office of Fusion Energy, DOE, and a Task Group on *Damage Analysis and Fundamental Studies* which operates under the auspices of that Branch. The purpose of this series of reports is to provide a working technical record of that effort for the use of the program participants, for the fusion energy program in general, and for DOE.

This report is organized along topical lines in parallel to a Program Plan of the same title (to be published) so that activities and accomplishments may be followed readily relative to that Program Plan. Thus, the work of a given laboratory may appear throughout the report. Chapters 1 and 2 report topics which are generic to all of the DAFS Program: DAFS Task Group Activities and Irradiation Test Facilities, respectively. Chapters 3, 4, and 5 report the work that is specific to each of the subtasks around which the program is structured: A. Environmental Characterization, B. Damage Production, and C. Damage Microstructure Evolution and Mechanical Behavior. The Table of Contents is annotated for the convenience of the reader.

This report has been compiled and edited under the guidance of the Chairman of the Task Group on *Damage Analysis and Fundamental Studies*, D. G. Doran, Hanford Engineering Development Laboratory, and his efforts, those of the supporting staff of HEDL and the many persons who made technical contributions are gratefully acknowledged. T. C. Reuther, Materials and Radiation Effects Branch, is the Department of Energy counterpart to the Task Group Chairman and has responsibility for the DAFS Program within DOE.

Klaus M. Zwilsky, Chief
Materials and Radiation
Effects Branch
Office of Fusion Energy

CONTENTS

CONTENTS (Cont'd)

CONTENTS (Cont'd)

CONTENTS (Cont'd)

CONTENTS (Cont'd)

FIGURES

CHAPTER 3

FIGURES (Cont'd)

CHAPTER 3 (Cont'd)

CHAPTER 5 (Cont'd)

CHAPTER 5 (Cont'd)

CHAPTER 5 (Cont'd)

14 MeV Neutron Damage

CHAPTER 5 (Cont'd)

TABLES

CHAPTER 2

CHAPTER 3

TABLES (Cont'd)

CHAPTER 3 (Cont'd)

CHAPTER 5 (Cont'd)

CHAPTER 1

DAFS TASK GROUP ACTIVITIES

I. PROGRAM

Title: Irradiation Effects Analysis
Principal Investigator: D. G. Doran
Affiliation: Hanford Engineering Development Laboratory

II. OBJECTIVE

The objective of this work is to coordinate the activities of the DAFS Task Group.

III. RELEVANT DAFS PROGRAM PLAN TASK/SUBTASK

All tasks

IV. SUMMARY

DAFS Task Group activities have included participation in a FMIT Experimenters Review Panel, in the preparation of a FMIT dosimetry plan, and in defining nuclear data needs. Plans are being formulated for a program on fundamental mechanical behavior and workshops on microstructural characterization and on damage production modeling.

V. ACCOMPLISHMENTS AND STATUS

The DAFS Program Plan was completed and forwarded to DOE headquarters for printing.

The Task Group continued its involvement in activities related to the design of the Fusion Materials Irradiation Test (FMIT) facility to be built at HEDL. Several members participated in an ad hoc Experimenters Review Panel for FMIT on May 22-23 at HEDL. Subtask Group A, Environmental Characterization, continued to contribute to the development

of a document describing FMIT Dosimetry Program Requirements and Support Activities.

Subtask Groups A and B (Damage Production) continued to assist the Materials and Radiation Effects Branch, Office of Fusion Energy, in defining nuclear data needs ever more specifically and in addressing the means of obtaining needed data.

Subtask Group B has held preliminary discussions regarding a possible Fall workshop on computer modeling of damage production phenomena.

Subtask Group C (Damage Microstructure Evolution and Mechanical Behavior) has concentrated on implementing a program on fundamental mechanical behavior as outlined in the DAFS Program Plan. A major meeting on this topic is planned for July 13-14 at Richland, Washington, in conjunction with the 9th ASTM International Symposium on Effects of Radiation on Structural Materials. Also to be considereo at that time will be implementation of a proposal for a workshop on techniques for microstructural and microchemical examination.

CHAPTER 2

IRRADIATION TEST FACILITIES

I. PROGRAM

Title: Irradiation Effects Analysis
Principal Investigator: D. G. Doran
Affiliation: Hanford Engineering Development Laboratory

II. OBJECTIVE

The objective of this work is to develop a national program plan for the effective utilization of the RTNS-II and other high energy neutron facilities.

III. RELEVANT DAFS PROGRAM PLAN TASK/SUBTASKS

All tasks are relevant in that the utilization of high energy neutron sources is an integral part of the DAFS Program strategy. The tasks expected to be affected most directly are:

TASK II.A.2 High Energy Neutron Dosimetry
II.A.4 Gas Generation Rates
II.A.5 Dosimetry Technique Development
II.B.3 Experimental Characterization of Primary Damage State
II.B.4 Damage Production in Insulators
II.C.1 Effect of Material Parameters on Microstructure
II.C.2 Effect of Helium on Microstructure
II.C.6 Effect of Damage Rate and Cascade Structure Microstructure
II.C.7 Effect of Helium and Displacements on Flow
II.C.8 Effect of Helium and Displacements on Fracture
II.C.11 Effects of Cascades and Flux on Flow
II.C.18 Relating Low and High Exposure Microstructures

IV. SUMMARY

A draft of the RTNS-II Utilization Plan has been completed and circulated for comments.

V. ACCOMPLISHMENTS AND STATUS

A. RTNS-II Utilization Plan - R. W. Powell and D. G. Doran

1. Introduction

The Rotating Target Neutron Source - II (RTNS-11), under construction at Lawrence Livermore Laboratory (LLL), is expected to be at full power in January 1979. Funded by the Office of Fusion Energy, the RTNS-II will be the highest flux source of high energy neutrons in the world. Preparation of a program plan for the utilization of this facility was initiated and progress was reported in the previous quarterly.(1)

2. Status

Over 120 individuals were contacted in an effort to poll the community on the effective use of the RTNS-II. The responses are summarized in Table 1 as "Projected or Proposed Experiments for RTNS-II."

Table 1 and the DAFS Program Plan formed the basis for the RTNS-II Utilization Plan. A draft of the Plan has now been completed and sent to members of the fusion materials community for comment.

VI. REFERENCES

1. R. W. Powell and D. G. Doran, "RTNS-II Utilization Plan," DAFS Quarterly Report, April 1978, p. 10.

VII. FUTURE WORK

Responses to the draft RTNS-II Plan will be considered and a final version completed during the next reporting period.

VIII. PUBLICATIONS

None.

TABLE 1

SUMMARY OF PROJECTED OR PROPOSED RTNS-II EXPERIMENTS

Principal Investigator	Organization	Experiment Description	Experiment Objective	Desired Fluence, n/cm^2	Temperature	Planned Date, FY	DAFS Subtask
1. J.A. Spitznagel	W-R&D	Helium pre-doped specimens for atom probe, ion channeling and anelastic relaxation measurements	Kinetics and microstructural sensitivity of helium/point defect clustering	2×10^{17} - 1×10^{19}	300-700°C	81-83	II.C.2.1, II.C.18.1 2.2.,
2. R.H. Jones	BW	TEM and tensile tests of representative path A, B and C alloys	1 Comparison of energetic neutrons and light ions on microstructure evolution 2 Relationships between microstructure and mechanical properties	1×10^{17} - 5×10^{18}	20°C, 200-800°C	79-83	II.C.6.3, I 11.4
3. M.W. Guinan	LL	Resistivity increase and annealing of pure metals with a range of atomic weight and crystal structure.	Total defect production, including clusters, relative to fission spectra.	10^{17}	~270°	79-80	II.B.3.2
		Resistivity of ordered alloys	Free defect production through resistivity decrease and replacement production through resistivity increase	10^{17}	20°C-elevated	79-80	II.B.3.1, II.B.3.2
		TEM of pure metals with a range of atomic weight	Void nucleation relative to fission spectra	10^{18}-5×10^{19}	elevated	79-83	II.C.6.3, II.C.18.1
		Resistivity and magnetic measurements of alloys	Phase stability relative to fission spectra	10^{18}-5×10^{19}	elevated	79-83	II.C.1.1, II.C.6.3 II.C.18.1
4. L.R. Greenwood	ANL	Mapping studies of neutron fields and integral testing of activation data	Characterization of neutron field	10^{16}-10^{18}	20°C	79-83	II.A.2.1, II.A.2.2
5. G.L. Kulcinski	Univ. of Wisc.	Ion bombardment of pure metals following high energy neutron preconditioning	Assess the effect of high energy neutron preconditioning on the high fluence microstructure	10^{19}-10^{20}	20°C-700°C	80-83	II.C.18.2
6. F.V. Nolfi	ANL	Irradiation creep-stress relaxation measurements	Determine effect production rates		Elevated	81	II.B.3.2, II.C.2.3, II.C.7.3, II.C.11.4
7. J.A. Sprague	NRL	Superlattice darkfield TEM of ordered precipitates	Determine cascade size	-	-	-	II.B.3.1, II.B.3.2
8. M. Kirk	ANL	TEM and resistivity of ordered alloys	Concentration and size of cascade clusters and number of free defects	10^{17}-10^{18}	~270°C-20°C	79-81	II.B.3.1, II.B.3.2

TABLE 1 (Cont'd)

Principal Investigator	Organization	Experiment Description	Experiment Objective	Desired Fluence, n/cm^2	Temperature	Planned Date, FY	DAFS Subtask No.
9. K. Merkle	ANL	TEM and resistivity of pure metals including observation of surface crater formation	Concentration and size of cascade clusters and number of free defects-quantitative comparison with cascade theory. Comparison of crater formation with theory.	10^{16}-10^{13}	20°C	79-80	II.B.3.2
10. G.R. Odette	UCSB	Destructive, non-destructive and microstructural tests	Comparison with models to ascertain defect production parameters and selected physical, mechanical and microstructural properties	10^{17}-10^{19}	20°C-elevated	79-82	II.B.3.1, II.B.3.2 II.C.6.3, II.C.8.2 II.C.11.4
11. P.R. Okamoto	ANL	Near surface solute segregation	Free defect production rate	-	Elevated	-	II.B.3.1, II.B.3 =
12. H. Wiedersich	ANL	High energy neutron induced loop growth rates in pre-nucleated material	Free defect production rate and dislocation bias	10^{13}-10^{20}	Elevated	-	II.B.3.1, II.B.3.2
13. W.J. Gray	BNW	Irradiate graphite	Defect characteristics in graphite	10^{17} max.	20°C	79-80	II.B.3.2, II.C.6.3
14. J.B. Roberto/ R.R. Coltman	ORNL	Resistivity, TEM, and X-ray diffuse scattering on pure metals. Recovery following low temperature irradiation	1) Cascade size, defect density and influence of subthreshold events. 2) Relationship between target mass, damage energy and defect distribution.	10^{17}-10^{19}	-270°C-20°C	-	II.B.3.2
		Measure helium production rates and influence on swelling	Effect of helium on microstructure evolution	10^{13}-10^{19}	Elevated	-	II.C.2.1, II.C.2.2
		X-ray, resistivity and annealing following high energy neutron preconditioning and short charged particle irradiation	Growth of defect aggregates	-	20°C-Elevated	-	
15. S. Sekula	ORNL	Flux-pinning effects in annealed and cold-worked superconducting alloys.	Pinning strength of cascades and defect clusters		-270°C-20°C	-	II.B.3.2
		Degradation of T_c with fluence in A15 compounds	Test damage energy correlation	-	-270°C-20°C	-	II.B.3.2
		Degradation of stability of commercial composite superconducting materials.	Delineate engineering limits	-	-270°C	-	

TABLE 1 (Cont'd)

Principal Investigator	Organization	Experiment Description	Experiment Objective	F	mpe	Planned Date, FY	DAFS Subtask No.
16. Y. Chen	ORNL	Spectroscopic measurements of irradiated MgO	Determine anion vacancy and divacancy concentrations		0°C	-	II.B.3.3
17. J. Narayan	ORNL	X-ray and TEM of Cu, Nb and pure 316	Concentration, size and type of clusters		0°C 0°0	80	II.B.3.2
18. D. Parkin	LASL	Dislocation damping and Zener relaxation measurements made in-cell.	Free interstitial production cross-section		0°C lev	80-81	II.B.3.1, II.B.3.2
19. F.W. Clinard	LASL	TEM and optical absorption plus density, thermal diffusivity, microhardness and fracture toughness measurements of irradiated ceramics. Isochronal anneals.	Nature of point defects and aggregated defects in ceramics. Survey of changes in physical properties.		0°C	79	II.B.3.3, II.C.6.3
20. C.L. Snead	BNL	Incremental irradiations of superconductors	Superconductor property correlations between fission and high energy neutrons			79-83	II.B.3.2
		Positron sample irradiation	Determine void and bubble nucleation and growth with positron annihilation technique			79-83	II.C.6.3, II.C.18.1
21. K.H. Westmacott	LBL	High energy neutron irradiations and 1.5 MeV HVEM irradiations	Establish validity, limitations and advantages of simulation techniques to predict high fluence behavior			80	II.C.6.3
22. R.M. Scanlon	LLL	Superconductor specimen irradiation without warm-up	Determine the effects of high energy neutrons on the superconducting properties			80-81	II.B.3.2
23. R.R. Coltman, Jr.	ORNL	Mechanical and electrical properties of organic and composite insulators after high energy neutron irradiation and irradiation	Significance of high energy neutrons relative to fission neutrons and gamma radiation			80	-
24. O. Harling/ M.T. Thomas	MIT/BNW	Neutron sputtering yield experiment on atomically clean surfaces	Direct comparison with theoretical sputtering yields			79-80	II.B.3.2

TABLE 1(Cont'd)

Principal Investigator	Organization	Experiment Description	Experiment Objective	Desired Fluence, n/cm^2	Temperature	Planned Date, FY	DAFS Subtask No.
25. M. Kaminsky	ANL	Neutron sputtering yield experiments on EPR and demo-materials	Particle release and near surface alteration	1×10^{18}-5×10^{18}	200C	80	-
		Sputtering yield experiments with simultaneous high energy neutron and helium bombardment	Particle release and near surface alteration	1×10^{18}-5×10^{18}	200C	80	-
26. E.A. Henry	LLL	14 MeV neutron irradiation of ^{235}U followed by fast chemistry	14 MeV neutron induced fission to study nuclei in the "valley" of the fission distribution, yield as a function of neutron energy and fission nuclei with a threshold for neutron induced fission	-	200C	79-82	
		14 MeV neutron induced reactions	Production and study of heavy, neutron rich nuclei	-	200C	79-82	
27. P.K. Hopke	Univ. of Ill. at Urbana-Champaign	Irradiation of various materials including biological tissues, coal and coal ash with multielement comparator standards followed by rapid gamma ray spectroscopy	Development of a trace multielement analytical technique for analyses of many difficult to analyze elements	10^{14}-10^{17}	200C	80	
28. H. Farrar, IV	AI	Elemental and alloy irradiations followed by mass spectroscopic helium analysis	Determine helium generation rates. Measure neutron flux with HAFM's and development of technique	-	200C		II.A.2.1, II.A.2.2, II.A.4.2, II.A.5.2

TABLE 1 (Cont'd)

Principal Investigator	Organization	Experiment Description	Experiment Objective	Desired Fluence, n/cm^2	Temperature		
29. D.G. Doran	HEDL	High resolution TEM; pre-irradiation microstructure control; mechanical properties	Technique development for damage detection and separation of simultaneous processes	10^{17}-10^{18}	20°C-600°C		
		TEM microstructure characterization; hot microhardness	Determine damage production and microstructure evolution for comparison with models and fission data. Compare microstructure with mechanical properties.	10^{17}-10^{19}	-270°C-600°C	79-83	II.B.3.2, II.C.2.1, II.C.2.2, II.C.2.3, II.C.6.3, II.C.7.2, II.C.8.2, II.C.11.4, II.C.18.1

CHAPTER 3

SUBTASK A: ENVIRONMENTAL CHARACTERIZATION

I. PROGRAM

Title: Helium Generation in Fusion Reactor Materials
Principal Investigators: D. W. Kneff, Harry Farrar IV
Affiliation: Energy Systems Group, Rockwell International

II. OBJECTIVE

The objective of this work is to develop and apply helium accumulation fluence dosimetry to the measurement of neutron fluences and energy spectra in mixed-spectrum fission reactors utilized for fusion materials testing.

III. RELEVANT DAFS PROGRAM PLAN TASK/SUBTASK

TASK II.A.1	Fission Reactor Dosimetry
SUBTASK II.A.1.1	Flux-Spectral Definition in a Tailored Fission Reactor
SUBTASK II.A.1.2	Enhance Technique

IV. SUMMARY

An extensive set of helium accumulation fluence monitors was assembled for neutron dosimetry in the Magnetic Fusion Energy (MFE) irradiation experiment MFE-2 in the Oak Ridge Research Reactor (ORR). This set was sent to Argonne National Laboratory (ANL) for incorporation with their radiometric dosimeters for Levels 1-4 of the MFE-2 experimental assembly.

V. ACCOMPLISHMENTS AND STATUS

Helium Accumulation Fluence Dosimetry for the MFE-2 Irradiation in the Oak Ridge Research Reactor -- D. W. Kneff and Harry Farrar IV (Energy Systems Group, Rockwell International)

An extensive set of helium accumulation fluence monitors (HAFM's) was assembled for neutron dosimetry in the MFE-2 ORR irradiation. This set has been modified somewhat from the list of HAFM's presented in the previous DAFS Progress Report,[**]) due to design changes in the MFE-2 experimental assembly. The set consists of four groups of HAFM's, to be placed in a single sealed aluminum tube between the MFE-2 experiment holder assembly and the external experiment can, and extending from the top of Level 1 to the bottom of Level 4. One group of HAFM's will be centered approximately on the midplane of each level. The final set of HAFM's is listed in Table 1.

This HAFM set was sent to ANL to be incorporated with their radiometric wire dosimeters. The combined dosimetry will be in a close spatial geometry for optimum comparison of the two neutron dosimetry methods.

VI. REFERENCES

1. D. W. Kneff and H. Farrar IV, "Helium Generation in Fusion Reactor Materials," Contributions to the Damage Analysis and Fundamental Studies Periodic Technical Progress Report for the Period October 1977 to March 1978 (in press).

VII. FUTURE WORK

The irradiation of these HAFM's will be followed by their helium analysis in the Rockwell International high-sensitivity gas mass spectrometer. The results will be combined with the ANL results to provide dosimetry for the MFE-2 experiment, and will be combined with other similar sets of helium generation data to develop energy-dependent HAFM's for future mixed-spectrum fission reactor irradiations.

TABLE 1

FINAL HELIUM GENERATION DOSIMETER SET
FOR ORR IRRADIATION MFE-2

Material	Number of Specimens	Form*
TiN	4	Encapsulated powder
PbS	4	Encapsulated powder
KCl	4	Encapsulated crystals
CaF_2	4	Encapsulated crystals
FeF_2	4	Encapsulated crystals
V_2O_5	4	Encapsulated crystals
Be	1	Encapsulated crystals
^{54}Fe	1	Encapsulated chunks
KI	1	Encapsulated crystals
SiO_2	1	Encapsulated powder
Ni	4	Encapsulated wire
	3	Bare wire
V		Empty capsule
		Bare wire
Fe	4	Encapsulated wire
Ti	4	Bare wire
Al	4	Encapsulated wire
cu	4	Bare wire
Nb	3	Bare wire
Pt	3	Bare wire

* The capsules were made of vanadium, electron-beam welded in vacuum.

I. PROGRAM

Title: Dosimetry and Damage Analysis
Principal Investigator: L. R. Greenwood
Affiliation: Argonne National Laboratory

II OBJECTIVE

To determine the flux-spectrum at various locations in the Oak Ridge Reactor (ORR) and to provide dosimetry and damage analysis for MFE irradiation effects experiments.

III. RELEVANT OAFS PROGRAM TASK/SUBTASK

SUBTASK 11. A.l.l Flux-spectral definition in a tailored fission reactor.

IV. SUMMARY

Dosimetry plans have been completed for ORK-MFE2 to commence in July, 1978. The low-power spectral run will occur in late June or early July following the completion of ORR-MFE1. Foil or wire activation materials and helium accumulation fluence monitors (HAFM) are included in all runs.

V. ACCOMPLISHMENTS AND STATUS

Experiments at ORK -- L. R. Greenwood and R. R. Heinrich

The first irradiation in ORR labeled ORR-MFE1 is scheduled to end prematurely in late June or early July. Due to the reduced fluence it is not certain that the activation will be adequate in all materials and the HAFM's may not have sufficient helium for reliable counting at Atomics

International (AI). Selected samples will thus be counted to determine the extent of our effort.

The low-power spectral study is scheduled for an irradiation during July. The dummy capsule will be inserted in the same loaction to be used for ORR-MFE2. ANL personnel will unload the capsules at Oak Ridge (ORNL) and ship the samples to Argonne for counting within a few days after the end of irradiation in order to see the activities with short half-lives.

Plans have been completed for ORR-MFE2. Dosimetry wires (Fe, Ni, Ti, and Co-Al) have been packaged in small aluminum capsules (~.045" diameter by 0.25" long) and sent to OKNL. These capsules will be placed in small holes drilled in the thermocouple supports in each of the sixteen materials capsules on levels 1 - 4. A single tube will contain all four wires and HAFM materials will be loaded in a separate tube. Both tubes will run the entire length of the assembly to map fluence gradients. The irradiation is scheduled to start in late July and should last about one year.

VI. REFERENCES

None

VII. FUTURE WORK

Plans are now being initiated for ORR-MFE3 to start in October. Data analysis should extend well into FY80.

I. PROGRAM

Title: Dosimetry and Damage Analysis
Principal Investigator: L. R. Greenwood
Affiliation: Argonne National Laboratory

11. OBJECTIVE

To develop dosimetry techniques and provide dosimetry and damage analysis for experiments in Be(d,n) irradiation facilities.

111. RELEVANT DAFS PROGRAM PLAN TASK/SUBTASK

SUBTASK II.A.2.1 Flux-spectral definition in Be(d,n) field

IV. SUMMAKY

Results are presented for integral activation cross-section tests conducted at the Oak Ridge Isochronous Cyclotron (ORIC) using the $^{9}Be(d,n)$ reaction at E_d = 40 MeV. Unfolded spectra agree very well with measured time-of-flight spectra with overall standard deviations of about ±10% indicating that our extrapolated cross-section library is surprisingly accurate.

V. ACCOMPLISHMENTS AND STATUS

Inteqral Cross-section resting in a $^{9}Be(d,n)$ Field at E_d = 40 MeV --

L. R. Greenwood and R. R. Heinrich (ANL), M. J. Saltmarsh (ORNL).

Integral neutron activation measurements have been completed for 14 materials (44 reactions) in the 40 MeV $^{9}Be(d,n)$ field at ORIC. Foils were irradiated in a well-defined geometry at 7.62 cm from the neutron source at angles of 0° and 15° to the beam direction. Available cross-

sections have been extrapolated to 44 MeV for 29 of the reactions. The neutron spectra at various angles have been previously measured by M. Saltnarsh, *et. al.*[1] using the time-of-flight technique. Our activation measurements are compared to activities calculated using the time-of-flight spectra and our extended cross-section library in Table 1. As can be seen, the overall agreement of about ±10% is surprisingly good.

The second column indicates the 90% energy limits for the calculated activities. The good agreement between measured and calculated results comes mainly from the fact that we are generally testing the cross-sections at energies where they are better known. The large discrepancies for the (n,p) reactions on ^{46}Ti, ^{47}Ti, and ^{54}Fe are due to contributions from higher mass isotopes. The numbers in parentheses show that these effects are very nearly accounted for using the THRESH code of S. Pearlstein (BNL).[2]

Figures 1 and 2 compare the spectra at 0" and 15" unfolded with the SAND II code with the time-of-flight measurements. The slight differences are generally within the experimental accuracies of both techniques.

The excellent results obtained in a well-defined geometry indicate that spectral analysis in a poorly defined geometry should be reasonably reliable. The SAND II code was thus used to unfold the flux-spectrum obtained from thin Au, Ni, Co, and Fe foils placed directly on the tantalum end plate approximately 6.25 mm from the neutron source. The foils were placed in a cross pattern and cut into 14 subsections (typically 6.2 mm square) to map flux and spectral gradients. Eleven reactions, which showed excellent agreement in Table 1, were used to unfold the flux as a function of radial distance from the beam axis, as shown in figure 3. The agreement between foils located in all four directions normal to the beam axis indicates that the field is cylindrically symmetric and that the unfolding technique is quite reproducible.

TABLE I: RATIOS OF MEASURED-TO-CALCULATED ACTIVITIES ($\overline{\sigma\phi}$) USING TIME-OF-FLIGHT SPECTRA. RELATIVE ERRORS ARE 1.5% ABSOLUTE ± 10%, EXCEPT AS NOTED.

REACTION	90% Energy[a] Range (MeV)	Ratio at 0" (~3.5°)	Ratio at 15" (~17°)
	(0° Spectrum)		
$^{45}Sc(n,\gamma)^{46}Sc$	7.6^{-3}-25.0	1.00[b]	1.17[b]
$^{59}Co(n,\gamma)^{60}Co$	1.6^{-4}-22.7	1.26[b] ±10%	1.35[b] ±10%
$^{197}Au(n,\gamma)^{198}Au$	2.5^{-4}-19.5	1.03[b]	1.10[b]
$^{238}U(n,\gamma)^{239}Np$	4.3^{-4}- 4.2	1.02[b]	0.88[b]
$^{235}U(n,f)$	0.6 - Z9.7	0.99[c]	0.94
$^{238}U(n,f)$	5.0 - 30.8	1.00[c]	0.94
$^{115}In(n,n')^{115m}In$	1.8 - 23.1	1.04	0.96
$Ti(n,p)^{46}Sc$	9.0 - 33.0	*1.84 (0.83)[d]	*1.93 (0.88)[d]
$Ti(n,p)^{47}Sc$	12.0 - 33.0	*8.82 (1.18)[d]	*7.14 (1.13)[d]
$^{48}Ti(n,p)^{48}Sc$	9.9 - 26.6	0.97	u.99
$Fe(n,p)^{54}Mn$	6.0 - 33.0	*1.89 (0.94)[d]	*1.88 (1.04)[d]
$^{56}Fe(n,p)^{56}Mn$	8.6 - 23.5	1.05	1.02
$^{59}Co(n,p)^{59}Fe$	8.1 - 24.2	0.85 ±15%	0.95 ±15%
$^{58}Ni(n,p)^{58}Co$	4.4 - 23.4	0.93	0.88
$^{60}Ni(n,p)^{60}Co$	7.9 - 23.0	0.97 ± 5%	0.98 ± 7%
$^{27}Al(n,\alpha)^{24}Na$	9.0 - 21.5	1.02	0.56
$^{54}Fe(n,a)^{51}Cr$	9.5 - 28.0	*1.28	*1.43
$^{59}Co(n,\alpha)^{56}Mn$	9.3 - 24.4	1.05	1.02
$^{45}Sc(n,2n)^{44m}Sc$	13.9 - 27.5	0.95	0.98
$^{59}Co(n,2n)^{58}Co$	12.8 - 26.6	1.06	1.04
$^{58}Ni(n,2n)^{57}Ni$	14.8 - 28.2	0.82 (1.26)[e]	0.84 (1.34)[e]
$^{90}Zr(n,2n)^{89}Zr$	14.1 - 28.1	0.99	1.02
$^{93}Nb(n,2n)^{92m}Nb$	11.2 - 22.0	0.93	0.94

TABLE I (cont'd)

$^{169}Tm(n,2n)^{168}Tm$	10.4 - 23.3	0.91	0.92
$^{169}Tm(n,3n)^{167}Tm$	17.9 - 30.6	1.05	1.08
$^{197}Au(n,2n)^{196}Au$	10.7 - 23.5	0.99	0.98
$^{197}Au(n,3n)^{195}Au$	18.0 - 29.4	0.87 ± 4%	1.06 ± 7%
$^{197}Au(n,4n)^{194}Au$	27.2 - 39.8	1.03 ±10%	0.88 ±13%
$^{238}U(n,2n)^{237}U$	7.7 - 16.4	1.21	1.10
Std. Dev. (%)		*9.7	*10.8
Total Flux (n/cm^2-sec)		6.26 x 10^{10}	3.21 x 10^{10}

*Reactions not included in standard deviation.

[a]90% of the activation integral falls within this energy range. 7.6^{-3} means 7.6 x 10^{-3}. The range at '15" is only slightly changed.

[b](n,γ) ratios are somewhat arbitrary since the time-of-flight data stops at 2 MeV. A smooth extrapolation was chosen to give a reasonable fit to the data.

[c]14 MeV fission yields were used.

[d]Ratios not in parentheses were calculated assuming mono-isotopic production [e.g. $^{54}Fe(n,p)$]; ratios in parentheses include production from higher mass isotopes based on THRESH calculations. Energy limits are for total production.

[e]Cross-section from ENDF/B-IV and LASL; values in parentheses from ENDF/B-IV Only.

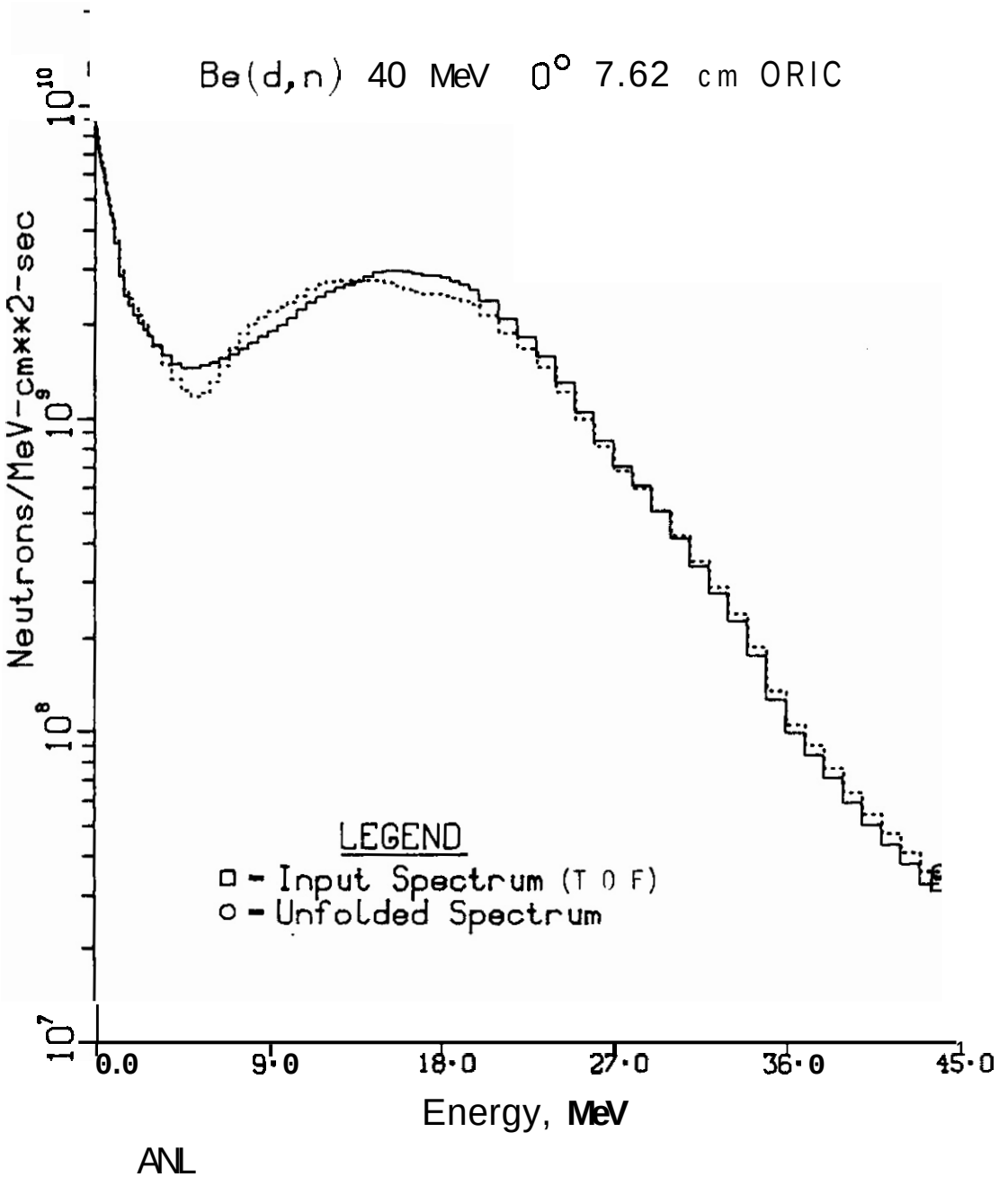

FIGURE 1. **Comparison of time-of-flight (input) spectrum at 40 MeV at 0" and unfolded spectrum from SAND II using our integral activities.**

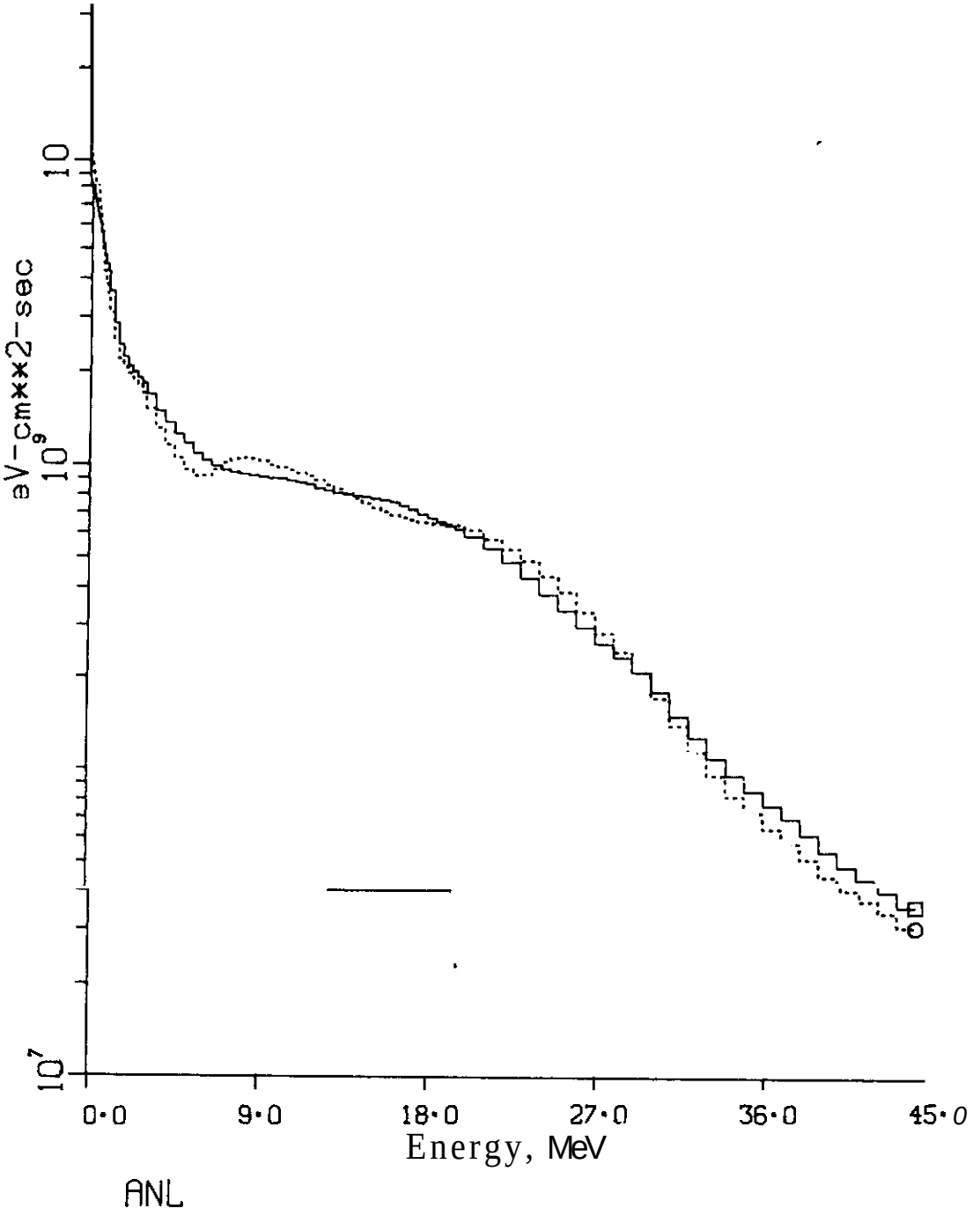

FIGURE 2. Comparison of time-of-flight (input) spectrum at 40 MeV at 15" and unfolded spectrum from **SAND** II using our integral activities.

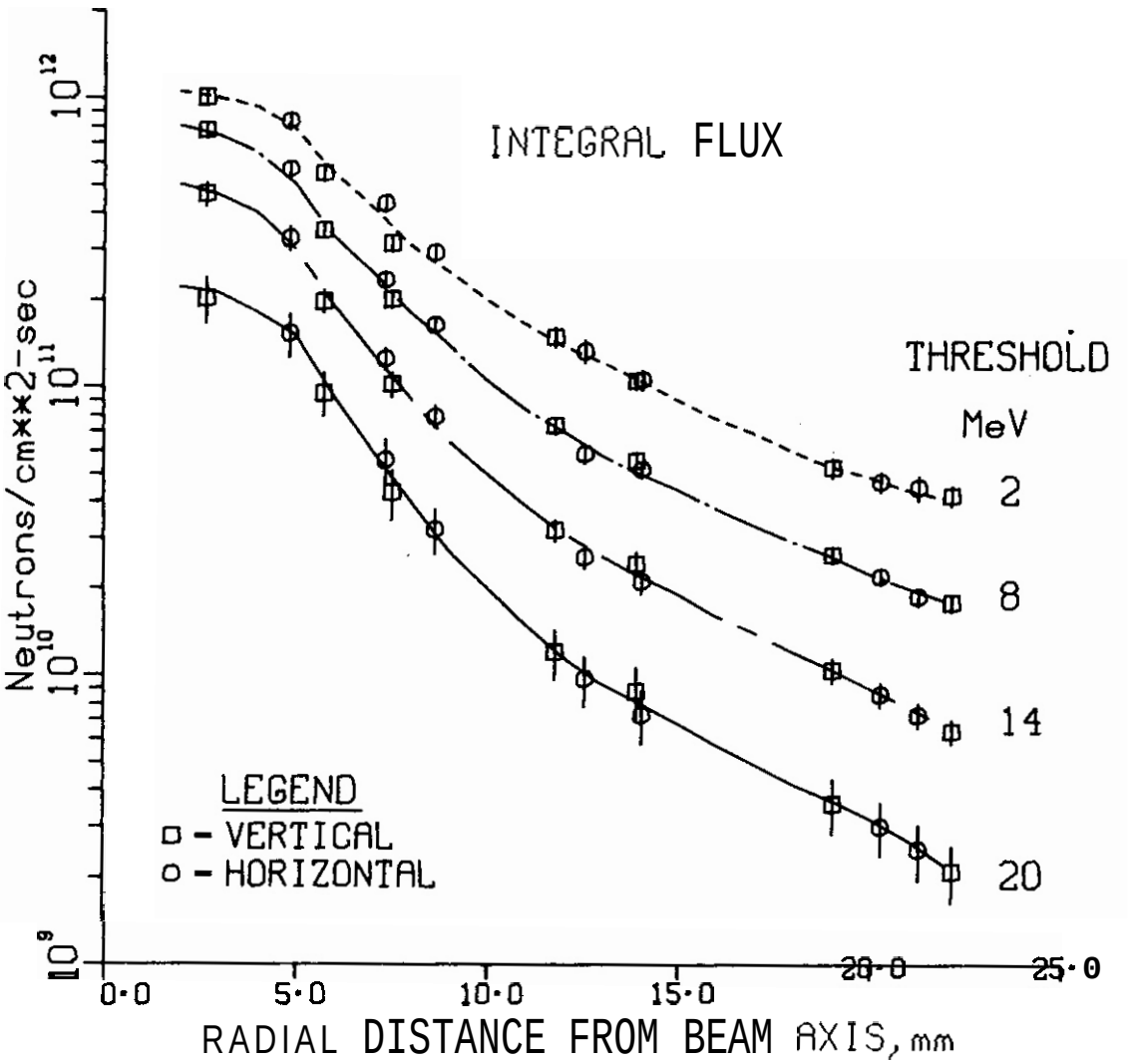

FIGURE 3. Integral radial flux gradients at 6.3 mm from the source unfolded with **SAND II** using our integral activity measurements. Various lower energy thresholds are indicated and errors were calculated with the Monte Carlo code **SANDANL.**

An unfolded spectrum obtained trom the centermost group of foils is shown with an error analysis in figure 4. This spectrum and figure 3 are of particular interest since it represents the maximum flux obtainable at ORIC for materials irradiations.

The errors shown in figure 4 indicate that the flux-spectrum is reasonably well-defined between 4 - 30 MeV where most of the materials damage originates. In a pure 0" spectrum, about 14%of the flux lies below 2 MeV, 9% is above 25 MeV, and only 3.5% is above 30 MeV. Hence, the larger flux errors at very low and very high energies are relatively unimportant in terms of neutron damage in materials.

A draft of our complete study is now being readied for submission to Nuclear Technology and preprints should be available shortly.

VI. REFEKENCES

1. M. J. Saltmarsh, C. A. Ludemann, C. B. Fulmer, and R. C. Styles, ORNL/TM-5696, 1976.

2. S. Pearlstein, BNL16271, 1971

VII. FUTURE WOKK

We plan to continue these integral tests at other deuteron energies in order to obtain a more complete picture of the accuracy of nuclear cross-sections. Development work is particularly important at very high and very low neutron energies where unfolded spectra have the largest errors at present.

VIII. PUBLICATIONS

A manuscript is now being prepared for submission to Nuclear Technology. Our extended cross-section file will be published in an ANL report.

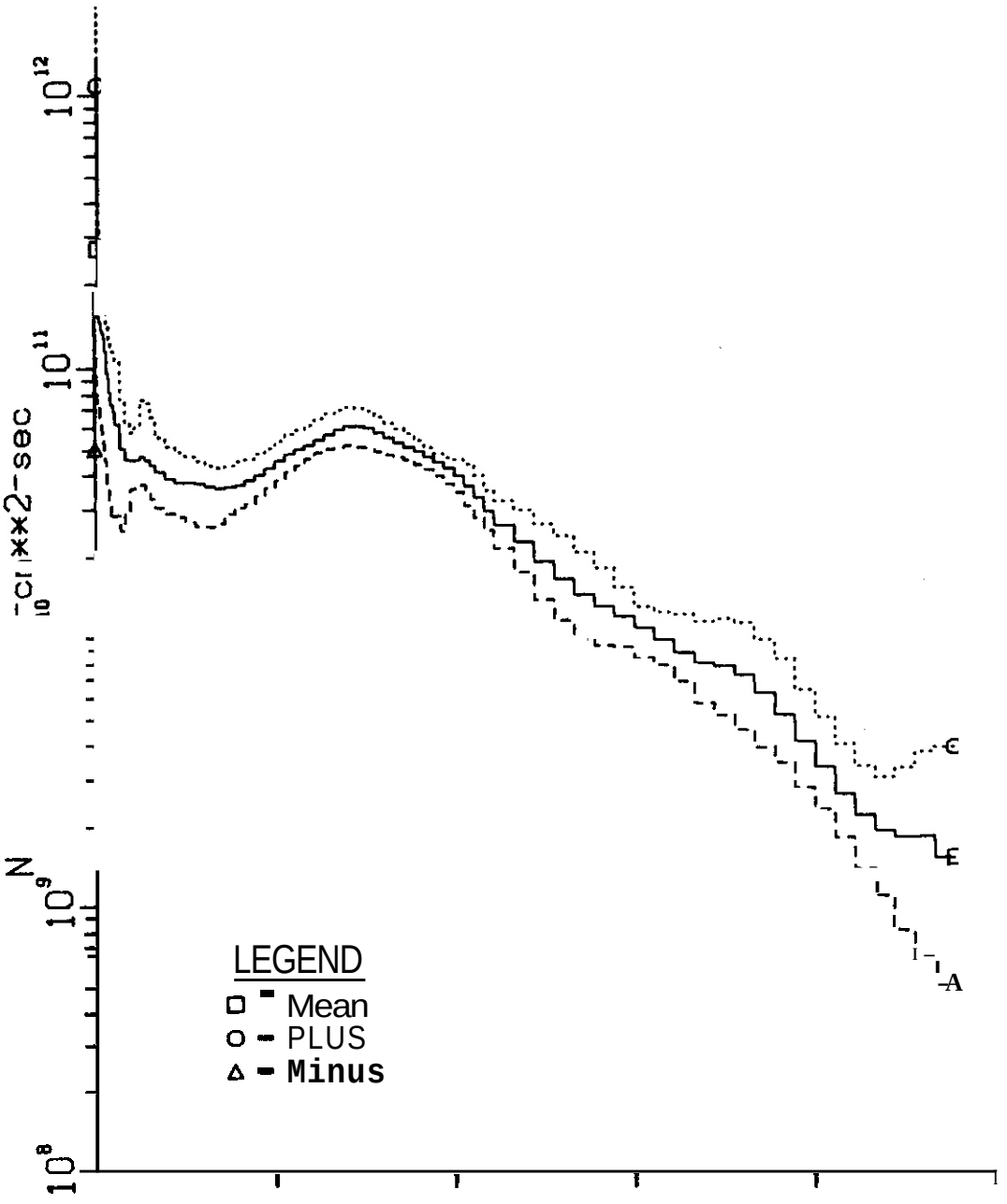

FIGURE 4. **Unfolded spectrum with error analysis at closest available geometry at ORIC. This position offers the maximum possible flux for materials irradiations.**

I. PROGRAM

Title: Helium Generation in Fusion Reactor Materials
Principal Investigators: D. W. Kneff, Harry Farrar IV
Affiliation: Energy Systems Group, Rockwell International

II. OBJECTIVE

The objectives of this work are to measure helium generation rates of materials for Magnetic Fusion Reactor applications in the broad-band Be(d,n) neutron environment, to characterize the Be(d,n) neutron fluence and energy spectra, and to develop helium accumulation fluence monitors for neutron fluence and energy spectrum dosimetry for fusion-program neutron irradiations.

III. RELEVANT DAFS PROGRAM PLAN TASK/SUBTASK

SUBTASK II.A.2.1	Flux-Spectral Definition in the Be(d,n) Field
SUBTASK II.A.4.3	Be(d,n) Helium Gas Production Data
SUBTASK II.A.5.1	Helium Accumulation Monitor Development

IV. SUMMARY

Helium analyses have been initiated for the pure elements irradiated in July 1977 in the Be(d,n) neutron field for 30-MeV deuterons. The analyses completed to date, include 29 specimens from five pure element wire rings (Al, Fe, Ni, and Cu) incorporated in the experiment for both cross section and helium accumulation dosimetry applications.

V. ACCOMPLISHMENTS AND STATUS

Helium Analyses of Be(d,n) - Irradiated Pure Elements -- D. W. Kneff, Harry Farrar IV, and M. M. Nakata (Energy Systems Group, Rockwell International)

A complex assembly of helium-generation and neutron dosimetry materials was irradiated in July 1977, using the Be(d,n) reaction with 30-MeV deuterons from the Crocker Nuclear Laboratory cyclotron at the University of California at Davis. The primary objectives were to measure the spectrum-integrated helium-generation cross sections of a large number of pure elements, separated isotopes, and alloys of potential fusion reactor design interest; to characterize the Be(d,n) neutron environment in detail; and to evaluate and use helium accumulation materials as neutron fluence and energy dosimeters. The experiment was undertaken jointly with personnel from Argonne National Laboratory (ANL) and Lawrence Livermore Laboratory (LLL), who are providing extensive radiometric characterization dosimetry for the irradiation.

The experiment has been described in detail elsewhere.(1) The helium-generation materials were contained in the irradiation capsule shown schematically in Figure 1. It was mounted 1 cm from the downstream face of the beryllium target assembly, and consisted of multiple layers of helium dosimetry materials sandwiched between layers of radiometric dosimetry foils. The eleven Au, Ni, Al, Fe, and Cu wire rings (Figure 1), irradiated concentric with the capsule axis, will provide most of the helium accumulation neutron dosimetry for the capsule volume. The first samples to be analyzed for helium in this experiment were taken from these dosimetry rings.

The rings were prepared for helium analysis by acid etching to reduce possible a-recoil surface effects to $<1\%$, and by segmenting each ring into multiple pieces for individual analysis. This segmenting procedure will provide detailed information on the neutron spectrum profile. The use of this technique has been demonstrated for the 14.8-MeV neutron field of the Rotating Target Neutron Source (RTNS-I) at LLL.(2)

Table 1 presents the helium results for 29 segments of five of the wire rings, which were analyzed using the Rockwell International high-

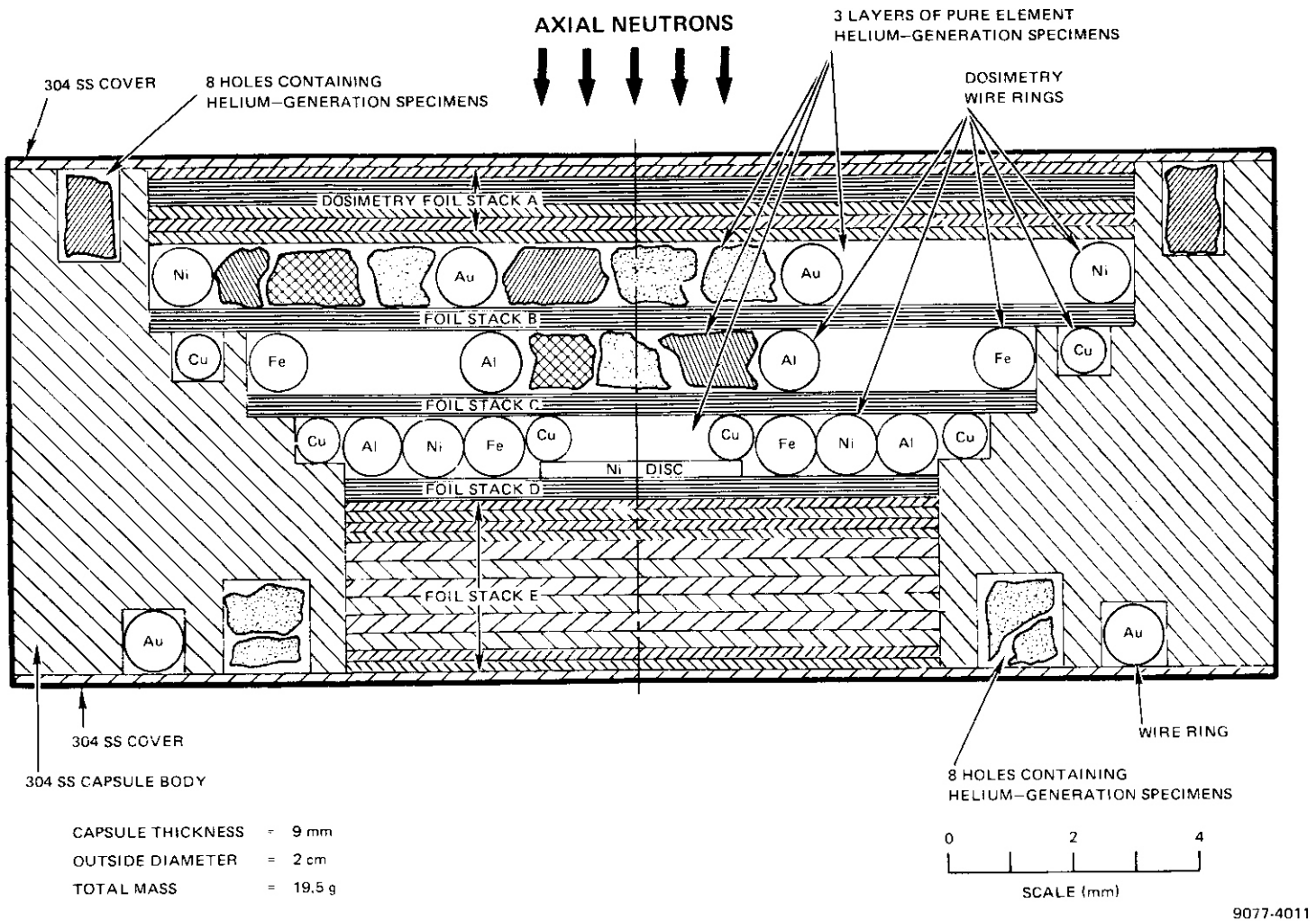

FIGURE 1. View of Be(d,n) Ir

TABLE 1

HELIUM CONCENTRATIONS IN Be(d,n) -
IRRADIATED PURE ELEMENT RING SEGMENTS

Ring	Sample	$\bar{\theta}$*	Mass (mg)	Atoms ^{4}He	appb+
Al	GAL-W1A	67°	0.5605	2.699 x 10^{11}	21.57
Layer 2	GAL-W1C	3°	0.7226	3.695 x 10^{11}	22.90
	GAL-W1E	302'	Q. 5617	3.502 x 10^{11}	27.93
	GAL-W1G	248'	0.4228	3.014 x 10^{11}	31.93
	GAL-W1I	191°	0.6299	4.559 x 10^{11}	32.42
	GAL-WlK	132'	0.6305	3.776 x 10^{11}	26.83
Fe	GFE-W2A	62°	2.195	1.691 x 10^{11}	7.14
Layer 3	GFE-W2B	43°	1.403	1.086 x 10^{11}	7.18
	GFE-W2C	29'	1.632	1.296 x 10^{11}	7.37
	GFE-W2E	351°	1.697	1.408 x 10^{11}	7.70
	GFE-W2G	311'	2.014	1.890 x 10^{11}	8.70
	GFE-W2I	273'	2.165	2.213 x 10^{11}	9.50
	GFE-W2K	228'	1.992	2.240 x 10^{11}	10.42
	GFE-W2M	185°	1.326	1.489 x 10^{11}	10.42
	GFE-W2O	154'	1.531	1.636 x 10^{11}	9.91
	GFE-W2Q	111°	2.445	2.302 x 10^{11}	8.75
Ni	GNI-W2A	74°	2.515	3.648 x 10^{11}	14.14
Layer 3	GNI-W2E	14°	2.473	3.634 x 10^{11}	14.32
	GNI-W2I	320°	2.054	3.468 x 10^{11}	16.46
	GNI-W2M	262'	2.932	6.032 x 10^{11}	20.05
	GNI-W2Q	206'	2.311	5.123 x 10^{11}	21.61
	GNI-W2U	154°	2.953	5.851 x 10^{11}	19.31

(See next page for footnotes)

Continued . . .

TABLE 1 (CON.)

HELIUM CONCENTRATIONS IN Be(d,n) - IRRADIATED PURE ELEMENT RING SEGMENTS

Ring	Sample	$\bar{\theta}$*	Mass (mg)	Atoms ^{4}He	appb^t
cu	GCU-W1E	22°	2.537	6.046 x 10^{10}	2.52
Layer 2	GCU-W1I	319°	2.579	7.456 x 10^{10}	3.05
	GCU-W1Q	192°	2.958	1.147 x 10^{11}	4.09
	GCU-W1U	132°	2.524	7.994 x 10^{10}	3.34
Inner Cu	GCU-W3A	56°	1.433	1.232 x 10^{11}	9.07
Layer 3	GCU-W3C	290°	1.575	1.595 x 10^{11}	10.69
	GCU-W3E	180°	1.653	1.769 x 10^{11}	11.30

*Average angular orientation of segment relative to capsule axis in plane of ring.

'Helium concentration in atomic parts per billion.

sensitivity gas mass spectrometer. The segments represent various locations around each ring. These initial results reflect ring irregularities relative to the capsule axis, with the effect magnified by the effect of energy-spectrum changes with source angle on the helium generation. Analyses of selected segments of all eleven helium dosimetry rings are continuing, and will provide a matrix of helium-generation dosimetry results covering the capsule volume.

IV. REFERENCES

1. D. W. Kneff and H. Farrar IV, Helium Generation in Fusion Reactor Materials, Technical Progress Report for Period April - September 1977, AI-DOE-13219, Atomics International, Canoga Park, CA, January 1978.

2. D. W. Kneff and H. Farrar IV, "Helium Generation in Fusion Reactor Materials," Contributions to the Damage Analysis and Fundamental Studies Periodic Technical Progress Report for the Period October 1977 to March 1978 (in press).

VII. FUTURE WORK

The helium analyses of selected pure element wire ring segments will continue. The results will be combined with the radiometric foil results to characterize the Be(d,n) neutron field, and the neutron fluence and energy profiles will be carefully mapped over the experimental volume. The other pure elements, alloys, and separated isotopes irradiated in this experiment will be analyzed for helium, and the results will be combined with the neutron mapping results to determine helium-generation cross sections for this Be(d,n) environment.

I. PROGRAM

Title: Irradiation Effects Analysis
Principal Investigator: D. G. Doran
Affiliation: Hanford Engineering Development Laboratory

II. OBJECTIVE

The objective of this work is to predict the spatial variations of radiation damage parameters within the test volume of the Fusion Materials Irradiation Test (FMIT) facility, and the sensitivity of these parameters to cross section and spectrum uncertainties.

III. RELEVANT DAFS PROGRAM TASK/SUBTASK

SUBTASK II.A.2.4 Flux Spectrum Definition in FMIT
SUBTASK II.B.I .5 Calculation of Displacement Cross Sections

IV. SUMMARY

The major finding so far is the insensitivity of spectral-averaged damage parameters to position throughout the test region where the flux is greater than $10^{14} n/cm^2-s$. This result is obtained for either uniform or Gaussian source distributions and for both unperturbed (source) spectra and for spectra perturbed by the presence of simulated test assemblies. That is, the variation in damage rates appears to be dominated by changes in flux, not spectrum. For the deuteron energies considered, 35, 30, and 15 MeV, the spectral-averaged helium-to-dpa ratios for copper and niobium vary by less than 11% in the test region. However, this ratio decreases by as much as 65 percent in going from 35 to 15 MeV deuterons.

A typical test assembly perturbation of neutron spectra from 35 MeV deuterons decreases the spectral-averaged damage energy cross section by 10 to 19 percent, and the spectral-averaged helium production cross section

by 15 to 28 percent. The corresponding decrease in the helium-to-dpa ratio is less than 10%. Effects of possible cross section uncertainties on spectral-averaged values are presented.

V. ACCOMPLISHMENTS AND STATUS

A. FMIT Damage Parameter Sensitivity Study - J. O. Schiffgens, R. L. Simons, F. M. Mann, and L. L. Carter

1. Introduction

FMIT is to be an accelerator-based high energy neutron irradiation facility utilizing d-Li breakup reactions. Although the neutron spectra will have the fusion energy neutrons lacking in fission reactor spectra, the FMIT spectra will extend to higher energies as well.[1] Characterization of the expected neutron field is essential for the development of appropriate experimental test assemblies and for the determination of required data accuracies. Since both needs must be reflected in the design of the facility, an FMIT damage parameter sensitivity study is in progress. This report summarizes the results thus far obtained.

The results of new neutron yield measurements for all deuteron energies and neutron emission angles of interest are not yet available.[2] Hence, source models fit to available data have been used to calculate spectra in the test region of the irradiation cell for use in this study. The neutron spectra used here were generated by F. M. Mann[1] and L. L. Carter.[3-5] Mann's model, as described previously,[6] provides unperturbed spectra throughout the irradiation cell. Carter's model, on the other hand, was devised to generate neutron flux maps within experimental test assemblies; it provides both perturbed and unperturbed spectra in the irradiation cell. The latter model employs a Monte Carlo procedure to determine the average spectrum on small surface segments within the empty or assembly-filled irradiation cell. An interpolation scheme permits the spectrum at any point within the cell to be obtained economically.

A reasonable basis for describing spectrum variations in neutron irradiation facilities is in terms of displacement per atom (dpa) and gas atoms generated from transmutation reactions (appm He or H). In this study, calculations were made of spectral-averaged damage energy and helium production cross sections for potential FMIT spectra. The emphasis here continues to be on the assessment of damage anticipated under likely operating conditions at locations of most interest for irradiation testing (i.e., where the total flux is greater than 10^{14} n/cm^2-s).

The first part of this report describes a comparison of results using uniform and Gaussian source distributions. This is followed by a discussion of the sensitivity of the results to cross section uncertainties. Finally, results of calculations with unperturbed spectra and spectra perturbed by a likely experimental test assembly are compared and discussed.

2. Results

a. Uniform and Gaussian Source Distributions

Although the source geometry in the flowing lithium target has been specified for the FMIT facility conceptual design to be a parallelepiped 10 cm wide, 1 cm high, and R cm deep, where the range R is 1.4 cm for 35 MeV deuterons, the optimum spatial distribution of deuterons striking the target is yet to be determined. That Mann and Carter have treated the source differently will be discussed later; for now consider only spectra from Mann's model and compare results from two extreme and idealized source distributions. Mann's model treats the deuterium ions as all being in a plane 10 cm wide and R cm deep*, incident normal to the flowing lithium surface. The two extreme cases are uniform and Gaussian distributions along the source width; in the latter, the deuterium ion density peaks at the center with an edge intensity about 1/100th that of the center and a full width at half maximum of about 5.5 cm.

*The energy loss of the ions is explicitly included.

Contour maps for unperturbed neutrons from a Gaussian source formed by a 0.1 amp beam of 35 MeV deuterons are shown in Figure 1. Note that, in comparison with a uniform source of identical deuteron intensity and energy,** the contours are more forward peaked and the volumes within equivalent contours are larger. The rate at which the test volume shrinks with increasing flux is further demonstrated in Figures 2, 3, and 4. These figures show plots of flux versus distance normal to the flowing lithium surface for various y-coordinates on an x-y plane for which the z-coordinate is 0.1, 0.5, and 0.9 cm, respectively. The flux in the x-direction changes fastest near the x-y mid-plane where the flux is highest; for small values of x, the flux along the x-direction and that along the y-direction change much faster than they do for a uniform source.

Neutron spectra for deuteron energies of 35, 30, and 15 MeV have been calculated at the twelve positions shown in Figure 5 for both uniform and Gaussian source distributions. With these data, spectral-averaged damage energy cross sections and helium production cross sections for copper and niobium have been calculated using the damage energy cross sections of Roberto and Robinson[7] and the (n,α) and (n, ax) cross sections of Fu and Perey.[8] The mean neutron energies and corresponding averaged cross sections for each of the twelve positions shown in Figure 5 are presented in Tables 1 through 6. Included in these tables is the spectral-averaged helium-to-dpa ratio.* The most striking feature of these data is their overall insensitivity to position within the test region (as defined in Figure 5), even though the flux changes by as much as two orders of magnitude. At each deuteron energy considered, the spectral-averaged helium-to-dpa ratios for copper and niobium vary by less than 7% and 11%, respectively. This ratio decreases by about 50% for copper and 60% for niobium in going from 35 to 15 MeV deuterons.

---

* Damage energy cross sections were converted to displacement cross sections by multiplying by $0.8/2\ E_d$. Values used for E_d were 30 eV for copper and 60 eV for niobium.

b. Cross Section Uncertainties

In order to estimate the effect of cross section uncertainties on spectral-averaged values, cross sections were artificially perturbed above E_0 by a factor $(E/E_0)^b$, where E_0 is the neutron energy below which the cross section is assumed to be fairly well known, and b is an arbitrary constant. For this study, E_0 is taken to be 14 MeV and b is set equal to ± 0.3, so that for a maximum neutron energy of 50 MeV the cross section uncertainty is about ± 50 percent, as shown in Figures 6 through 9. For each of the deuteron energies considered, the corresponding percentage changes in the spectral-and volume-averaged cross sections are presented in Table 7. It should be noted that the spatial variation in the percentage change was always less than a few tenths of a percent. The calculated uncertainties in spectral-averaged values are, of course, largest at the highest deuteron energy. In general, the uncertainties in the averaged damage energy cross section are about the same for copper and niobium, while the uncertainties in the averaged helium production cross section are somewhat larger for niobium than for copper because of the higher threshold energy of the former.

c. Unperturbed and Test Assembly Perturbed Spectra

Figure 10 shows the module configurations of a typical irradiation test assembly.[9] Module A occupies the prime test region and is expected to be densely packed with test specimens. Module B is expected to contain a less dense packing of test specimens and support equipment. Module C would contain support equipment and have limited structural members. Spectra were calculated by Carter with and without this test assembly in the irradiation cell. Both unperturbed and test assembly perturbed spectra at positions 1 and 10 are plotted in Figure 11. At these positions, and position 2 as well, the total flux is higher in the perturbed spectrum than in the unperturbed spectrum due to neutron back-scattering from the rest of the test assembly. This back-scattering lowers the high energy flux and raises the low energy flux, with the result that the spectral-

averaged damage energy and helium production cross sections are lower in the perturbed spectra by 10 to 19 percent and 15 to 28 percent, respectively, as shown in Tables 8 and 9. The helium/dpa ratio drops by less than 10%.

Note that the fluxes and averaged cross sections for the unperturbed spectra in Tables 8 and 9 are different from those presented in Tables 1 and 4. This is due to the fact that the treatment of the source in Carter's Monte Carlo calculations was somewhat different from that used by Mann. Spectra from Mann and Carter at positions 1 and 10 (see Figure 5) are displayed in Figure 12. While the spectra at position 10 agree rather well below 25 MeV, there are substantial differences between the spectra at position 1 over the entire range. Mann modeled the source in terms of neutron stripping and compound nucleus formation, and normalized the resulting cross sections to the thick target yield data of Saltmarsh et. al.[10] at E_d = 40 MeV and θ = 0° and 90° (see Figure 13). In order to reflect the presence of experimentally observed shoulders in yield curves,[2] Carter altered and renormalized the source data of Mann for his model. A better treatment of the neutron yield incorporating recently obtained experimental data is being developed and will be employed in future calculations.

In addition to differences in yield curves, there are differences in the spatial distribution of neutrons in the source as treated in each model. In Mann's model, the neutron source is two dimensional, with neutrons of appropriate energy originating along the depth of the source plane reflecting deuteron slowdown in the flowing lithium. Carter, on the other hand, treats the source as three dimensional with neutrons of all energies originating at points uniformly distributed throughout the source volume. Consequently, Mann's source overestimates the flux near the origin, as shown in Figure 12 and Tables 1-6. Note, also, that Carter's spectra are a good bit softer than Mann's. This is due to the fact that Carter has used a relatively much larger spatial mesh to determine the neutron energy dependence than that used to determine the neutron flux spatial dependence near the source. For future calculations, Mann's source is

being extended to three dimensions and Carter's mesh for calculating the neutron energy dependence will be made finer.

VI. REFERENCES

1. J. O. Schiffgens, R. L. Simons, and F. M. Mann, DAFS Quarterly Technical Progress Report, October 1977-March 1978, p. 43 (in press).

2. Preliminary results of neutron yield measurements from 35 MeV deuterons on a thick lithium target made by D. L. Johnson, HEDL, show a high energy shoulder at neutron energies above about 35 MeV.

3. E. D. Cashwell, J. R. Neergaard, W. M. Taylor, and G. D. Turner, MCN: A Neutron Monte Carlo Code, LA-4751, Los Alamos Scientific Laboratory, Los Alamos, NM, January 1972.

4. E. D. Cashwell, J. R. Neergaard, C. J. Everett, R. G. Schrandt, W. M. Taylor, and G. D. Turner, Monte Carlo Photon Codes MCG and MCP, LA-5157-MS, Los Alamos Scientific Laboratory, Los Alamos, NM, March 1973.

5. L. L. Carter and E. D. Cashwell, "Particle Transport Simulation with the Monte Carlo Method," ERDA Critical Review Series, TID-26607 U. S. Energy Research and Development Administration, Technical Information Center, Oak Ridge, TN (1975).

6. F. M. Mann, "Neutron Environment in d-Li Facilities," HEDL-SA-1464, 1978.

7. J. B. Roberto and M. T. Robinson, J. Nucl. Mat. 61, p. 149, (1976)

8. C. Y. Fu and F. G. Perey, J. Nucl. Mat. 61, p. 153, (1976).

9. A likely irradiation test assembly configuration and density distribution was provided by R. E. Nygren, HEDL.

10. M. J. Saltmarsh, C. A. Ludeman, C. B. Fuller, and R. C. Styles, "Neutron Yields and Dosimetry for Be(d,n) and Li(d,n) Neutron Sources at E_d = 40 MeV," NBSIR 77-1279, 24, National Bureau of Standards (1977). ORNL TM-5696, Oak Ridge National Laboratory.

VII. FUTURE WORK

Calculations to define the effect of data uncertainties for FMIT will be continued, including analyses of spectral-averaged damage parameters for stainless steel.

VIII. PUBLICATIONS

None.

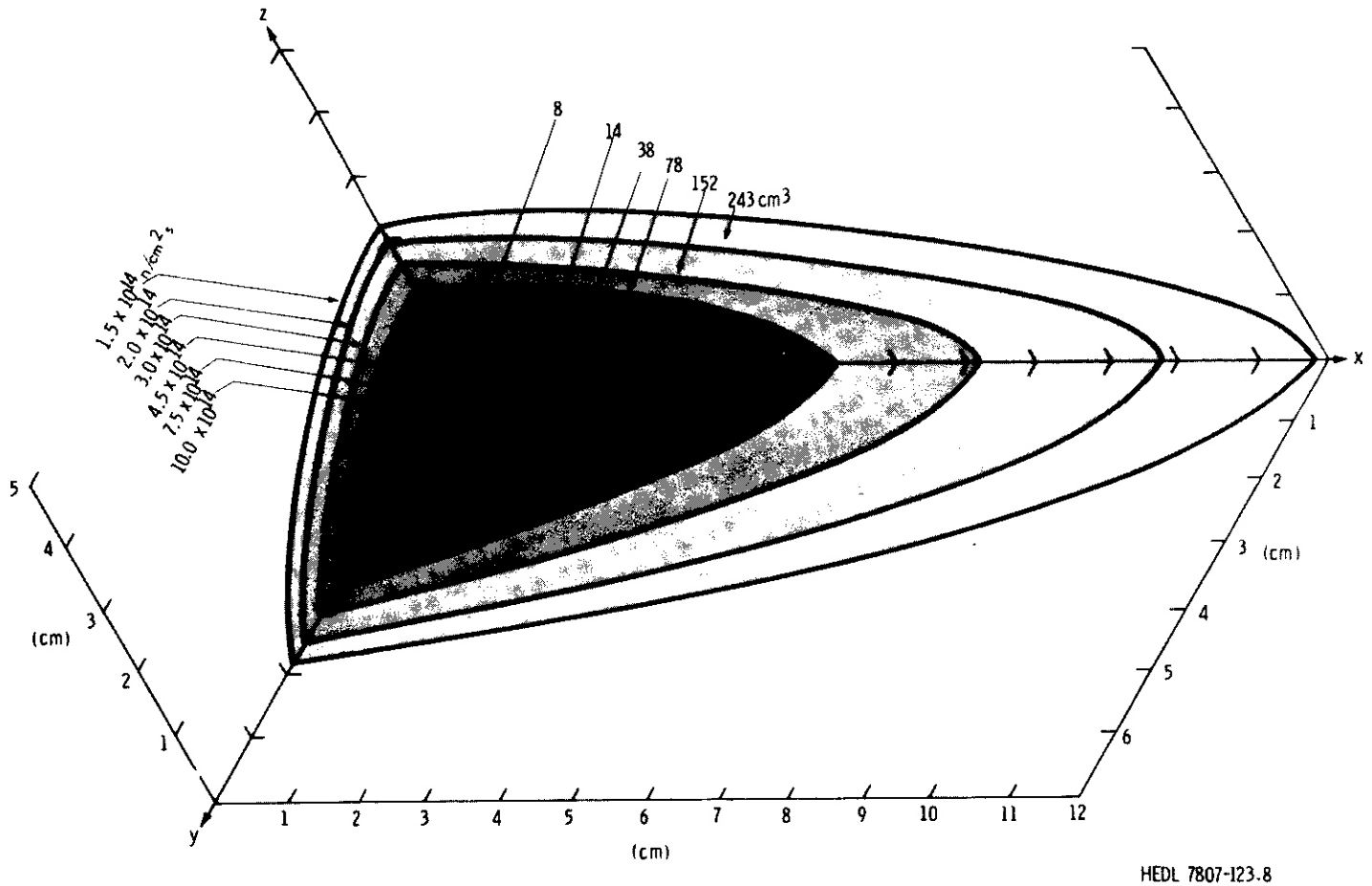

Figure 1. Flux Contour Maps for a Gaussian Source Distribution. The Deuteron Energy is 35 MeV and the Beam Current is 0.1 amp. The Irradiation Volumes Within the Given Contours are listed.

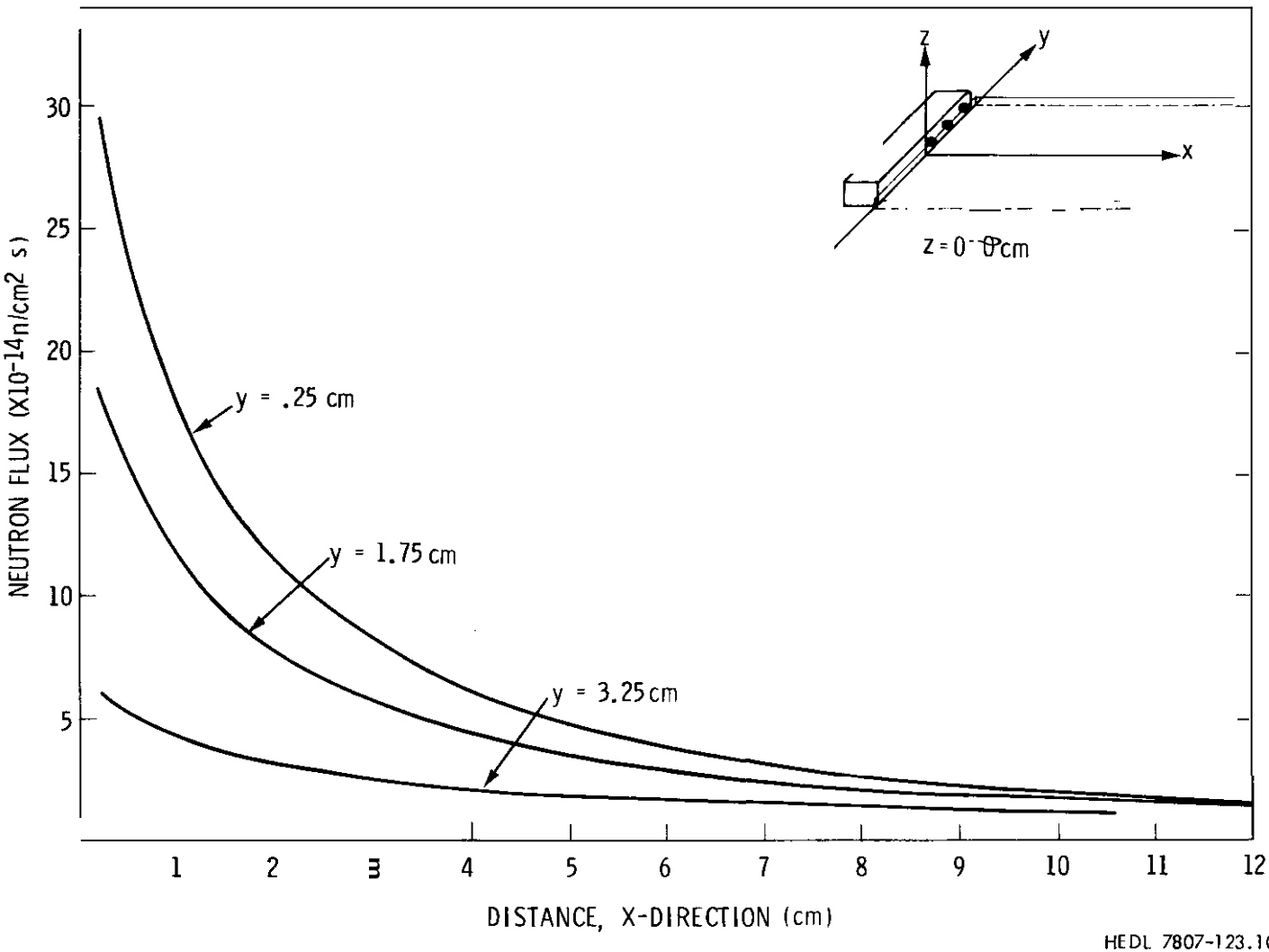

Figure 2 Flux Versus Distance Normal to the Source Surface for Some Y-Coordinates on the Plane Z = 0.1 cm.

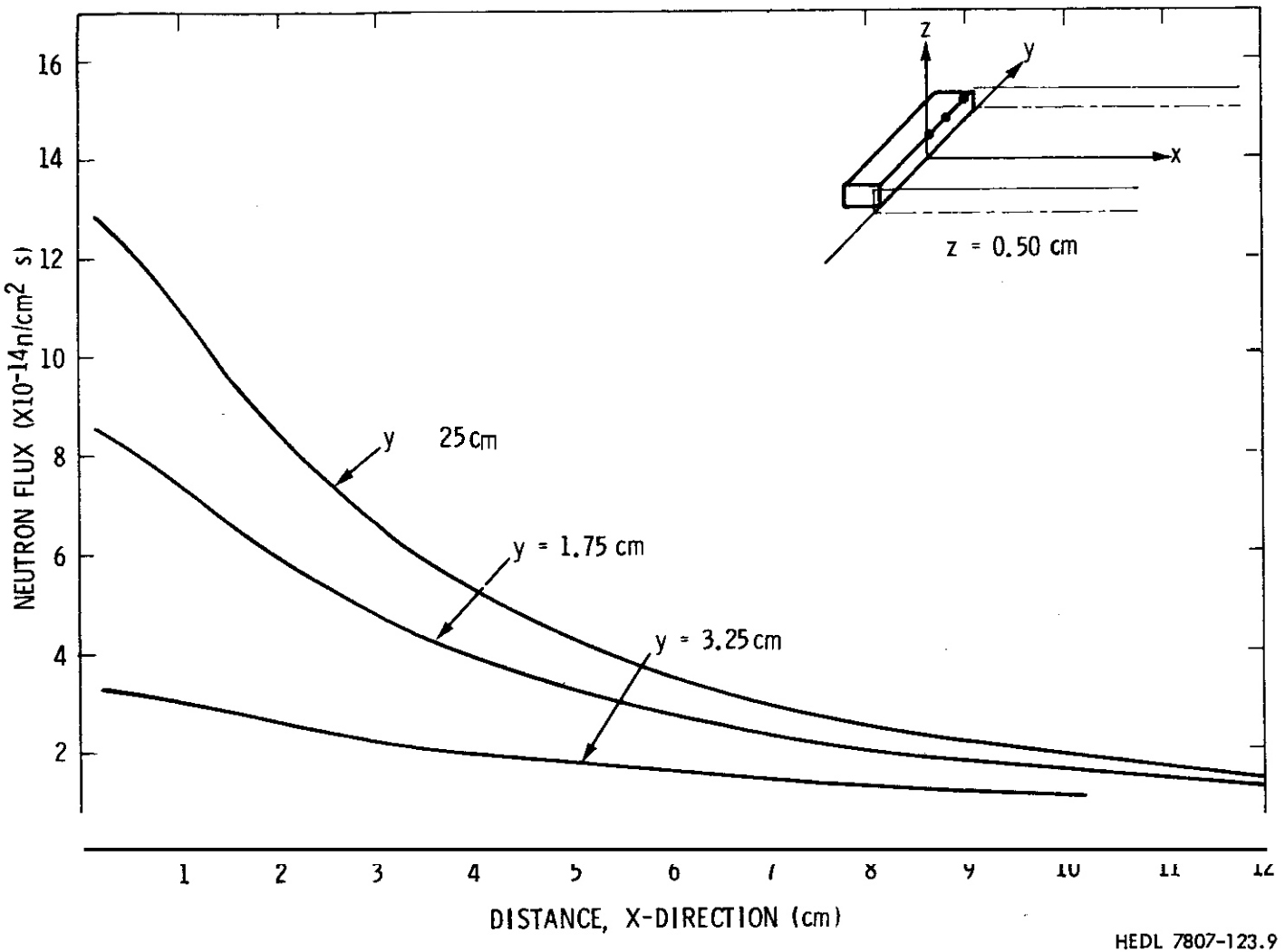

Figure 3 Flux Versus Distance Normal to the Source Surface for S e Y-Coordinates on an X-Y Plane with a Z-Coordinate of 0.5 cm.

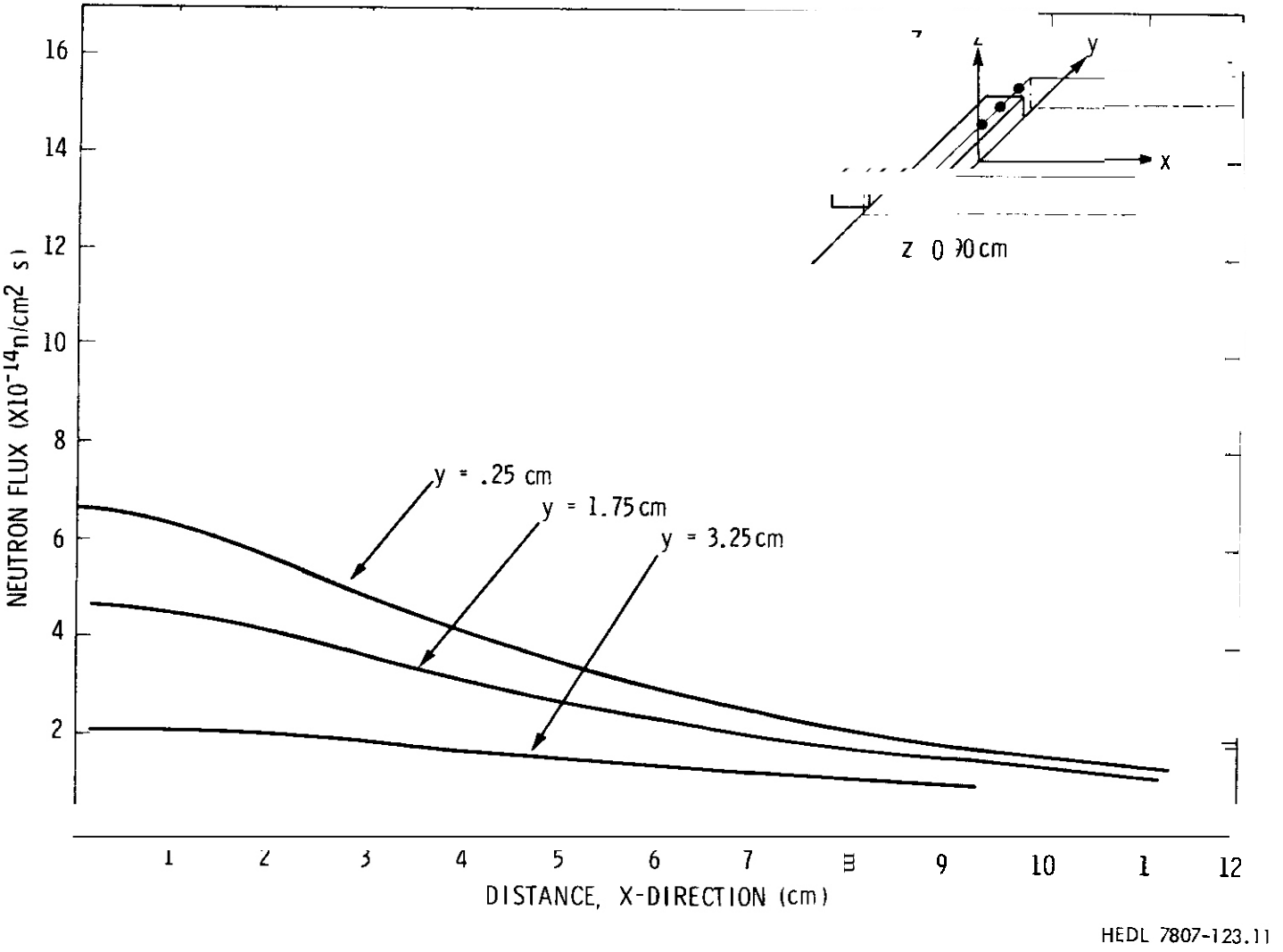

Figure 4. Flux Versus Distance Normal to the Source Surface for Some Y-Coordinates on an X-Y Plane With a Z-Coordinate of 0.9 cm.

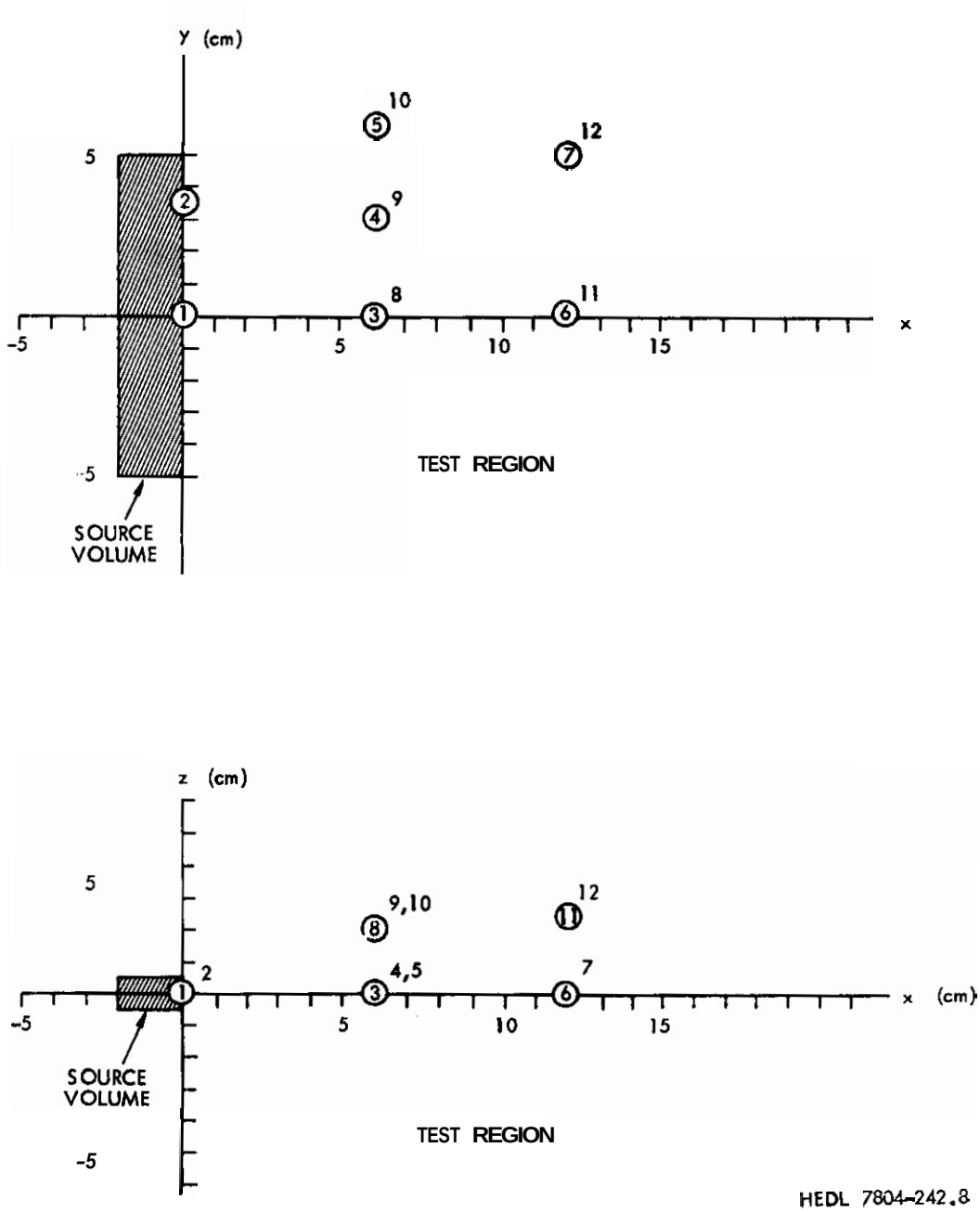

Figure 5. Positions Within the Test Cell at Which Neutron Spectra Were Calculated.

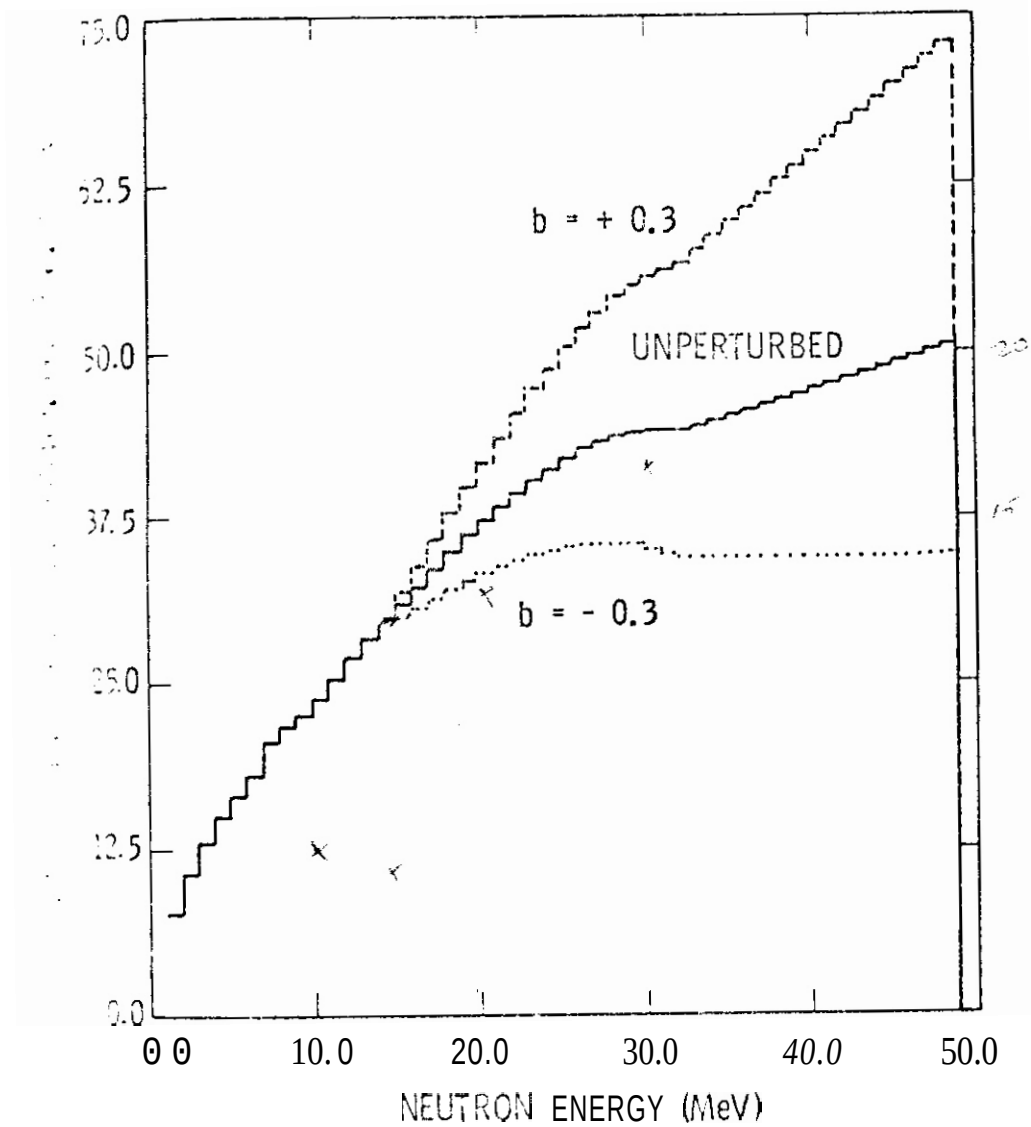

Figure 6. Perturbed and Unperturbed Damage Energy Cross Sections for Copper versus Neutron Energy.

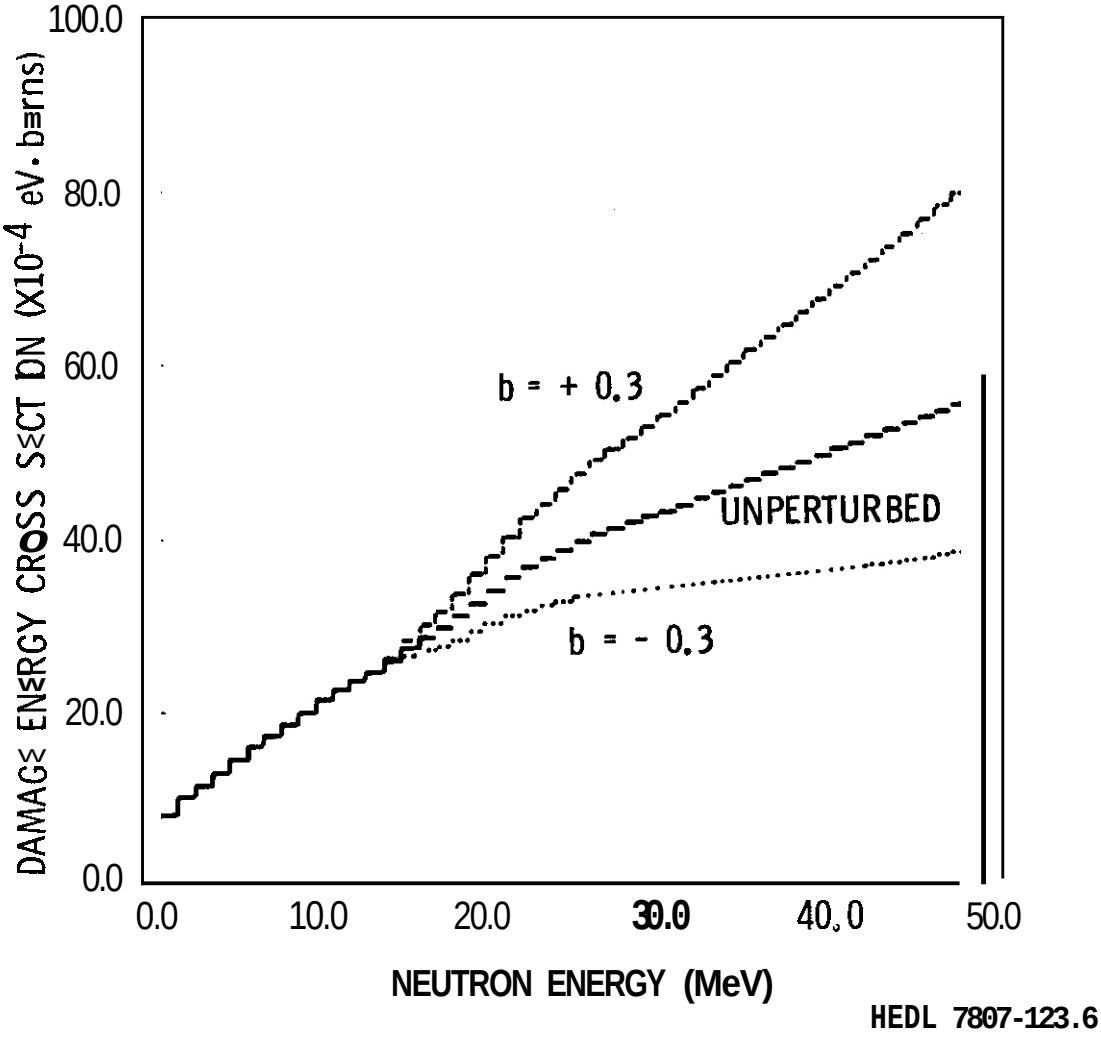

Figure 7. Perturbed and Unperturbed Damage Energy Cross Sections for Niobium versus Neutron Energy.

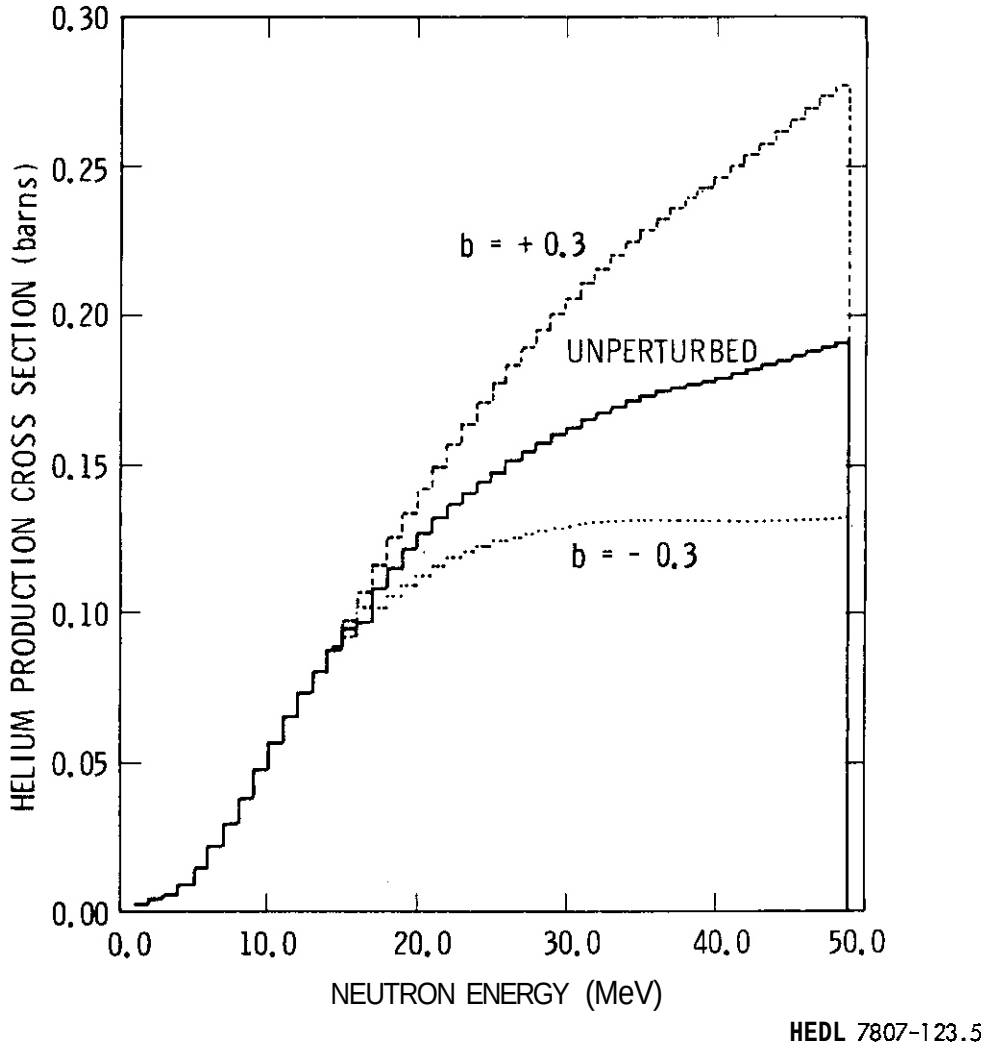

Figure 8. Perturbed and Unperturbed Helium Production Cross Sections for Copper versus Neutron Energy.

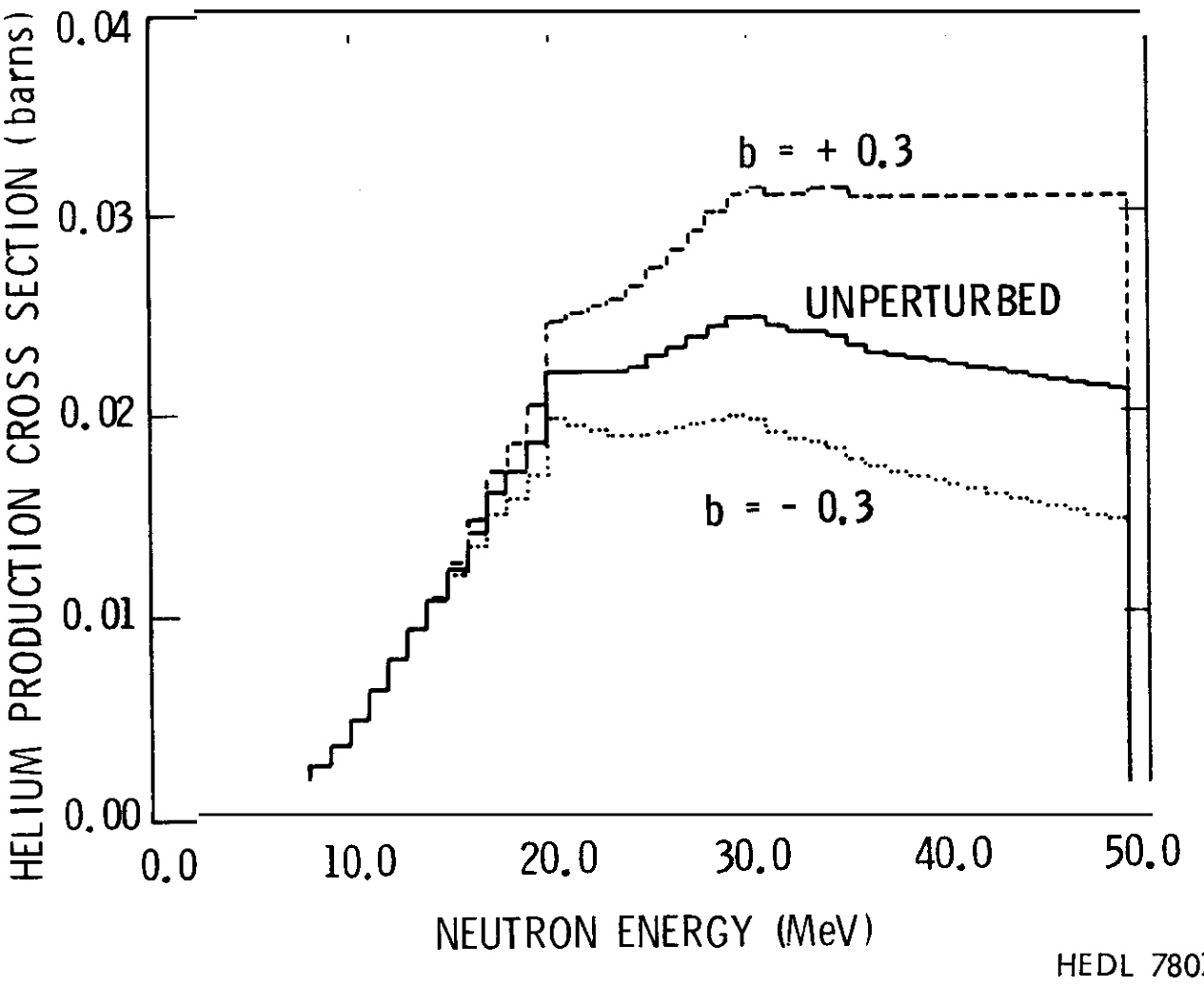

Figure 9 Perturbed and Unperturbed Helium Production Cross Sections for Niobium versus Neutron Energy.

ALL DIMENSIONS ARE IN CENTIMETERS

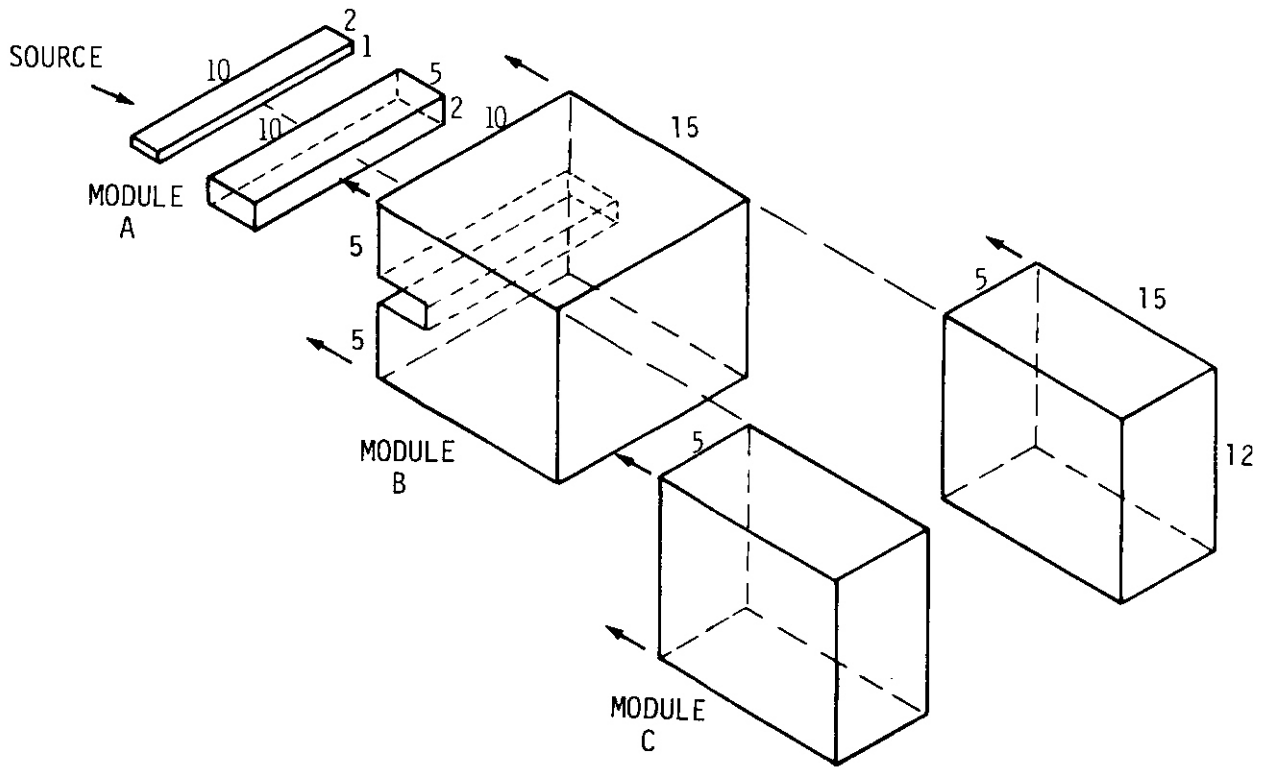

TEST ASSEMBLY MODULES	A	B	C
PERCENT STAINLESS STEEL DENSITY	50	25	10

Figure 10. Module Configurations of a Typical Irradiation Test Assembly

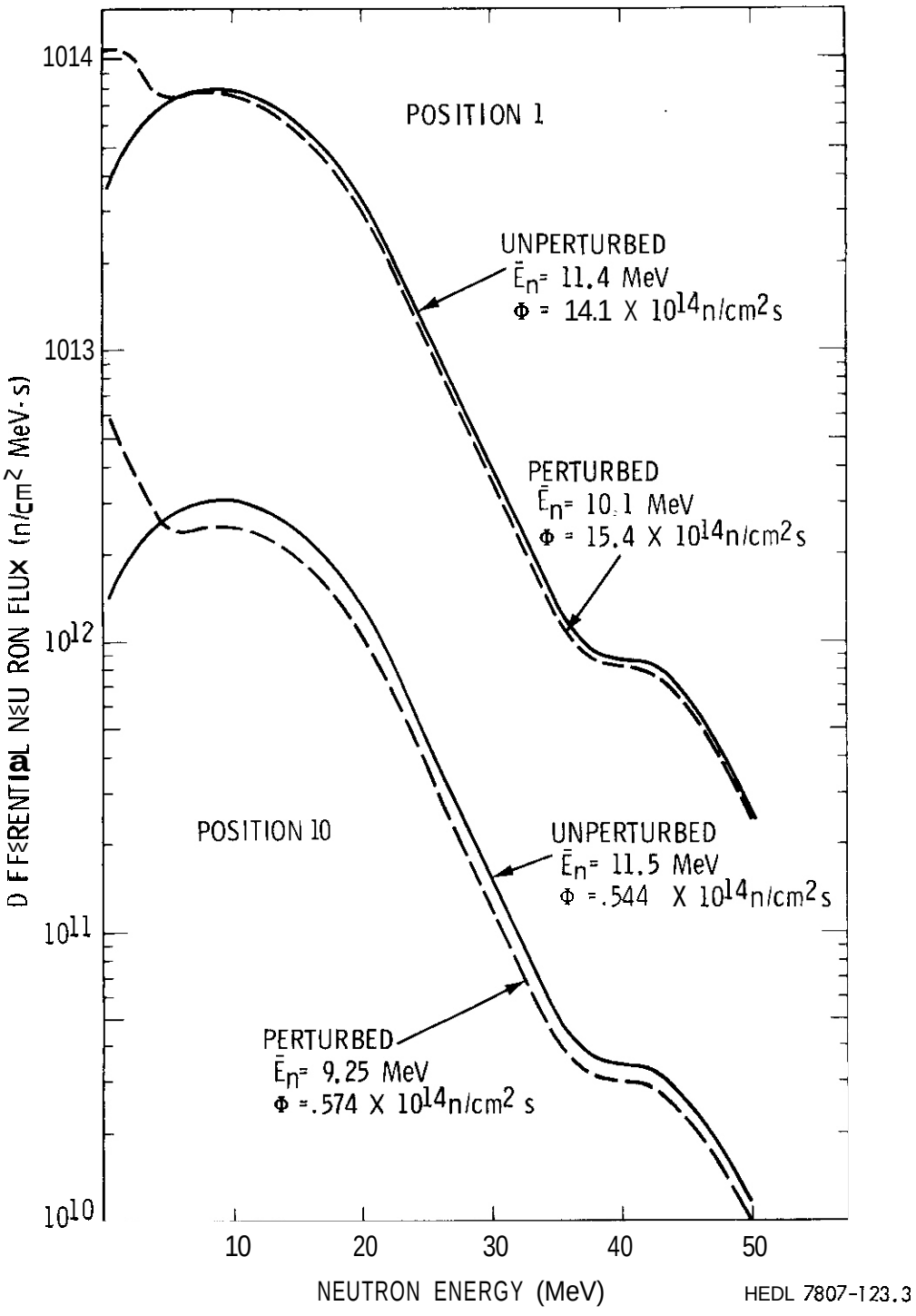

Figure 11. Calculated Perturbed and Unperturbed Neutron Spectra at Positions 1 and 10 in the Test Region, as Shown in Figure 5. The Deuteron Energy is 35 MeV, the Beam Current is 0.1 amp.

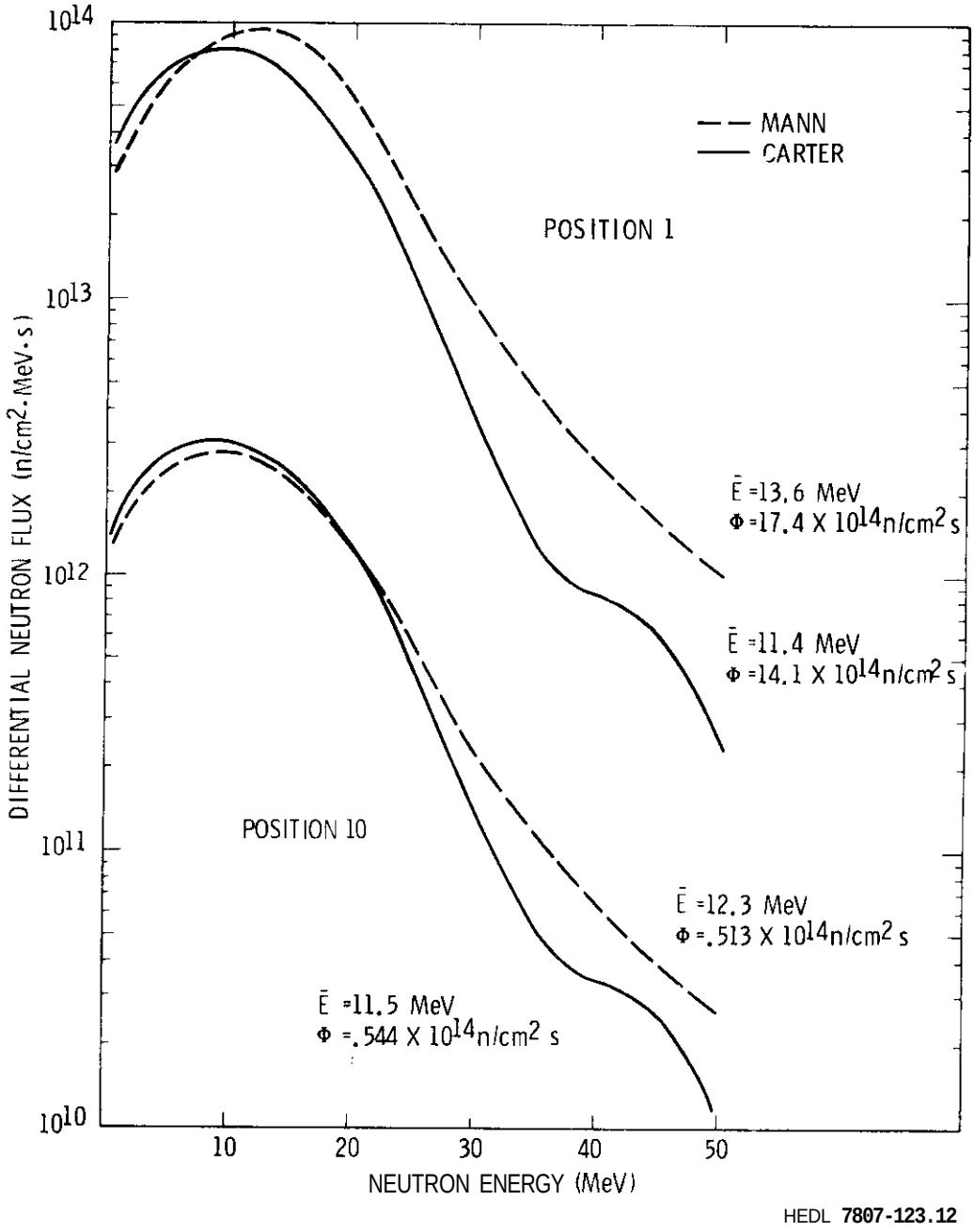

Figure 12. Calculated Neutron Spectra at Positions 1 and 10 in the Test Region as Shown in Figure 5. The Deuteron Energy is 35 MeV and the Beam Current is 0.1 amp.

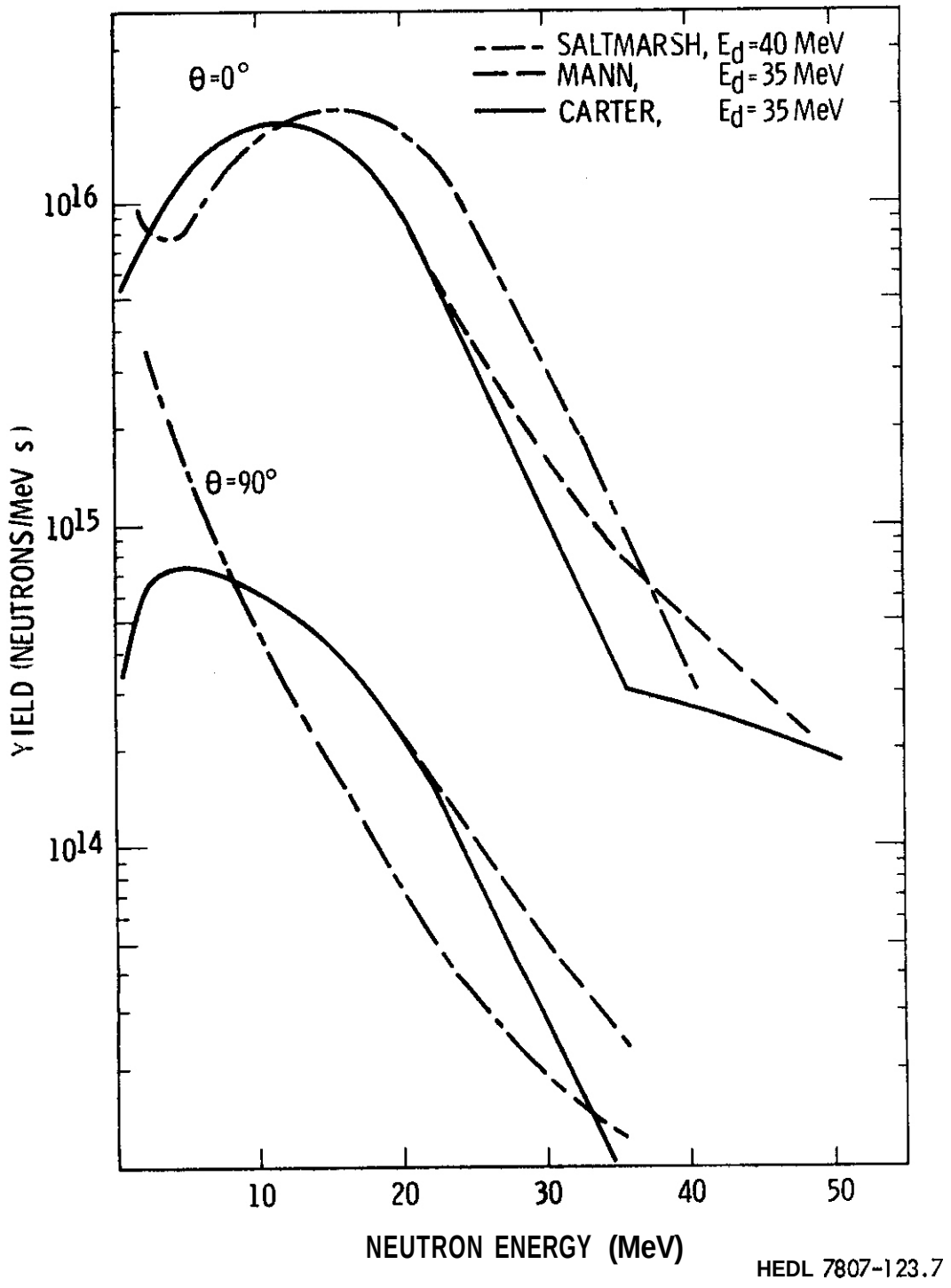

Figure 13. Neutron Yields From Li(d,n) Reactions for a Deuteron Beam Current of 0.1 amp.

TABLE 1

SPECTRAL-AVERAGED CROSS SECTIONS AND HELIUM PRODUCTION TO DISPLACEMENT RATIOS FOR COPPER WITHIN THE TEST VOLUME; E_d = 35 MeV

Position				Uniform Source					Gaussian Source				
#	X (cm)	Y (cm)	Z (cm)	ϕ (10^{+14} n/cm^{2}s)	$\bar{E}_n$ (MeV)	$\bar{\sigma}_{dam}$ (10^{+4} eV·b)	$\bar{\sigma}_{He}$ (b)	appm He / dpa	ϕ (10^{+14} n/cm^{2}s)	$\bar{E}_n$ (MeV)	$\bar{\sigma}_{dam}$ (10^{+4} eV·b)	$\bar{\sigma}_{He}$ (b)	appm He / dpa
1	0	0	0	17.4	13.6	27.0	.0744	20.7	37.9	13.8	27.2	.0753	20.8
2	0	3.5	0	17.7	13.7	27.2	.0752	20.7	5.53	13.2	26.5	.0719	20.3
3	6	0	0	2.34	13.2	26.5	.0716	20.3	3.69	13.4	26.8	.0733	20.5
4	6	3	0	2.12	13.2	26.5	.0720	20.4	1.74	13.0	26.2	.0704	20.2
5	6	6	0	0.754	12.6	25.7	.0678	19.8	0.426	12.1	25.0	.0646	19.4
6	12	0	0	1.07	13.3	26.6	.0722	20.4	1.40	13.5	26.9	.0737	20.5
7	12	5	0	0.648	13.1	26.3	.0710	20.2	0.478	12.7	25.8	.0685	19.9
8	6	0	2	1.19	12.5	25.6	.0673	19.7	1.61	12.7	25.8	.0683	19.9
9	6	3	2	1.04	12.6	25.6	.0674	19.7	0.980	12.5	25.5	.0668	19.6
10	6	6	2	0.513	12.3	25.2	.0655	19.5	0.354	12.0	24.8	.0638	19.3
11	12	0	2.5	0.678	12.9	26.0	.0694	20.0	0.814	13.0	26.2	.0702	20.0
12	12	5	2.5	0.442	12.7	25.8	.0683	19.9	0.373	12.5	25.6	.0672	19.7

TABLE 2

SPECTRAL-AVERAGED CROSS SECTIONS AND HELIUM PRODUCTION TO DISPLACEMENT RATIOS FOR COPPER WITHIN THE TEST VOLUME; E_d = 30 MeV

Position				Uniform Source					Gaussian Source				
#	X (cm)	Y (cm)	Z (cm)	ϕ (10^{+14} n/cm^{2}s)	$\bar{E}_n$ (MeV)	$\bar{\sigma}_{dam}$ (10^{+4} eV·b)	$\bar{\sigma}_{He}$ (b)	appm He / dpa	ϕ (10^{+14} n/cm^{2}s)	$\bar{E}_n$ (MeV)	$\bar{\sigma}_{dam}$ (10^{+4} eV·b)	$\bar{\sigma}_{He}$ (b)	appm He / dpa
1	0	0	0	9.97	11.6	24.6	.0620	18.9	21.4	11.9	24.8	.0636	19.1
2	0	3.5	0	9.87	11.7	24.7	.0625	19.0	3.47	11.4	24.2	.0600	18.6
3	6	0	0	1.63	11.5	24.4	.0609	18.7	2.52	11.8	24.7	.0626	19.0
4	6	3	0	1.46	11.5	24.4	.0612	18.8	1.25	11.4	24.2	.0604	18.7
5	6	6	0	0.562	11.0	23.7	.0579	18.3	0.337	10.7	23.2	.0555	17.9
6	12	0	0	0.745	11.6	24.5	.0616	18.9	0.967	11.9	24.8	.0630	19.1
7	12	5	0	0.642	11.4	24.3	.0605	18.7	0.361	11.2	23.9	.0589	18.5
8	6	0	2	0.900	11.0	23.7	.0576	18.2	1.21	11.2	23.9	.0586	18.4
9	6	3	2	0.784	11.0	23.7	.0576	18.2	0.752	11.0	23.6	.0574	18.2
10	6	6	2	0.397	10.8	23.3	.0561	18.1	0.283	10.6	23.0	.0549	17.9
11	12	0	2.5	0.500	11.3	24.0	.0594	18.6	0.598	11.5	24.3	.0603	18.6
12	12	5	2.5	0.330	11.1	23.9	.0584	18.3	0.287	11.1	23.2	.0578	18.3

TABLE 3

SPECTRAL-AVERAGED CROSS SECTIONS AND HELIUM PRODUCTION TO DISPLACEMENT RATIOS FOR COPPER WITHIN THE TEST VOLUME; E_d = 15 MeV

Position				Uniform Source					Gaussian Source				
#	X (cm)	Y (cm)	Z (cm)	ϕ (10^{+14} n/cm^{2}s)	$\bar{E}_n$ (MeV)	$\bar{\sigma}_{dam}$ (10^{+4} eV·b)	$\bar{\sigma}_{He}$ (b)	appm He / dpa	ϕ (10^{+14} n/cm^{2}s)	$\bar{E}_n$ (MeV)	$\bar{\sigma}_{dam}$ (10^{+4} eV·b)	$\bar{\sigma}_{He}$ (b)	appm He / dpa
1	0	0	0	1.71	6.39	17.1	.0266	11.7	3.40	6.45	17.2	.0269	11.7
2	0	3.5	0	1.59	6.42	17.1	.0268	11.8	0.755	6.26	16.8	.0259	11.6
3	6	0	0	0.345	6.45	17.2	.0269	11.7	0.485	6.53	17.3	.0274	11.9
4	6	3	0	0.302	6.45	17.2	.0270	11.8	0.292	6.40	17.1	.0266	11.7
5	6	6	0	0.143	6.29	16.9	.0260	11.5	0.107	6.15	16.6	.0252	11.4
6	12	0	0	0.153	6.51	17.3	.0273	11.8	0.185	6.57	17.4	.0276	11.9
7	12	5	0	0.104	6.43	17.2	.0268	11.7	0.0943	6.35	17.0	.0264	11.6
8	6	0	2	0.242	6.31	16.9	.0261	11.6	0.316	6.37	17.1	.0265	11.6
9	6	3	2	0.211	6.31	16.9	.0261	11.6	0.213	6.28	16.9	.0260	11.5
10	6	6	2	0.177	6.20	16.7	.0255	11.5	0.930	6.12	16.6	.0250	11.3
11	12	0	2.5	0.120	6.41	17.1	.0267	11.7	0.140	6.45	17.2	.0270	11.8
12	12	5	2.5	0.088	6.34	17.0	.0263	11.6	0.0805	6.30	16.9	.0261	11.6

TABLE 4

SPECTRAL-AVERAGED CROSS SECTIONS AND HELIUM PRODUCTION TO DISPLACEMENT RATIOS FOR NIOBIUM WITHIN THE TEST VOLUME; E_d = 35 MeV

Position				Uniform Source					Gaussian Source				
#	X (cm)	Y (cm)	Z (cm)	ϕ (10^{+14} n/cm^{2}s)	$\bar{E}_n$ (MeV)	$\bar{\sigma}_{dam}$ (10^{+4} eV·b)	$\bar{\sigma}_{He}$ (b)	appm He / dpa	ϕ (10^{+14} n/cm^{2}s)	$\bar{E}_n$ (MeV)	$\bar{\sigma}_{dam}$ (10^{+4} eV·b)	$\bar{\sigma}_{He}$ (b)	appm He / dpa
1	0	0	0	17.4	13.6	24.4	.00954	5.87	37.9	13.8	24.6	.00968	5.90
2	0	3.5	0	17.7	13.7	24.5	.00967	5.92	5.53	13.2	23.9	.00915	5.74
3	6	0	0	2.34	13.2	23.9	.00909	5.71	3.69	13.4	24.2	.00933	5.80
4	6	3	0	2.12	13.2	23.9	.00915	5.74	1.74	13.0	23.6	.00890	5.66
5	6	6	0	0.754	12.6	23.1	.00849	5.51	0.426	12.1	22.5	.00800	5.33
6	12	0	0	1.07	13.3	24.0	.00918	5.74	1.40	13.5	24.2	.00942	5.84
7	12	5	0	0.648	13.1	23.7	.00899	5.69	0.478	12.7	23.3	.00860	5.54
8	6	0	2	1.19	12.5	23.0	.00841	5.49	1.61	12.7	23.2	.00856	5.53
9	6	3	2	1.04	12.6	23.0	.00842	5.49	0.980	12.5	22.9	.00833	5.46
10	6	6	2	0.513	12.3	22.7	.00814	5.38	0.354	12.0	22.3	.00788	5.30
11	12	0	2.5	0.678	12.9	23.4	.00873	5.60	0.814	13.0	23.6	.00887	5.64
12	12	5	2.5	0.442	12.7	23.2	.00857	5.54	0.373	12.5	23.0	.00839	5.47

TABLE 5

SPECTRAL-AVERAGED CROSS SECTIONS AND HELIUM PRODUCTION TO DISPLACEMENT RATIOS FOR NIOBIUM WITHIN THE TEST VOLUME; E_d = 30 MeV

Position				Uniform Source					Gaussian Source				
#	X (cm)	Y (cm)	Z (cm)	ϕ (10^{+14} n/cm^{2}s)	$\bar{E}_n$ (MeV)	$\bar{\sigma}_{dam}$ (10^{+4} eV·b)	$\bar{\sigma}_{He}$ (b)	appm He / dpa	ϕ (10^{+14} n/cm^{2}s)	$\bar{E}_n$ (MeV)	$\bar{\sigma}_{dam}$ (10^{+4} eV·b)	$\bar{\sigma}_{He}$ (b)	appm He / dpa
1	0	0	0	9.97	11.0	22.0	.00744	5.07	21.4	11.9	22.6	.00738	5.12
2	0	3.5	0	9.87	11.3	22.1	.00752	5.10	3.47	11.4	21.6	.00703	4.95
3	6	0	0	1.63	11.5	21.8	.00727	5.00	2.52	11.8	22.1	.00751	5.10
4	6	3	0	1.46	11.5	21.9	.00732	5.01	1.25	11.4	21.7	.00716	4.95
5	6	6	0	0.562	11.0	21.2	.00683	4.83	0.337	10.7	20.8	.00648	4.67
6	12	0	0	0.745	11.6	21.9	.00737	5.05	0.967	11.9	22.2	.00758	5.12
7	12	5	0	0.642	11.4	21.7	.00721	4.98	0.361	11.2	21.4	.00696	4.88
8	6	0	2	0.900	11.0	21.2	.00678	4.80	1.21	11.2	21.4	.00692	4.85
9	6	3	2	0.784	11.0	21.2	.00678	4.80	0.752	11.0	21.1	.00674	4.79
10	6	6	2	0.397	10.8	20.9	.00657	4.72	0.283	10.6	20.6	.00639	4.65
11	12	0	2.5	0.500	11.3	21.5	.00704	4.91	0.598	11.5	21.7	.00717	4.96
12	12	3	2.5	0.330	11.1	21.3	.00691	4.87	0.287	11.1	21.2	.00679	4.80

TABLE 6

SPECTRAL-AVERAGED CROSS SECTIONS AND HELIUM PRODUCTION TO DISPLACEMENT RATIOS FOR NIOBIUM WITHIN THE TEST VOLUME; E_d = 15 MeV

Position				Uniform Source					Gaussian Source				
#	X (cm)	Y (cm)	Z (cm)	ϕ (10^{+14} n/cm^{2}s)	$\bar{E}_n$ (MeV)	$\bar{\sigma}_{dam}$ (10^{+4} eV·b)	$\bar{\sigma}_{He}$ (b)	appm He / dpa	ϕ (10^{+14} n/cm^{2}s)	$\bar{E}_n$ (MeV)	$\bar{\sigma}_{dam}$ (10^{+4} eV·b)	$\bar{\sigma}_{He}$ (b)	appm He / dpa
1	0	0	0	1.71	6.39	15.2	.00224	2.21	1.40	6.45	15.3	.00227	
2	0	3.5	0	1.59	6.42	15.2	.00225	2.22	0.755	6.26	15.0	.00217	
3	6	0	0	0.345	6.45	15.3	.00227	2.23	0.485	6.53	15.4	.00232	
4	6	3	0	0.302	6.45	15.3	.00227	2.23	0.292	6.40	15.2	.00224	
5	6	6	0	0.148	6.29	15.0	.00218	2.18	0.107	6.15	14.8	.00210	
6	12	0	0	0.153	6.51	15.4	.00230	2.24	0.185	6.57	15.4	.00234	
7	12	6	0	0.104	6.43	15.2	.00226	2.23	0.0943	6.35	15.1	.00211	
8	6	0	2	0.242	6.31	15.1	.00219	2.18	0.316	6.37	15.2	.00222	
9	6	3	2	0.211	6.31	15.1	.00219	2.18	0.213	6.28	15.0	.00217	
10	6	6	2	0.127	6.20	14.9	.00213	2.19	0.0930	6.12	14.8	.00208	
11	12	0	2.5	0.120	6.41	15.2	.00225	2.22	0.140	6.45	15.3	.00227	
12	12	5	2.5	0.085	6.34	15.1	.00220	2.19	0.805	6.30	15.0	.00218	

TABLE 7

AVERAGE<PERCENTAGE CHANGE>*IN SPECTRAL-AVERAGED CROSS SECTIONS DUE TO ASSUMED CROSS SECTION VARIATIONS ABOVE 14 MeV

$$\sigma>_p = \left\{ \int_o^{E_o} \sigma(E)\phi(E)dE + \int_{E_o}^{E_{max}} \sigma(E)(E/E \quad b \ \phi(E)dE \right\} \Big/ \int_o^{E_{max}} \phi(E)dE$$

$$<\sigma> = \int_o^{E_{max}} \sigma(E)\phi(E)dE \Big/ \int_o^{E_{max}} \phi(E)dE$$

$$<PC> = \left\langle \frac{<\sigma>_p - <\sigma>}{<\sigma>} \right\rangle \times 100\%$$

Cross Section	b	PC E_d = 15 MeV	E_d = 30 MeV	E_d = 35 MeV
σ_{dam}(Cu)	+.3	+1.2	+5.0	+6.7
	-.3	-1.0	-4.2	-5.8
σ_{He}(Cu)	+.3	+2.6	+7.1	+9.0
	-.3	-2.3	-5.9	-7.5
σ_{dam}(Nb)	+.3	+1.2	t5.3	t7.3
	-.3	-1.1	-4.5	-6.1
σ_{He}(Nb)	t.3	+4.7	+8.9	+10.6
	-.3	-4.2	-7.5	- 8.9

* The percentage change, PC, was averaged over the twelve positions shown in Figure 5.

TABLE 8

SPECTRAL-AVERAGED CROSS SECTIONS FOR COPPER WITHIN THE TEST VOLUME; E_d = 35 MeV; UNIFORM SOURCE - CARTER

Position				Unperturbed				Perturbed			
#	X (cm)	Y (cm)	Z (cm)	ϕ (10^{+14} n/cm^{2}s)	E_n (MeV)	σ_{dam} (10^{+4} eV·b)	σ_{He} (b)	ϕ (10^{+14} n/cm^{2}s)	E_n (MeV)	σ_{dam} (10^{+4} eV·b)	σ_{He} (b)
1	0	0	0	14.1	11.4	24.2	.06?5	15.4	10.0	?2.0	.0525
2	0	3.?	0	11.1	11.2	23.9	.05?1	12.1	9.20	?1.5	.0504
3	6	0	0	2.75	12.0	25.1	.0?49	2.17	1?.1	21.9	.0534
4	6	3	0	2.11	11.9	25.0	.0?41	1.66	?.95	21.7	.0523
5	6	6	0	0.83?	11.5	24.4	.0?14	0.76?	?.35	20.8	.04?5
6	12	?	0	1.19	12.3	25.5	.0666	0.75?	10.4	22.2	.0552
7	12	?	0	0.66?	12.0	25.0	.0644	0.44?	10.0	21.?	.052?
8	?	0	2	1.31	11.7	24.7	.0628	1.28	9.52	21.1	.0498
9	?	3	2	1.10	11.7	24.7	.0629	1.07	9.63	21.2	.0502
10	?	6	2	0.544	11.5	24.4	.0612	0.574	9.?5	20.6	.0478
11	12	?	2.5	0.721	12.0	25.1	.0645	0.522	?.??0	21.5	6?21
12	12	?	2.5	0.460	12.0	25.0	.0645	0.338	?.??0	21.6	6?25

TABLE 9

SPECTRAL-AVERAGED CROSS SECTIONS FOR NIOBIUM WITHIN THE TEST VOLUME; E_d = 35 MeV; UNIFORM SOURCE - CARTER

Position				Unperturbed				Perturbed			
#	X (cm)	Y (cm)	Z (cm)	ϕ (10^{+14} n/cm^{2}s)	E_n (eV)	σ_{dam} (10^{+4} eV·b)	σ_{He} (b)	ϕ (10^{+14} n/cm^{2}s)	E_n (MeV)	σ_{dam} (10^{+4} eV·b)	σ_{He} (b)
1	0	0	0	14.1	11.4	21.7	.00736	15.4	10.0	19.8	.00632
2	0	3.5	0	11.1	11.2	21.4	.00716	12.1	9.80	19.3	.00602
3	6	0	0	2.75	12.0	22.5	.00816	2.17	10.1	19.8	.00655
4	6	3	0	2.11	11.9	22.4	.00790	1.66	9.95	19.5	.00639
5	6	6	0	0.832	11.5	21.8	.00748	0.768	9.35	18.7	.00584
6	12	0	0	1.19	12.3	22.8	.00828	0.758	10.4	20.0	.00687
7	12	5	0	0.662	12.0	22.4	.00794	0.44	10.0	19.6	.00689
8	6	0	2	1.31	11.7	22.1	.00770	1.28	9.56	19.0	.00602
9	6	3	2	1.10	11.7	22.1	.00771	1.07	9.63	19.1	.00609
10	6	6	2	0.544	11.5	21.8	.00746	0.574	9.25	18.6	.00574
11	12	0	2.5	0.721	12.8	22.4	.00786	0.522	9.90	19.4	.00639
12	12	3	2.5	0.460	12.9	22.5	.00803	0.338	9.75	19.5	.00645

I. PROGRAM

Title: Dosimetry and Damage Analysis
Principal Investigator: L. R. Greenwood
Affiliation: Argonne National Laboratory

II OBJECTIVE

To determine the sensitivity of calculated damage parameters to uncertainties in neutron flux/spectra

III. RELEVANT DAFS PROGRAM TASK/SUBTASK

SUBTASK II. A.3.1 Evaluate damage parameter sensitivity to flux/spectra uncertainties.

IV. SUMMARY

The SANDANL Monte Carlo error analysis code for spectral unfolding has been modified to produce a complete error corvariance matrix. This matrix is then used with the DISCS and SPECTRE codes to determine the errors in all calculated damage parameters. The codes can be used in any type of spectrum for energies below 20 MeV.

V. ACCOMPLISHMENTS AND STATUS

Development of Error Analysis Code -- L. R. Greenwood (ANL)

It is important in the near term to assess accuracy requirements for dosimetry at accelerator neutron sources. In particular, we must determine how accurately integral damage parameters can be measured. These parameters, such as displacements-per-atom (DPA), primary-knock-on-atom (PKA) distributions, and gas and transmutant generation rates, are cal-

culated from unfolded neutron spectra. Hence, any errors in nuclear cross-sections or activation measurements will propagate directly to the derived damage parameters.

Kecent improvements in our computer codes now allow us to determine the errors in all calculated, integral parameters due to uncertainties in nuclear data, activation measurements, or input starting spectra. Errors in the displacement cross-sections themselves are not included since they are relatively unknown but independent of our measurements. The SANOANL Monte Carlo error analysis code has been modified to generate a complete covariance error matrix for all unfolded spectra. This is done following the Monte Carlo unfolding by calculating the relative cross-correlations Cij between all energy qroups i and j:

$$C_{ij} = \frac{\frac{1}{N}\sum_{k=1}^{N} (\phi_{ki} - \bar{\phi}_i)(\phi_{kj} - \bar{\phi}_j)}{\sigma_i \sigma_j}$$

where k runs over the N Monte Carlo trials, ϕ_{ki} is the k^{th} solution for energy group i, $\bar{\phi}_i$ is the mean flux for group i, and σ_i is the standard deviation from the mean flux for group i. If i = j, then Cii = 1.0 and complete anti-correlation would result in Cij = -1.0. We thus compute the covariance effects in the output flux spectrum, although we are neglecting possible covariance effects in the input data. However, these input effects are probably small and are not well-known at present.

In practice we find that the covariance effects are strongly dominated by variations in the input spectrum. Smoothing in the flux iterations guarantees that nearby flux groups are highly correlated and variations in the spectral shape are also correlated to maintain smooth spectra. If the input spectrum is not perturbed, then the covariance effects are much reduced and show local competitions for flux between overlapping reactions. Errors in activation measurements are almost always less than 5% and hence have little effect on the results since

cross-section errors are typically 10-50%.

The covariance error matrix is then read into our code SPECTRE which generates spectral-averaged damage parameters using displacement cross-sections generated by the DISCS code. Figure 1 shows a typical error analysis for a neutron spectrum unfolded at the ANL Tandem Van de Graaff accelerator using the $^{9}Be(d,n)$ reaction at E_d = 16 MeV.[1] Table 1 gives a brief example of the errors produced in the damage parameters due to the unfolding uncertainties shown in figure 1. As can be seen, the integral errors in Table I are significantly less than the errors in the differential fluxes (figure 1) due to the strong covariance effects. The SPECTRE code routinely includes all significant cross-sections for 21 elements. The PKA distribution has been collapsed from a 100 energy group calculation.

The small errors in Table I indicate that our present technique is capable of determining damage parameters with relatively high accuracy, 5-10%. This is to be expected since our highly accurate activation measurements are integral measurements, as are the damage parameters. Differential flux errors thus tend to wash out as long as the integral measurements cover the entire energy spectrum and are reasonably self-consistent.

VI. REFERENCES

1. L. R. Greenwood, R. R. Heinrich, R. J. Kennerley, and R. Medrzychowski, Development and Testing of Neutron Dosimetry Techniques for Accelerator Based Irradiation Facilities, accepted for publication in Nuclear Technology.

VII. FUTURE WORK

At present our calculations are limited to 20 MeV since our displacement calculations are derived directly from ENDF/B-IV. We plan to

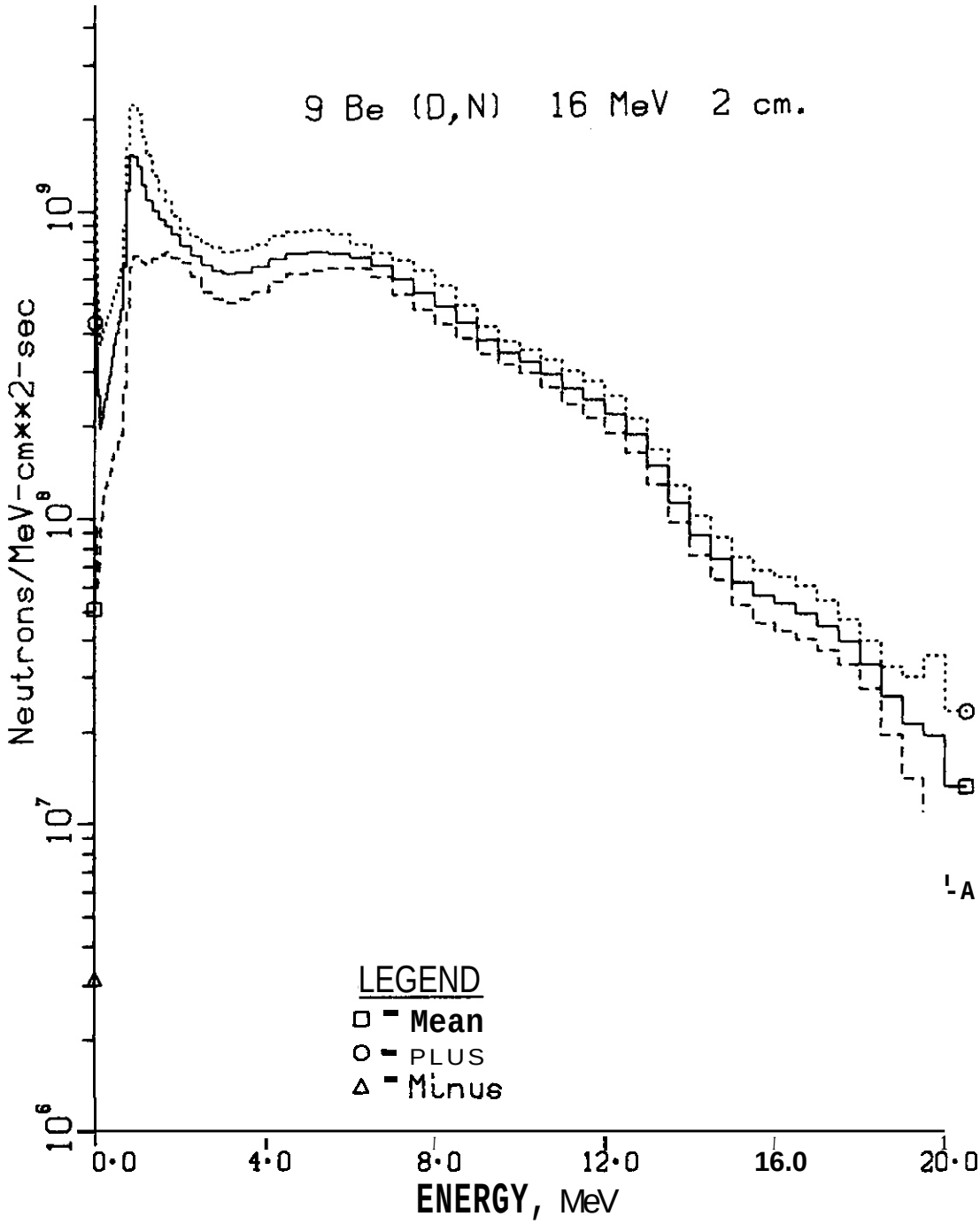

FIGURE 1. Error analysis for $^{9}Be(d,n)$ field at E_d = 16 MeV, 2 cm from the source. The dashed lines represent one standard deviation.

TABLE I: ERROR ANALYSIS FOR ANL TANDEM VAN DE GRAAFF

$^{9}Be(d,n)$ E_d = 16 MeV, R = 2.01 cm, $\bar{I}$ = 1.02 μA

$\Phi = 7.9 \pm 0.5 \times 10^{9}$ n/cm^{2}sec

Element	DPA[a] (10^{-11}/sec)	< H >[b] (10^{-11}ppm/sec)	<He>[b] (10^{-11}ppm/sec)
Al	1.44 ± .11	30.2 ± 2.2	20.3 ± 1.5
Ni	1.24 ± .09	20.3 ± 1.6	40.1 ± 2.8
Nb	1.07 ± .08	7.56 ± 0.52	1.26 ± 0.09

PKA[c] Energy Range (keV) — Primary Knock-on Atoms (%)

PKA Energy Range (keV)	Al	Ni	Nb
<1	1.2 ± 0.2	3.3 ± 0.5	5.5 ± 0.7
1 - 10	9.7 ± 1.4	20.1 ± 1.8	31.6 ± 5.2
10 - 40	22.9 ± 4.1	30.8 ± 2.5	30.0 ± 4.7
40 - 100	23.8 ± 3.3	20.3 ± 1.6	19.6 ± 1.4
100 - 300	23.4 ± 1.7	18.8 ± 1.1	12.3 ± 0.5
>300	19.1 ± 0.9	6.7 ± 0.3	0.9 ± 0.04

[a] Displacements-per-atom

[b] Gas generation rates do not include secondary reactions such as $(n,n\alpha)$

[c] Energy distribution of primary displaced atoms (collapsed from 100 groups).

extend the calculations to higher energies for a few materials using recent cross-section calculations done at Oak Ridge National Laboratory. This will allow us to study the spectra expected at FMIT as well as current work at the University of California at Davis.

VIII. PUBLICATIONS

None

I. PROGRAM

Title: Synergistic Helium Production by Boron Doping of Splat Cooled Alloys

Principal Investigator: O. K. Harling

Affiliation: Nuclear Reactor Laboratory, Massachusetts Institute of Technology

II. OBJECTIVE

This work is directed toward the development of better simulation techniques for the synergistic production of helium and displacement damage in first wall structural materials.

III. RELEVANT DAFS PROGRAM PLAN TASK/SUBTASK

A number of tasks are relevant since adequate experimental simulation of fusion reactor irradiation effects is a major reason for the DAFS program. Some of the tasks/subtasks which are significantly affected are:

TASK II.A.4 Gas Generation Rates
II.A.5 Technique Development
II.B.3 Experimental Characterization of Primary Damage State
II.C.2 Effects of Helium on Microstructure
II.C.8 Effects of Helium and Displacements on Fracture

IV. SUMMARY

Efforts during this, the first quarter of this project, have emphasized the development of techniques for the spacial characterization of boron in rapidly quenched, splat cooled, boron doped alloys. Resolutions of $\sim$0.3 μm have been attained by use of electron microscopy on plastic replicas which contain the boron fission tracks. Initial results of characterizing the boron distribution insnlattedand air cooled *ss*, indicates that there is no grain boundary segregation for boron contents

of 100 and 500 atomic parts per million. Heat treatment for 90 minutes at 575°C also failed to induce measureable segregation at these boron concentrations.

A series of measurements and reactor physics calculations has been completed to characterize the fast neutron fields in the in-core testing facilities of the M. I. T. Research Reactor. These facilities will be used for future low flux irradiations of boron doped samples as well as for other tests relevant to FR materials development.

V. ACCOMPLISHMENTS AND STATUS

A. Boron Doping of Stainless Steel by Rapid Quenching - S. West, A. Fadaai and 0. Harling (M. I. T.)

1. Introduction

It is generally understood that existing irradiation facilities i.e. accelerators and fission reactors will have to be used for the initial irradiation testing of fusion reactor (FR) structural materials. Damage rates and helium production rates should simulate the expected rates in FR's. Only fission reactors offer the required large testing volumes with fast neutron fluxes which produce damage rates which equal or exceed those expected for near term FR's. Helium production rates, with the exception of nickel alloys in mixed spectrum reactors, cannot be reproduced by direct nuclear reaction on the alloy constituents. The present studies are directed toward the development of techniques for the production of helium during fission reactor irradiations. Current efforts emphasize the doping of structural alloys with boron. To assure the uniform distribution of boron, the alloy is produced by rapid quenching from the melt. Cooling rates of 10^5 - 10^9°C/sec offer the possibility of uniform boron concentrations which are much higher than those which can be maintained without segregation during normal solidification rates. The usefulness of this approach to boron doping will also depend upon the

maintenance of a uniform boron distribution during thermo-mechanical consolidation, and during the use of the consolidated material in the temperature, stress and radiation environment of the fission reactor. Furthermore, the effect of boron on the physical properties of the boron doped alloys, whether segregated to grain boundaries or uniformly distributed, must be understood.

This quarterly report deals with our efforts to develop techniques for the spacial determination of boron in alloys and summarizes the status of other work related to this project.

2. The Spacial Characterization of Boron

Neutron autoradiography has previously been found to be a useful method of determining[1-5] the three dimensional distribution of boron in metal alloys. We have applied this technique for the spacial characterization[6] of boron in splat cooled samples of stainless steel. Thin films (∿50μm) of cellulose acetate butyrate were placed into intimate contact with polished boron doped ss samples and then irradiated, in the MITR-II, in a highly thermalized neutron flux. The damage tracks produced by the energetic a's and Li ions from the $^{10}B\ (n,\alpha)\ ^{7}Li$ reaction were developed by etching with KOH. Observation of the damage tracks was by optical microscopy, scanning electron microscopy (SEM) and transmission electron microscopy (TEM).

Specimens with 100, *500* and *24,500* appm (0.5% by weight) boron were examined by neutron autoradiography. Splat cooled specimens, grain size ∿2μm, had 100 and 500 appm boron. Conventionally cooled specimens with 500 and *24,500* appm had grain sizes of 10 - 25μm. The *24,500* appm, slowly cooled specimen, was expected to have boron segregation to the grain boundaries and this was clearly observed, see Figure 1. No segregation was observed in the TEM examination of plastic film replicas of the boron tracks in air cooled as well as splat cooled SS, aged 90 minutes at 575°C, and doped with 100 and 500 appm B. Figures 2 and 3

show these results for the splat cooled and air cooled specimens. No segregation is observed for the 100 and 500 appm specimens. The spacial resolution for these TEM autoradiographs is about 0.3μm. This resolution will probably be adequate for characterization of boron in splat cooled metals for grain sizes down to about 2μm. Scanning electron microscopy was also used to observe the fission damage tracks in the replica foils. The results were consistent with those obtained with TEM.

Optical microscopic examination of autoradiographic foils gave good results but was limited to a resolution of ~1μm which is inadequate for fine grained materials. Scanning transmission electron microscopy (STEM) was also used to examine the specimens and precipitate particles which were extracted from air cooled specimens with 500 appm B. Electron energy loss spectroscopy was used to analyze for boron content in the extracted particles. No boron at the detection sensitivity of the STEM was observed in the few particles which were examined in this manner.

3. Neutron Flux Characterization in the MITR-II

An extensive series of dosimetry measurements has been completed to characterize the fast neutron flux intensity and spectral shape in the in-core irradiation positions of the MITR-II. The MITR-II, which has an undermoderated core, a fast neutron flux of $\sim 10^{14}$ with estimated average fast neutron damage energy in excess of that in FFTF, will be used for low fluence irradiations in this project. Dosimeters of Al, Ni, Fe and Cu were activated by placement in the in-core facilities. Gamma ray counting from activities produced in the following high energy threshold reactions, $^{58}Ni(n,p)^{58}Co$, $^{54}Fe(n,p)^{54}Mn$, $^{63}Cu(n,\alpha)^{60}Co$ and $^{27}Al(n,\alpha)^{24}Na$, is completed. A complete fast neutron flux profile is being generated from these activation data. Calculations using the code CITATION[7] are being used to determine the fast neutron flux distribution for other configurations of the in-core facilities than those for which the base line dosimeter measurements were made.

VI. REFERENCES

1. Hughes, J. D. H., and Rogers, G. T., J. Inst. Met. 95 (1967):299

2. Kawasaki, S., Hishihuma, A. and Nagasaki, R., J. Nucl. Mat. 39 (1971):166.

3. Tanaka, M., and Kawasaki, S., J. Nucl. Mat. 48 (1973):336.

4. Blen, J. D., and Glas, A., J. Nucl. Mat. 48 (1973):336.

5. Hughes, J. D. H., Dewey, M. A. P., and Briers, G. W., Nature 223 (1969):498.

6. "Determination of 3-D Boron Distribution", Abolghaasem Fadaai, A thesis submitted in partial fulfillment of the requirements for a MS in Nuclear Engineering and Material Science and Engineering at the Massachusetts Institute of Technology, June 1978.

7. CITATION is a multi-group slowing down code based upon the diffusion equation.

VII. FUTURE WORK (Near Term)

Refinement of the 3-D boron characterization technique is planned. In the near future high resolution (0.2 μm) auger electron spectroscopy and scanning secondary ion mass spectroscopy will become available at M. I. T. and these techniques will also be examined for their suitability in characterizing boron distributions in our boron doped materials.

The analysis of the neutron radiation dosimetry will be completed and a fast neutron flux map developed for in-core facilities of the MITR-II.

An optimum mechanical property test will be designed to determine the effects of boron in the boron doped alloys.

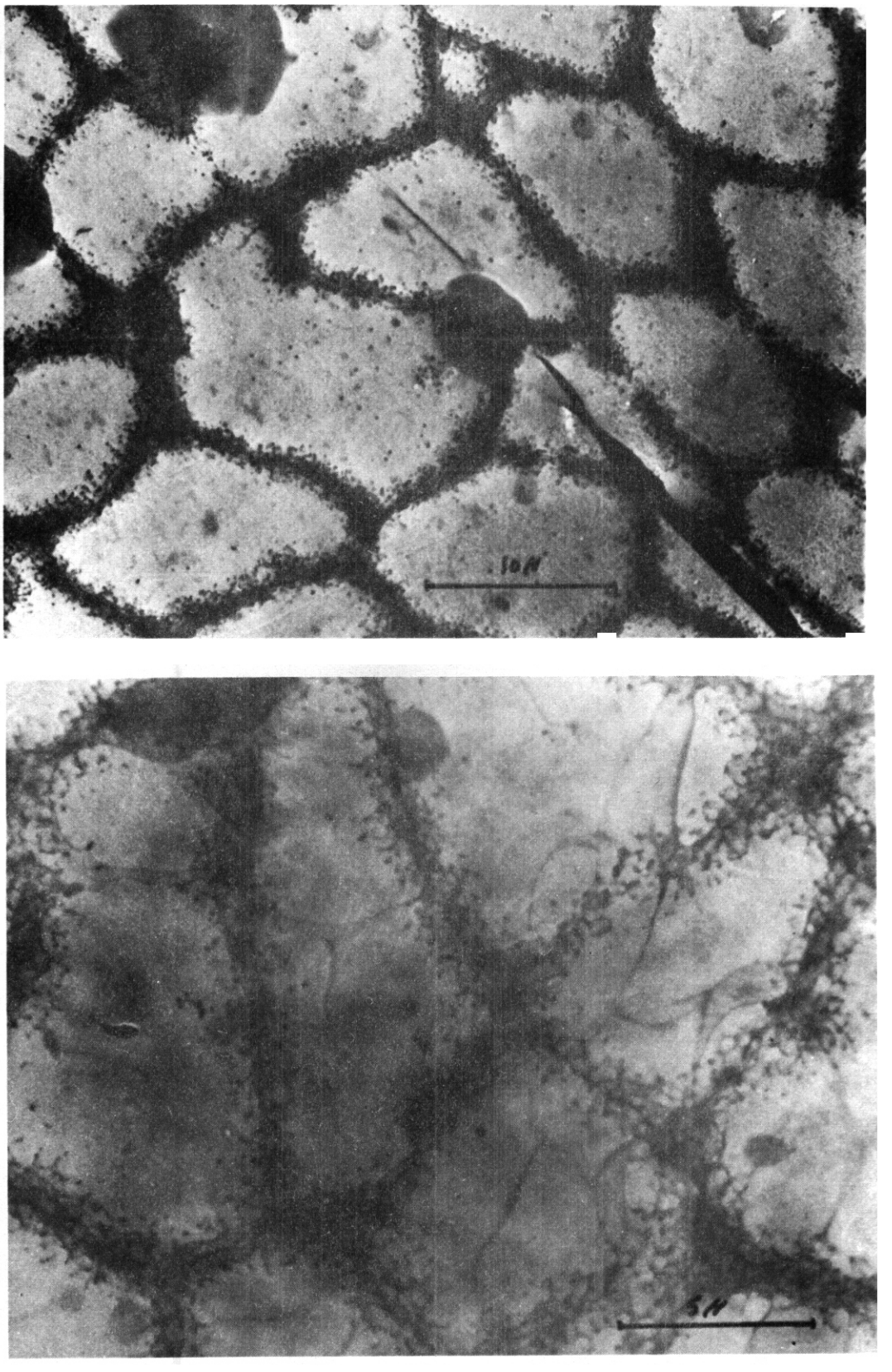

FIGURE 1. TEM autoradiographs of 316 SS with 0.5 wt. % B. *The* fluence is 2.4×10^{13} n · cm^{-2}; (a) 3000x, (b) 6000x.

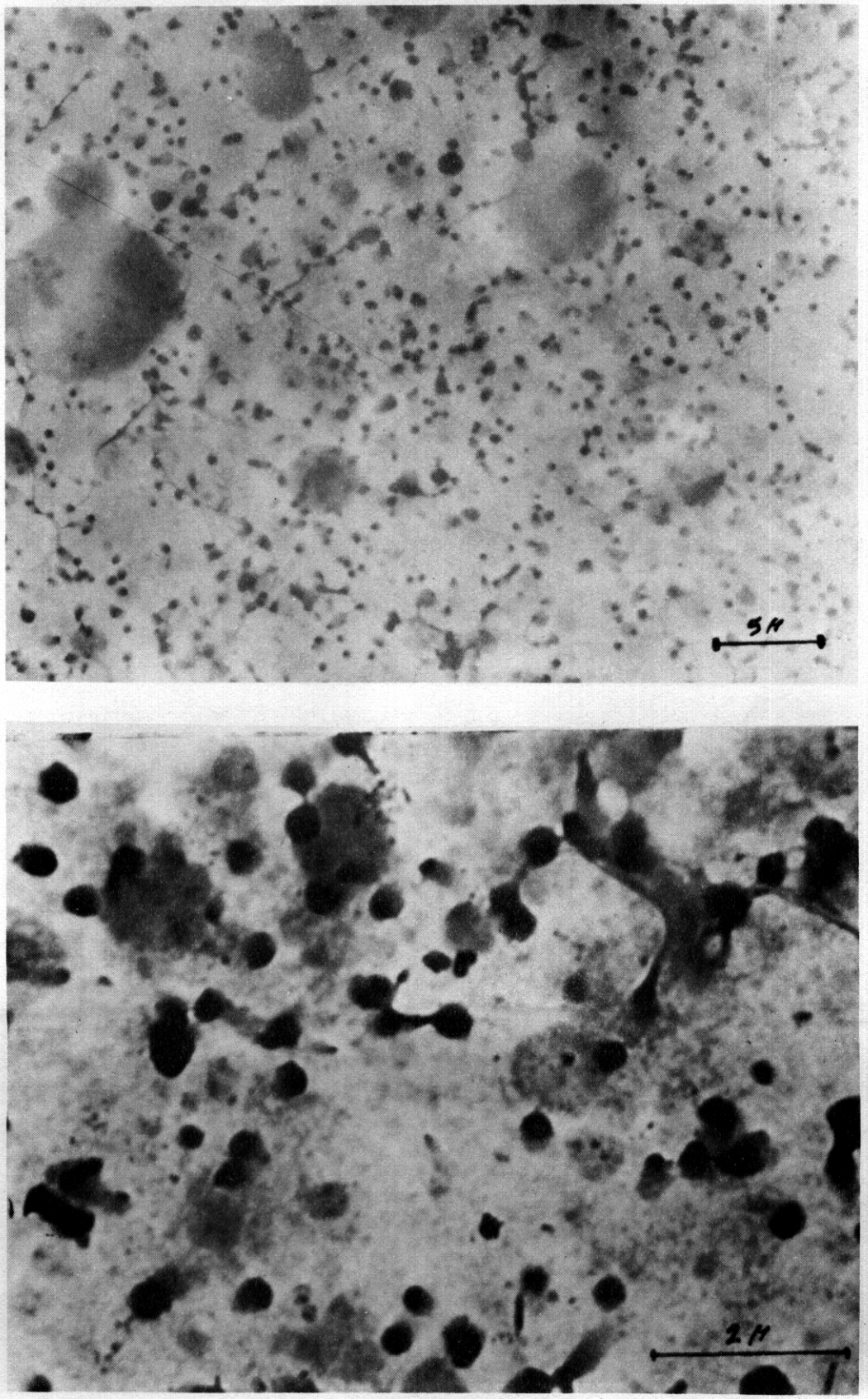

FIGURE 2. Boron distribution in a heat-treated, (90 min at 575°C) splat-cooled 316 SS; (a) 500 appm B, 3000x; (b) 100 appm B; 15000x. TEM

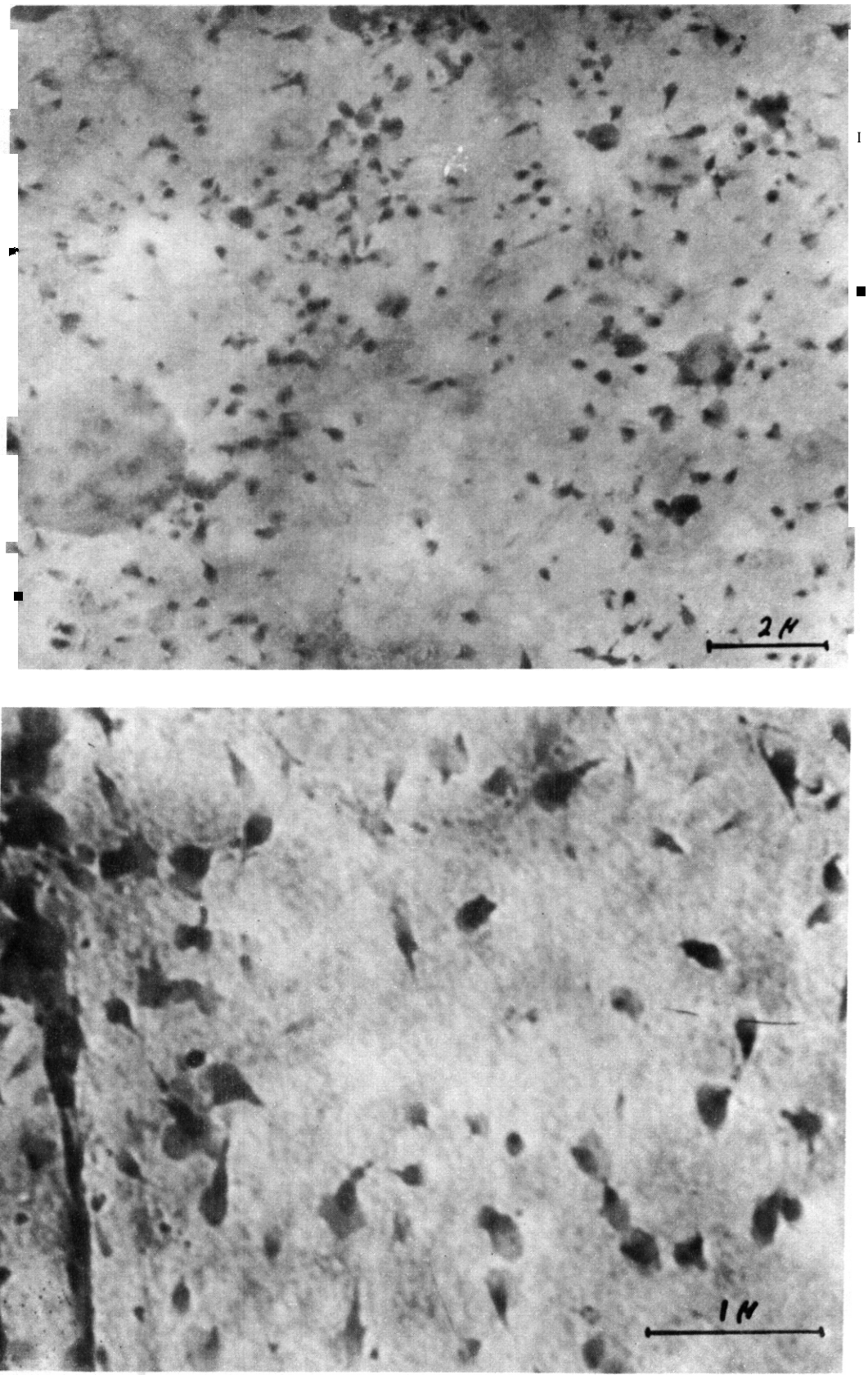

FIGURE 3. TEM boron autoradiographs of an air-cooled, heated (90 min at 575°C) 316 SS with 500 appm B showing uniform boron distribution; (a) 9000x; (b) 27000x. TEM

I. PROGRAM

Title: Helium Generation in Fusion Reactor Materials
Principal Investigators: O. W. Kneff, Harry Farrar IV
Affiliation: Energy Systems Group, Rockwell International

II. OBJECTIVE

The objectives of this work are tc measure helium generation rates *of* materials for Magnetic Fusion Reactor applications in a 14.8-MeV T(d,n) neutron field, and to develop helium accumulation fluence monitors for neutron fluence and energy spectrum dosimetry for long-term irradiations in fusion program neutron environments.

III. RELEVANT DAFS PROGRAM PLAN TASK/SUBTASK

SUBTASK II.A.4.2 T(d,n) Helium Gas Production Data
SUBTASK II.A.5.1 Helium Accumulation Monitor Development

IV. SUMMARY

Helium analyses have been initiated for the pure elements irradiated in the second Rockwell International T(d,n) irradiation at the Rotating Target Neutron Source (RTNS-I) at Lawrence Livermore Laboratory (LLL). The analyses completed to date include 41 specimens from seven pure element wire rings (Al, Ti, Ni, Cu) incorporated in the experiment for both cross section and helium accumulation dosimetry applications. The weighing was completed for the segmented radiometric foils, and the results were transmitted to Argonne National Laboratory (ANL) for incorporation with the radiometric counting results.

V. ACCOMPLISHMENTS AND STATUS

Helium Analyses of T(d,n) - Irradiated Pure Elements -- D. W. Kneff, Harry Farrar IV, and M. M. Nakata (Energy Systems Group, Rockwell International)

An extensive set of helium-generation and neutron dosimetry materials was irradiated in January 1977 in the T(d,n) neutron environment of the RTNS-I facility at LLL. The primary objectives of this irradiation were to measure the spectrum-integrated helium-generation cross sections of a large number of pure elements, separated isotopes, and alloys of potential fusion reactor design interest, and to further develop the use of helium accumulation materials as neutron fluence dosimeters. Radiometric dosimetry for this experiment was included by personnel from ANL and LLL.

The experiment has been described in detail elsewhere.[1] The irradiation assembly consisted of a small capsule, mounted on the outside face of the tritium target assembly. It contained two layers of multiple helium-generation specimens sandwiched between layers of dosimetry foils, as shown schematically in Figure 1. The ten Al, Ti, Fe, Ni, Cu, and Au wire rings, irradiated concentric with the capsule axis, will provide both cross section information and most of the helium accumulation fluence dosimetry for this experiment. They are the first materials from this irradiation to be analyzed.

The wire rings were prepared for helium analysis by acid etching to remove all possible α-recoil surface effects, and by segmenting each ring into multiple pieces for individual analysis. This analysis procedure will provide detailed information on the neutron fluence profile, as demonstrated for the first Rockwell International RTNS-I irradiation.[2]

To date, 41 segments of seven of the wire rings have been analyzed for helium in the Rockwell International high-sensitivity gas mass

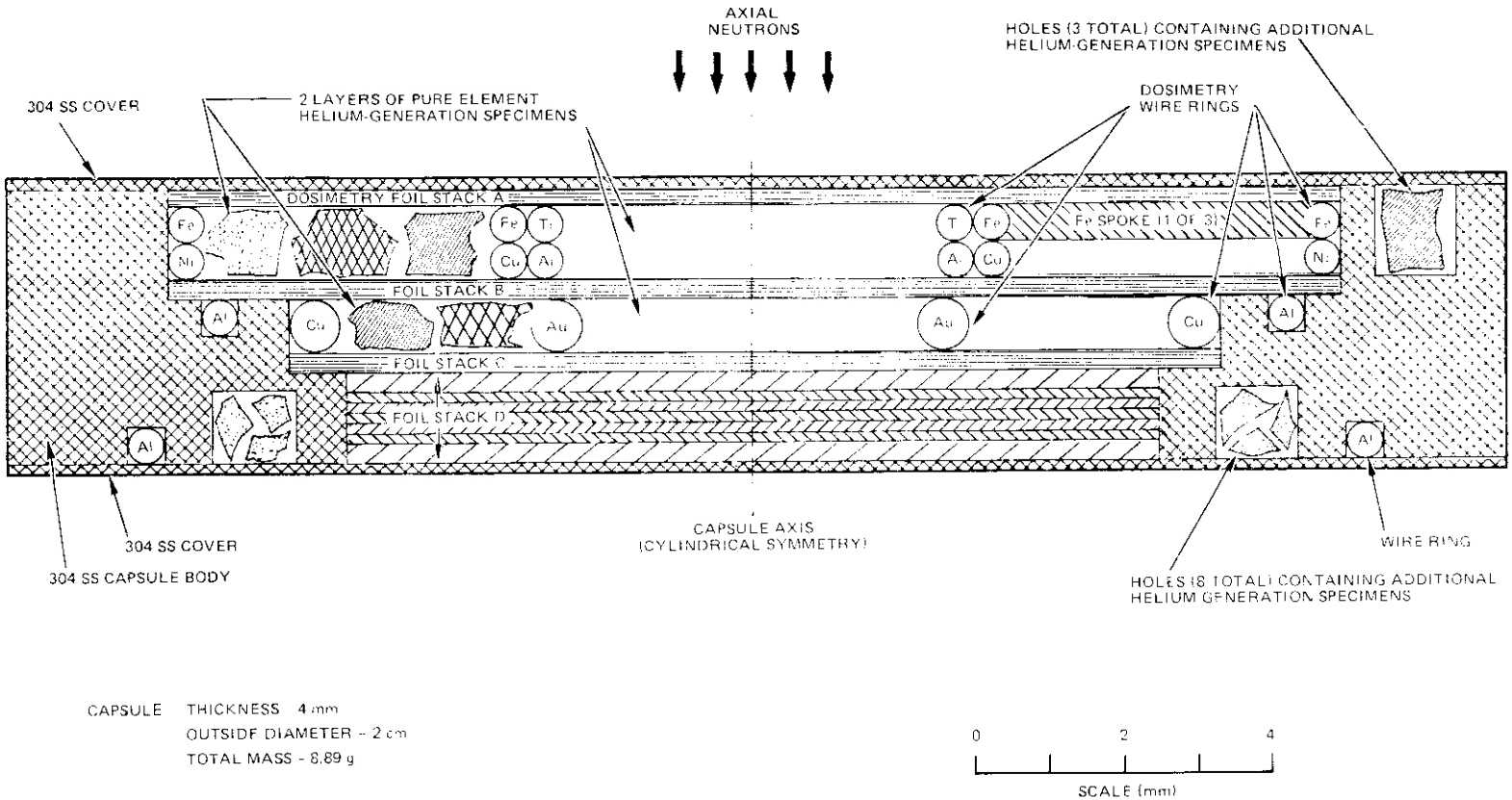

CAPSULE THICKNESS 4 mm
OUTSIDE DIAMETER - 2 cm
TOTAL MASS - 8.89 g

0 2 4
SCALE (mm)

FIGURE 1. Cross Sectional View of T(d,n) Irradiation

spectrometer. The results are given in Table 1. The segments represent various locations around each ring. These initial results show that the capsule axis was offset from the tritium target assembly axis, as observed from autoradiographs made after the irradiation. The analysis of selected segments of all ten helium dosimetry rings is continuing, and will effectively cover the irradiation volume for later fluence mapping.

The segmented radiometric dosimetry foils for this experiment have all been weighed, using mass standards traceable to the National Bureau of Standards. These weighing results will be combined with the ANL and LLL counting data to obtain the radiometric neutron dosimetry information for this experiment.

VI. REFERENCES

1. D. W. Kneff and H. Farrar IV, Helium Generation in Fusion Reactor Materials, Technical Progress Report for Period April-September 1977, AI-DOE-13219, Atomics International, Canoga Park, CA, January 1978.

2. O. W. Kneff and H. Farrar IV, "Helium Generation in Fusion Reactor Materials," Contributions to the Damage Analysis and Fundamental Studies Periodic Technical Progress Report for the Period October 1977 to March 1978 (in press).

VII. FUTURE WORK

The helium analyses of selected pure element wire ring segments will continue. The results will be combined with the radiometric foil results to construct a map of the neutron fluence profile over the experimental volume. The other materials irradiated in this experiment will be analyzed for helium, and the results will be combined with the fluence map to determine new helium-generation cross sections for 14.8-MeV neutrons.

TABLE 1

HELIUM CONCENTRATIONS IN T(d,n) - IRRADIATED PURE ELEMENT RING SEGMENTS

Ring	Sample	$\bar{\theta}$*	Mass (mg)	Atoms 4He	appb†
Al	FAL-W1A	58°	0.4829	2.428×10^{11}	22.52
Layer 1	FAL-W1C	304'	0.4962	2.848×10^{11}	25.74
	FAL-W1D	243'	0.6000	3.047×10^{11}	22.71
	FAL-W1E	179°	0.5513	2.442×10^{11}	19.84
	FAL-W1F	119°	0.5228	2.282×10^{11}	19.55
Al	FAL-W2A	71°	1.1162	2.582×10^{11}	10.36
Layer 2	FAL-W2C	7°	0.9260	2.731×10^{11}	13.21
	FAL-W2E	309'	0.8971	2.906×10^{11}	14.51
	FAL-W2G	256°	0.8635	2.550×10^{11}	13.23
	FAL-W2I	198°	0.9456	1.962×10^{11}	9.29
	FAL-W2K	138°	0.9677	1.743×10^{11}	8.07
Al	FAL-W3A	71°	1.4073	1.820×10^{11}	5.79
Capsule	FAL-W3E	305°	0.8809	1.334×10^{11}	6.78
Back	FAL-W3I	211°	0.9748	1.884×10^{11}	8.66
Ni	FNI-WA	80°	1.5898	1.217×10^{11}	7.46
Layer 1	FNI-WC	42°	2.4951	2.400×10^{11}	9.38
	FNI-WG	326°	1.7784	2.021×10^{11}	11.08
	FNI-WK	258°	1.4468	1.511×10^{11}	10.18
	FNI-WN	214°	2.2835	1.661×10^{11}	7.09
	FNI-WQ	152°	2.5890	1.465×10^{11}	5.52
	FNI-WS	114'	1.4299	8.613×10^{10}	5.87

(See next page for footnotes)

Continued . . .

TABLE 1 (CON.)

HELIUM CONCENTRATIONS IN T(d,n) -
IRRADIATED PURE ELEMENT RING SEGMENTS

Ring	Sample	e*	Mass (mg)	Atoms 4He	appb†
Ti	FTI-WA	39°	0.6636	5.894×10^{10}	7.06
Layer 1	FTI-WB	341°	0.6805	6.581×10^{10}	7.69
	FTI-WC	288°	0.5273	5.058×10^{10}	7.63
	FTI-WO	239°	0.5955	5.012×10^{10}	6.69
	FTI-WE	182°	0.7168	5.207×10^{10}	5.78
	FTI-WF	121°	0.6850	4.946×10^{10}	5.74
CU	FCU-W1A	73°	1.4362	1.025×10^{11}	7.54
Layer 1	FCU-W1C	14°	1.6254	1.359×10^{11}	8.83
	FCU-W1E	311°	1.3733	1.150×10^{11}	8.85
	FCU-W1G	251°	1.6487	1.224×10^{11}	7.84
	FCU-W1I	186°	1.2902	7.886×10^{10}	6.45
	FCU-W1K	131°	1.1535	6.976×10^{10}	6.38
Cu	FCU-W2AA	88°	3.7777	1.402×10^{11}	3.92
Layer 2	FCU-W2AO	57°	3.3714	1.460×10^{11}	4.57
	FCU-W28A	0°	4.2215	2.251×10^{11}	5.63
	FCU-W28D	329°	2.8646	1.566×10^{11}	5.77
	FCU-W2CA	269°	3.8551	1.960×10^{11}	5.37
	FCU-W2CD	241°	3.4659	1.533×10^{11}	4.67
	FCU-W2DA	177°	3.3243	1.096×10^{11}	3.48
	FCU-W2DD	148°	3.1530	9.887×10^{10}	3.31

*Average angular orientation of segment relative to capsule axis in plane of ring.

†Helium concentration in atomic parts per billion.

VIII. PUBLICATIONS

The following paper was presented to the American Nuclear Society Meeting in San Diego, CA, on June 20, 1978:

H. Farrar IV and D. W. Kneff, "Helium Generation in Twelve Pure Elements by 14.8-MeV Neutrons," Trans. Am. Nuc. Soc. 28, 197 (1978).

CHAPTER 4

SUBTASK B: DAMAGE PRODUCTION

No contributions this quarter.

CHAPTER 5

SUBTASK C: DAMAGE MICROSTRUCTURE EVOLUTION AND MECHANICAL BEHAVIOR

I. PROGRAM

Title: The Simulation of Oxide Dispersoid Stability in Irradiated Alloys

Principal Investigator: Kenneth C. Russell

Affiliation: Department of Materials Science and Engineering
Massachusetts Institute of Technology

II. OBJECTIVE

The objective is to model phase stability of dispersoid strengthened Al-Al_2O_3 and 316 SS-Cr_2O_3 alloys.

III. RELEVANT DAFS PROGRAM PLAN TASK/SUBTASK

SUBTASK II.C.1.2. Effect of Material Parameters on Microstructure/ Modelling and Analysis.

IV. SUMMARY

The Maydet and Russell[1] theory for phase stability under irradiation was used to evaluate the stability of chromium and aluminum oxides in 316SS and aluminum, respectively. The critical particle sizes were found to depend crucially on the sign of the precipitate misfit with the matrix. The vacancy supersaturation helps to stabilize the positive misfit nuclei, and the critical size increases with increasing temperature (because of the decrease in vacancy supersaturation). On the other hand, the vacancy supersaturation destabilizes the negative misfit particles, and the critical size decreases with increasing temperature. The solute supersaturation helps to stabilize the particles in either case, and higher solute supersaturation leads to smaller critical size particles.

V. ACCOMPLISHMENTS AND STATUS

A. Introduction

In an irradiation environment, thermal equilibrium is disturbed by the production of thermal spikes and displacement cascades. The high energy atoms can easily produce nonequilibrium phases or cause other phases to dissolve which exist in an equilibrium situation. Since the dissolution or redistribution of phases which serve as barriers to dislocations, such as oxide precipitates, alter the mechanical properties of structural components during operation of a reactor, the study of phase stability becomes important.

Al-Al_2O_3 alloys, consisting of an Al-matrix with Al_2O_3 particles, are considered interesting first wall materials since they have a small absorption cross-section for thermal neutrons, and they preserve good strength and resistance to corrosion up to high homologous temperatures. Another system which is considered here is 316SS with dispersed Cr_2O_3 particles. The 316SS is a candidate material for controlled thermonuclear reactor (CTR) first walls. The addition of Cr_2O_3 particles in the 316SS is to preserve the stability of the alloy's dislocation structure at high temperatures and, as a result, superior strength to above 0.55 to 0.65 of the melting point of the matrix.[2]

The purpose of the calculation is to predict the particle critical size under various irradiation conditions.

B. Theoretical Model

The theoretical model of Maydet and Russell[1] will be briefly reviewed. They considered spherical precipitates which are incoherent with the matrix, and are therefore good sinks for vacancies and interstitials. The matrix and the precipitate are binary

substitutional solutions dilute in solute and in solvent, respectively. The precipitate may then be characterized by two variables: the number of solute atoms (x) and the number of excess vacancies (n). Thus

$$n = a - x \tag{1}$$

where (a) is the number of matrix atoms displaced by the precipitate. A precipitate with a greater atomic volume than the matrix would thus tend to have n > 0. The behavior of a precipitate particle may then be described by its movement in a phase space of coordinates n and x.

The particle moves with a velocity equal to the frequency of addition times the jump distance - in this case, unity.

$$\dot{x} = \beta_x(n,x) - \alpha_x(n,x) \tag{2}$$

$$\dot{n} = \beta_v(n,x) - \alpha_v(n,x) - \beta_i(n,x) \tag{3}$$

where $\beta_x(n,x)$, $\beta_v(n,x)$ and $\beta_i(n,x)$ are the arrival rates of solute, vacancies, and interstitials, respectively. The β's are easily calculated from the concentrations and mobilities of the respective point defects.

$a_x(n,x)$ and $\alpha_v(n,x)$ are the rates of loss of solute and vacancies, respectively. Redenote the equilibrium number of (n,x)-mer as

$$\rho^\circ(n,x) = \Omega_m^{-1}\exp(-\Delta G(n,x)/kT) \tag{4}$$

where Ω_m = matrix atomic volume and $\Delta G^\circ(n,x)$ = free energy of forming the particle from n matrix vacancies and x solute atoms. Then detailed balancing gives

$$\beta_v(n-1,x)\rho^\circ(n-1,x) = \alpha_v(n,x)\rho^\circ(n,x) \tag{5}$$

$$\beta_v(n,x-1)\rho^\circ(n,x-1) = \alpha_v(n,x)\rho^\circ(n,x) \tag{6}$$

Replacing differences in $\Delta G^\circ(n,x)$ by derivatives gives

$$a_v(n,x) \approx \beta_v(n,x)\exp(1/kT)(\partial\Delta G^\circ(n,x)/\partial n) \tag{7}$$

$$\alpha_x(n,x) \approx \beta_x(n,x)\exp(1/kT)(\partial\Delta G^\circ(n,x)/\partial x) \tag{8}$$

The free energy change on forming a precipitate particle from a solid solution supersaturated with solute and vacancies has been calculated from the capillary model.[3]

$$\Delta G^\circ = -xkT \ln S_x - nkT \ln S_v + (36\pi\Omega^2)^{\frac{1}{3}}\gamma x^{\frac{2}{3}} + x\Delta g_s \quad (9)$$

where S_x = ratio of the actual and saturation concentrations of solute, S_v = ratio of the actual and saturation concentrations of vacancies, n = atomic volume of precipitate, γ = particle-matrix surface energy, Δg_s = strain energy per molecule of precipitate.

In the case where elastic properties of matrix and precipitate are equal, the strain energy per molecule becomes

$$\Delta g_s = \frac{\Omega E(\delta - n/x)^2}{9(1-\nu)} \quad (10)$$

where

$$\delta = \frac{\Omega - 5\Omega_m}{5\Omega_m} \quad \text{and} \quad 6 = \frac{n-2n_m}{2\Omega_m} \quad (11)$$

for substitutional and interstitial oxygen atoms, respectively.

Nodal lines are obtained by setting $\dot{x}$ and $\dot{n}$ individually equal to zero. Any particle on an $\dot{x}$ nodal line may have a velocity only in the n direction and vice versa. The particle has zero net velocity at a critical point.

For $\dot{n} = 0$

$$n = x\{\delta + (1/2B) \ln[S_v(1-\beta_i/\beta_v)]\} \quad (12)$$

For $\dot{x} = 0$

$$n = x\delta\{1 + A/B\ \delta^2 x^{1/3} - (1/B\delta^2) \ln S_x\}^{1/2} \quad (13)$$

The equations for the nodal lines are seen to be independent of the kinetic parameters, other than β_i/β_v which is actually energetic in nature. Furthermore, S_v and β_i/β_v appear only in $\dot{n} = 0$ and S_x appears only in $\dot{x} = 0$.

Simultaneous solution of Equations 12 and 13 shows that the critical point is located at an x^* and n^* given by

$$x^* = -32\pi\gamma^3\Omega^2/3(\Delta\phi)^3 \quad (14)$$

$$n^* = x^*[\delta + (1/2B) \ln S_v(1-\beta_i/\beta_v)] \quad (15)$$

or a radius of

$$r^* = -2\gamma\Omega/\Delta\phi \quad (16)$$

where $\Delta\phi$ is an irradiation-modified potential given by

$$\Delta\phi = -kT \ln S_x[S_v(1-\beta_i/\beta_v)]^{\delta} - (kT/4B)[\ln S_v(1-\beta_i/\beta_v)]^2 \quad (17)$$

If $\Delta\phi = 0$, the nodal lines do not intersect (for $x > 0$) and all particles will eventually decay. In the absence of excess defects $\Delta\phi = -kT\ln S_x$ and familiar Gibbs-Thomson equation is recovered from Equation 14.

C. Calculations and Results

Where possible, actual material values were used in the analysis. In the case of (316SS) alloy, the nominal composition of major alloying additions were assumed.

When the two kinds of atoms are more nearly of the same size, a substitutional solid solution is formed, in which the atoms of solute replace those of the solvent, so that the two occupy a common lattice. In the case at hand, $\delta < 0$ which means that there is a contraction around the precipitate, and as seen from Equation 17 the high vacancy supersaturation actually helps to shrink the precipitate by the chemical effect of vacancies and to lessen the stability of the phase. The opposing term then is solute supersaturation, which must overcome other terms and factors in order to stabilize the precipitate.

Figure 1 shows the critical particle size versus homologous temperature for 316SS with Cr_2O_3 precipitates. Figure 2 is the same except for the Al-Al_2O_3 system. Although the vacancy supersaturation in aluminum is less than 316SS, the critical size of Al_2O_3 in the aluminum matrix is larger than Cr_2O_3 in 316SS matrix. This is because of the smaller precipitate misfit in aluminum as compared to chromium oxide in the 316SS system.

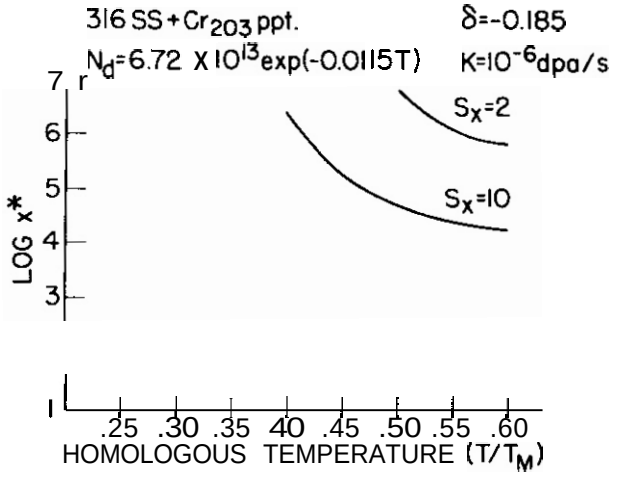

Fig. 1 Critical Particle Size Versus T/T_m in 316 SS Under Irradiation.

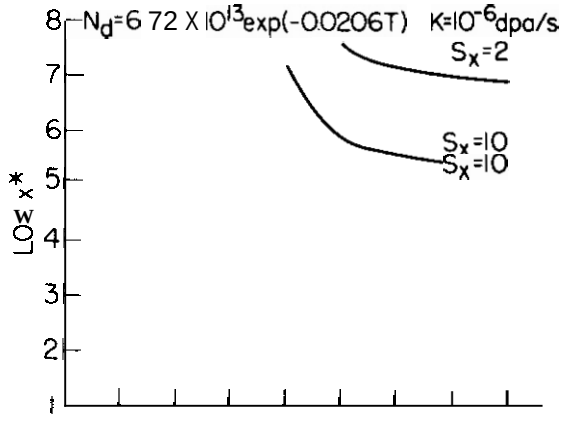

Fig. 2. Same as Figure 1 Except for Aluminum

Figures 1 and 2 are mapped to show the critical particle size of chromium and aluminum oxide particles versus homologous temperatures. It is seen that particles exist at high temperatures with solute supersaturation ($S_x > 1$), and the critical particle size increases with a decrease of temperature. This is due to the main effect of excess vacancies, which acts as a chemical component or a driving force to remove the solute atoms from the precipitates. At lower temperatures ($T < 0.45T_m$) the vacancy supersaturation is high enough to change the sign of irradiation modified free energy and give unstable precipitates.

Figures 3 and 4 are the same as Figures 1 and 2, except the displacement rate is 10^{-3}dpa/sec. It is obvious that this displacement rate produces higher vacancy supersaturations. As a result, for a particular homologous temperature, the critical particle size increases (when $\delta < 0$) compared to the previous condition of irradiation.

Figures 5 and 6 show the critical particle size versus homologous temperature for 316SS-Cr_2O_3 and Al-Al_2O_3 systems, respectively, for interstitial oxygen. When the oxygen occupies an interstitial site in the matrix, addition of an oxygen to the precipitate gives a large strain, so δ is strongly positive. The displacement rate as indicated on top of each graph is 10^{-6}dpa/sec. As is seen, there exist critical particle sizes for a wide range of temperatures, except for $Sx < 1$ at $T \geq 0.40T_m$ where the excess vacancies cannot compensate the solute undersaturation.

Figures 7 and 8 are the same as Figures 5 and 6, except for the displacement rate ($K = 10^{-3}$dpa/sec), which produces higher vacancy supersaturation in the alloy, and as a result, a smaller critical particle size compared to $K = 10^{-6}$dpa/sec. It is obvious that at high temperatures (where $S_v(1-\beta_i/\beta_v) \rightarrow 1$) the effect of solute supersaturation becomes highly significant. $\Delta\phi$ then becomes a function of solute supersaturation and temperature $\Delta\phi = -kT\ln S_x$. It is seen, however, that

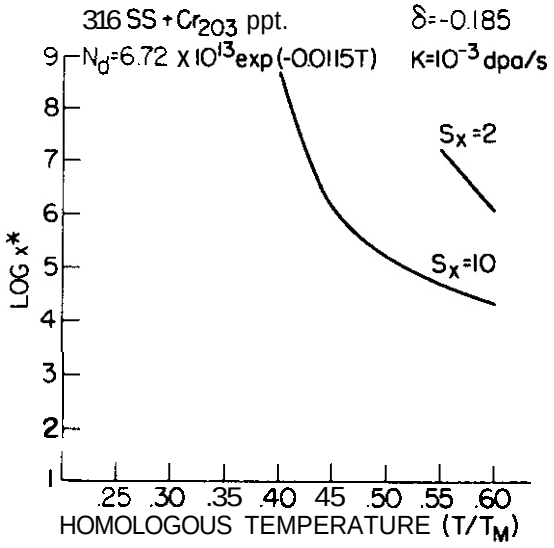

Fig. 3 Same as Figure 1 Except K = 10^{-3}dpa/s.

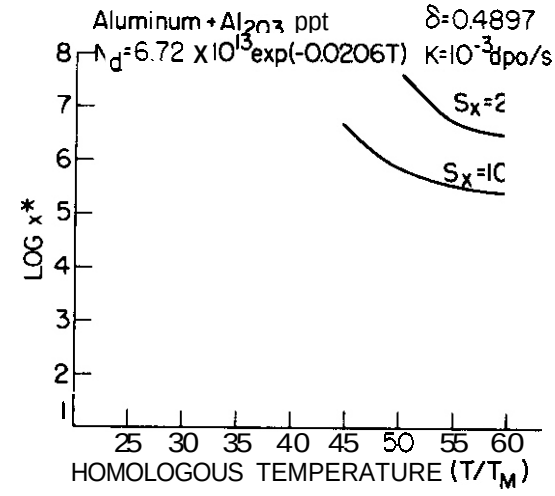

Fig. 4 Same as Figure 1 Except for Aluminum With K = 10^{-3}dpa/s.

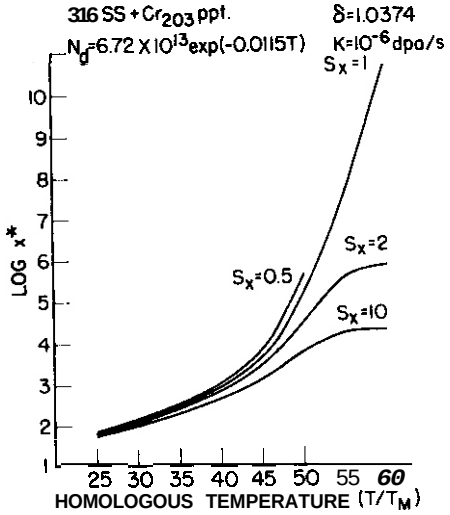

Fig. 5 Critical Particle Size Versus T/T_m in 316 SS Under Irradiation

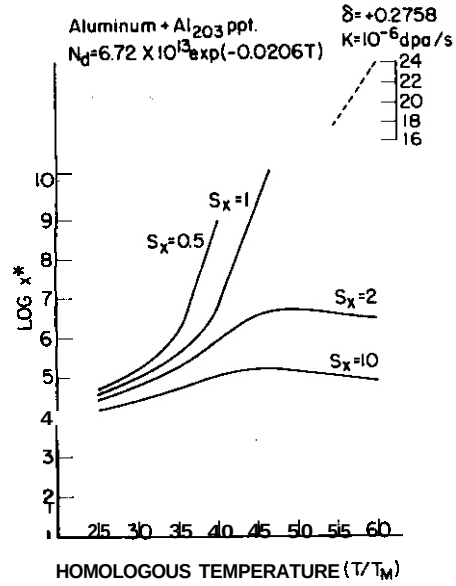

Fig. 6 Same as Figure 5 Except for Aluminum

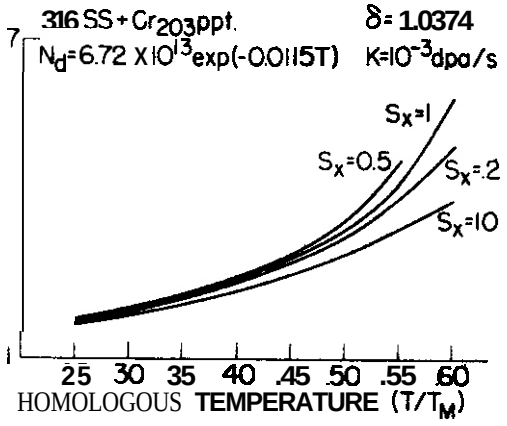

Fig. 7 Same as Figure 5 Except K = 10^{-3}dpa/s.

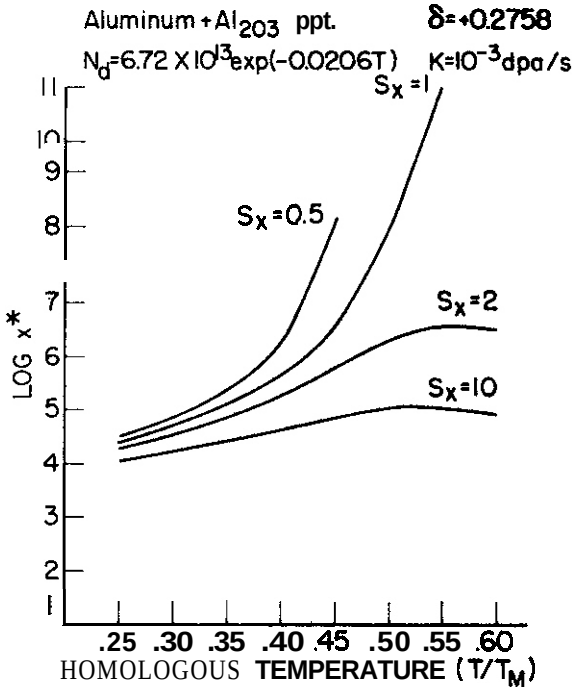

Fig. 8 Same as Figure 5 Except for Aluminum with K = 10^{-3}dpa/s.

the critical particle size increases with increasing temperature when ($\delta > 0$). For solute supersaturated solids ($S_x > 1$) the critical particle size increases up to a certain temperature and after that decreases. These conditions are due to competition between S_v and $(1-\beta_i/\beta_v)$: one term decreases (S_v) with increasing temperature, while the other term increases $(1-\beta_i/\beta_v)$.

VI. REFERENCES

1. S.I. Maydet and K.C. Russell, "Phase Stability Under Irradiation: Point Defect Effects", J. Nuclear Mats. 64, 101-114 (1977).

2. G. Mervin Ault and H.M. Burte in Oxide Dispersion Strengthening, Metallurgical Society Conferences, Vol. 47, p. 4 (1968).

3. K.C. Russell, "The Role of Excess Vacancies in Precipitation", Scripta Met. 3, 313-316 (1969).

VII. FUTURE WORK

Particle growth and decay rates will be calculated for steady-state and pulsed CTR conditions.

VIII. PUBLICATIONS

M. Saiedfar, "Simulation of Oxide Dispersoid Stability in Irradiated Alloys" in an S.M. Thesis, M.I.T., 1978.

I. PROGRAM

Title: Effects of Irradiation on Fusion Reactor Materials
Principal Investigator: F. V. Nolfi, Jr.
Affiliation: Argonne National Laboratory

II. OBJECTIVE

The objective of this work is to develop physically based models for microstructural evolution that occurs during simulated fusion-reactor irradiation.

III. RELEVANT DAFS PROGRAM PLAN TASK/SUBTASK

SUBTASK II.C.2.4 Modeling

IV. SUMMARY

Time-dependent interstitial- and vacancy-cluster number densities have been calculated for Ni-4 at. % Si using a nucleation model that has been modified to include interstitial trapping at Si atoms. Results are compared with experimental interstitial-loop number densities and sizes obtained by TEM examination of Ni-4 at. % Si irradiated with Ni^+ ions.

V. ACCOMPLISHMENTS AND STATUS

Microstructural Yodeling -- B. Okray Hall

1. Introduction

A comprehensive time-dependent nucleation and growth model that includes dislocation loops, voids, and helium bubbles is being developed to describe the effects of simultaneous helium production and displacement damage on microstructural evolution in metals. The modeling complements

the dual-ion irradiation studies and is designed to aid in interpretation of the experimental results.

2. Model Calculations

The basic interstitial- and vacancy-cluster nucleation model was modified to include interstitial trapping by an adaptation of the effective diffusion coefficient introduced by Schilling and Schroeder.[1] They considered impurities as immobile traps and derived an effective defect-diffusion coefficient D^+, dependent on trap concentration C_t, trapping time τ, and capture radius R_t. Use of the simplest form of interaction potential, a square well, was sufficient for our purposes; the capture radius of a single jump distance is assumed, and the trapping time is then inversely proportional to the jump frequency ν_t from the trap site to the nearest-neighbor site:

$$\nu_t = \nu_o \exp[-(E_m^I + E_B)/kT],$$

where ν_o is the attempt frequency (assumed equal to that in the pure metal), E_m^I is the interstitial motion energy, T is temperature, and E_B is the interstitial-solute binding energy. The effective diffusion coefficient is

$$D^+ = D_i/[1 + 4\pi C_t R_t D_i(\tau - \tau_o)],$$

where D_i is the interstitial diffusion coefficient in the pure metal, and τ_o is the "trapping" time at a host-atom site. The factor $(\tau - \tau_o)$ replaces the factor τ used in Ref. 1, since the earlier formulation neglected to consider that only trapping time in excess of the host-atom trapping time affects the diffusion coefficient.

Materials parameters used in the calculations are given in Table I. The temperature was 460°C, the displacement rate was

TABLE I. MODEL PARAMETERS

Quantity	Value
!Lattice constant, a	3.52×10^{-8} cm
Burgers vector, b	$a/\sqrt{2}$
Core radius, r_0	b/2
Poisson ratio, ν	0.34
Shear modulus, μ	7.85×10^{11} dyne/cm^2
Stacking fault energy, γ	400 erg/cm^2
Jump distance, d	2.49×10^{-8} cm
Vacancy formation energy, E_f^v	1.60 eV
Vacancy migration energy, E_m^v	1.28 eV
Vacancy frequency energy, ν_0^v	5×10^{13} s^{-1}
Interstitial formation energy, E_f^I	4.08 eV
Interstitial migration energy, E_m^I	5.15 eV
Interstitial frequency factor, ν_0^I	10^{13} s^{-1}

2.75 x 10^{-4} dpa-s^{-1}, the sink-annihilation probability was 10^{-6}, and the bias was 1.35.

The calculated number density, in atom fraction, for interstitial clusters of size ≥2 is plotted in Fig. 1 as a function of dose for pure nickel (E_B = 0) and for Ni-4 at. % Si alloys witn interstitial-solute binding energies of 0.25, 3.53, 3.75, and 1.00 eV. The plot shows that the calculated cluster number density increases strongly, and the cluster process slows, as binding energy increases.

The vacancy-cluster number density is affected through the decreased arrival rate of interstitials, and increases slightly with increasing binding energy.

3. Experimental Results

Experimental investigations on loop nucleation were performed by D. I. Potter under BES funding. Ni-4 at. % Si specimens were irradiated at ~465°C with 3.0-MeV $^{58}Ni^{+}$ ions. The ion flux of ~2.3 x 10^{11} ions-$cm^{-2}s^{-1}$ produced a peak damage rate of approximately 3 x 10^{-4} displacements per atom per second (dpa-s). After irradiation, specimens were sectioned at ~5000 Å from the surface and examined by TEM. Loops were observed under dynamical diffraction conditions with a <200> two-beam diffraction geometry [optimal conditions for sizing small Frank-faulted loops[2]]. Figure 2 shows the loop microstructures as a function of irradiation time at 465°C. The lowest dose, 0.05 dpa, produced loops with an average diameter of 56 Å [Fig. 2(a)]. The measured loop density at this dose was 4.78 x 10^{14} loops cm^{-3}. Irradiation to a higher dose of 0.11 dpa [Fig. 2(b)] increased the average loop diameter to 115 Å. The number density of 4.34 x 10^{14} loops cm^{-3} was essentially unchanged from its value at 0.35 dpa. Irradiation to higher doses of 0.35 dpa [Fig. 2(c)] and 3.67 dpa (not shown) produced average loop diameters of 302 Å and 341 Å, respectively, and measured number densities of 4.97 x 10^{14} and 4.87 x 10^{14} loops cm^{-3}. No voids were observed in any of the specimens.

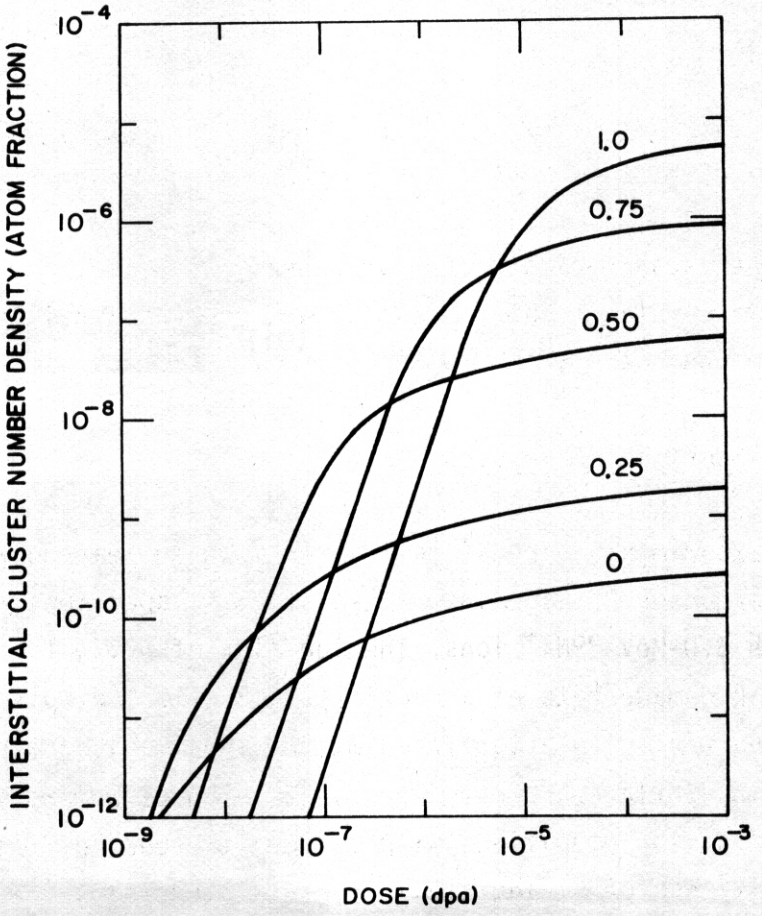

FIGURE 1. Calculated Interstitial-Cluster Number Density Versus Dose for Several Interstitial-Solute Binding Energies. T = 460°C, $\dot{n} = 2.75 \times 10^{-4}$ dpa-s^{-1}, $p = 10^{-6}$. Curves are labeled by binding energy in eV.

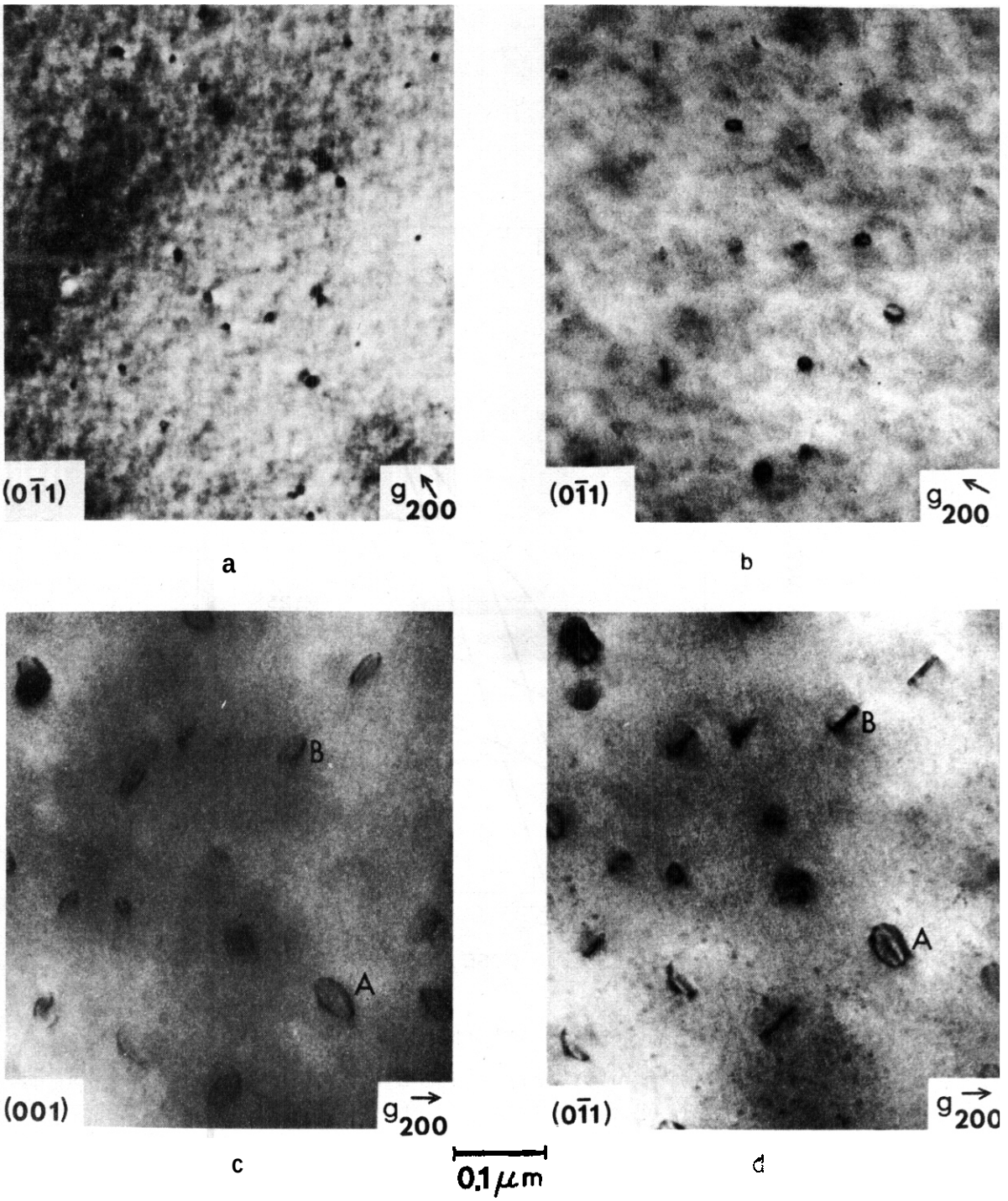

FIGURE 2. Dislocation Loop Microstructures Observed in Ni-4 at. % Si Irradiated at ∿465°C. (a) 0.053 dpa, w = **seg** ∿ 0; (b) 0.11 dpa, w ∿ 1.6; (c) 0.35 dpa, w ∿ 1.6, ∿(001) orientation; (d) same foil area as (c) with ∿(0$\bar{1}$1) orientation.

The geometry of the dislocation loops was investigated in detail and is briefly summarized in Figs. 2(c) and 2(d). These micrographs show the same foil area imaged under similar diffraction conditions but tilted into ~(001) orientation in Fig. 2(c) and ~(0$\bar{1}$1) orientation in Fig. 2(d). Such tilting experiments showed that all the loops were contained on {111} planes. Further, the images were used to identify the particular {111} planes of the loops being imaged; e.g., loops labeled A are on ($\bar{1}\bar{1}$1) while those labeled B are on ($\bar{1}$11). The sets of loops on the other two {111} planes are barely visible because of the particular diffraction conditions used to produce Figs. 2(c) and 2(d). The Tunstall criterion was used to establish that the loops are all interstitial in nature.

Loop-size distributions are plotted in Fig. 3 for the four low-dose Ni-4 at. % Si samples. The areas beneath the curves are approximately equal, reflecting the constant value of the loop number density with dose.

4. Comparison of Calculations and Experiment

In the Ni-4 at. % Si specimens examined, the interstitial-loop number density was constant at ~4.8 x 10^{14} cm^{-3}, i.e., 5.4 x 10^{-9} atom fraction, for doses between 0.05 and 0.6 dpa. From Fig. 1, the interstitial-solute binding energy should be ~0.25 eV, in good agreement with the value of 0.26 ± 0.06 eV obtained by Hossain and Brown[3], who performed HVEM experiments on pure Ni and dilute Ni-Si alloys. The observed average loop sizes, however, are consistent with higher binding energies and the associated delay in the clustering process.

5. Conclusions

In the present work, we have incorporated interstitial-solute trapping in a time-dependent nucleation and growth model and found that (1) the calculated interstitial-cluster number density depends

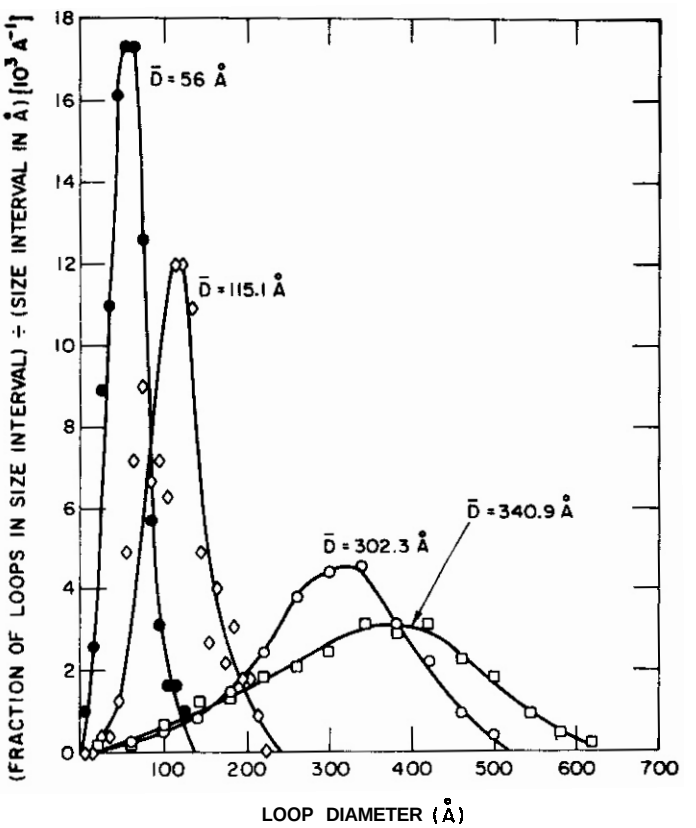

FIGURE 3. Dislocation Loop Size Distributions for Ni-4 at. % Si Specimens. (●) sample A-3, 0.053 dpa, T = 452°C; (x) sample B-3, 0.114 dpa, T = 469°C; (o) sample C-1, 0.33 dpa, T = 462°C; (□) sample D-1, 0.66 dpa, T = 464°C.

strongly on the choice of binding energy; (2) the time to reach saturation in interstitial-cluster number density increases as binding energy increases; and (3) the vacancy-cluster number density increases moderately as binding energy increases. The calculations were compared with experimental loop-number densities and size distributions obtained by TEM for a Ni-4 at. % Si alloy irradiated with Ni^+ ions to doses ranging from 0.05 to 0.6 dpa. The number-density data were consistent with an interstitial-solute binding energy of ~0.25 eV, but the average loop sizes were consistent with higher binding energies.

VI. REFERENCES

1. W. Schilling and K. Schroeder, Consultant Symposium on the Physics of Irradiation-produced Voids, R. S. Nelson, Ed., AERE-R7934, 1975, p. 212.

2. K. H. Katerbau, Phys. Status Solidi (a)38, p. 463 (1976).

3. M. K. Hossain and L. M. Brown, Rad. Effects 31, p. 203 (1977).

VII. FUTURE WORK

The time-dependent model will be expanded to include mobile helium and its effect on vacancy clustering. Parameterization of segments of the model will continue. Impurity effects on loop behavior will be examined further.

VIII. PUBLICATIONS

B. Okray Hall and O. I. Potter, "Microstructural Development during Low Dose Irradiation," accepted for publication in Proc. of the Ninth Intl. Symposium on Effects of Radiation on Structural Materials, Richland, WA, July 1978.

I. PROGRAM

Title: Mechanical Properties
Principal Investigator: R. H. Jones
Affiliation: Battelle - Pacific Northwest Laboratory

II. OBJECTIVE

The displacement damage produced in Materials Research Corporation Marz grade nickel and niobium and reactor grade 316 SS by 16 MeV protons and (D,T) and (D,Be) neutrons is being correlated on the basis of cluster size and density and yield strength. The effects of steady state and cyclic flux, temperature and stress on the microstructure and flow stress are being studied. The relationship between the radiation induced microstructure and flow properties is also being studied. Irradiation damage studies of path B and C alloys are planned.

III. RELEVANT DAFS PROGRAM PLAN TASK/SUBTASK

SUBTASK II.C.5 Effects of Cycling on Microstructure
SUBTASK II.C.11 Effects of Cascades and Flux on Flow
SUBTASK II.C.12 Effects of Cycling on Flow and Fracture

IV. SUMMARY

The microstructure and yield strength increase of 16 MeV proton and T(d,n) neutron irradiated nickel and niobium have been compared over the fluence range of 10^{16} cm^{-2} to 10^{17} cm^{-2}. These irradiations were performed on material taken from the same source, with the same geometry, given identical heat treatments, prepared and evaluated by the same techniques, and irradiated at 20-30°C at a flux of 10^{12} particles/cm^2-s.

The damage induced in nickel and niobium at 20°C by 16 MeV protons was found to exhibit many similarities to that induced by 14 MeV neutrons.

In nickel, the similarities include: 1) equal defect cluster diameters; 2) equal defect cluster densities at 10^{17} particles/cm^2; 3) a saturation in the cluster density of proton and neutron irradiated nickel on a damage energy basis and 4) a close, but not exact, correlation in the yield stress increase on a particle fluence basis. In niobium, the similarities include: 1) the magnitude of the lower yield stress increase and 2) the fluence dependence of the flow stress increase.

V. ACCOMPLISHMENTS AND STATUS

The yield strength increase induced in nickel and niobium by 16 MeV protons and 14 MeV neutrons was reported in the last Damage Analysis and Fundamental Studies Interlaboratory Progress Report. The microstructure of 16 MeV proton and 14 MeV neutron irradiated nickel and to a lesser extent niobium is the subject of the present report.

Typical microstructures of nickel irradiated with 14 MeV neutrons and 16 MeV protons to various fluence levels are shown in Fig. 1. In all cases, the damage consisted of small (< 8 nm diameter) clusters. No attempt was made to identify the nature of the clusters but based on the results of others [1, 2, 3, 4] they are assumed to be a mixture of interstitial and vacancy clusters. Examination of Fig. 1 indicates that the defect density increases with fluence and that at low fluence levels 16 MeV protons produce more visible damage than 14 MeV neutrons. In fact, 6×10^{16} n/cm^2 appears to be near the minimum fluence for observing defects whereas considerable damage is observed at 3×10^{16} p/cm^2.

The size and density of the defect clusters in 16 MeV proton and 14 MeV neutron irradiated nickel are summarized in Table 1. Within the estimated experimental uncertainty of $\pm$ 1 nm, there are no differences in the mean cluster diameters, while the cluster den-

sities do differ with an apparent dependence on both the irradiating particle and the particle fluence. This is shown in Fig. 2 where the cluster size and density are plotted as a function of the particle fluence.

Table I. *A* summary *of* the defect cluster data from irradiated nickel.

Irradiating Particle	Fluence (cm^{-2})	Mean Cluster Diameter (nm)	Cluster Density (m^{-3})
neutron	$6x10^{16}$	4.6	$5x10^{20}$
neutron	$1x10^{17}$	3.4	$2x10^{22}$
neutron	$2x10^{17}$	3.8	$1x10^{22}$
proton	$3x10^{16}$	3.5	$7x10^{21}$
proton	$9x10^{16}$	4.4	$2x10^{22}$

There is insufficient data to uniquely establish the fluence dependence of the cluster density, however the data in Fig. 2 suggests that the cluster density in neutron irradiated nickel may saturate at about $1x10^{17}$ n/cm2 and that there are no significant differences in the cluster size or density at this fluence level in proton and neutron irradiated nickel. The mean cluster diameters approach the practical resolution limit of the electron microscope and thus differences in the small defect clusters, < 3 nm, may not have been detected in the present study.

The defect size and density of proton and neutron irradiated nickel are very comparable on a damage energy basis, as shown in Fig. 3, where a saturation in the cluster density above 0.02 eV/atom is apparent for both particles.

The microstructure of a niobium specimen irradiated with 14 MeV neutrons to $1x10^{17}$ n/cm^2 consisted of a fairly uniform distribution of small defect clusters. The quality of the foil was not good enough for quantitative analysis; however, the mean cluster size and density are estimated to be $\sim$ 4 nm and $1x10^{22}$ m^{-3}, respectively. These results are comparable to those reported by J. Narayan et al. [5] for Be(d,n) neutron irradiated high purity, single crystal niobium. They reported that their dislocation loops were 2/3 interstitial and 1/3 vacancy type.

Niobium TEM foils were not irradiated with protons at the same time as the nickel foils and the tensile specimens and thus direct comparisons of the microstructures produced by neutrons and protons are not available. However, a niobium foil was proton irradiated to a fluence of $1x10^{17}$ p/cm2 during a test of the helium cooling system and the preliminary analysis indicates that proton irradiation produces more visible damage than neutron irradiation on a per particle basis. Experiments are underway to confirm this.

VI. REFERENCES

1. Brimhall, J. L., Kissinger, H. E. and Mastel, B., Journal of Applied Physics, vol. 37, No. 8, July 1966, p. 3317.

2. Ruhle, M. R., in "Radiation Damage in Reactor Materials", vol. I, IAEA Vienna, 1969, p. 113.

3. Mitchell, J. B., Parkin, D. M., Van Konynenberg, R. A., and Echer, E. J., The Philosophical Magazine, vol. 31, 1975, p. 919.

4. Bourret, A. and Dantreppe, D., Phy. Stat. Sol., vol. 29, 1968, p. 283.

5. Narayan, J. M. and Ohr, S. M., Journal of Nuclear Materials, vol. 63, 1976, p. 454.

VII. FUTURE WORK

16 MeV proton irradiations at 10^{13} p $/cm^2$-s and 20°C to fluences of $5x10^{17}$ p $/cm^2$ and 10^{18} p $/cm^2$ have been completed. Evaluation of these specimens along with Ni, 316 SS and Nb specimens irradiated with Be(d,n) neutrons to $1x10^{17}$ n/cm^2 and $5x10^{17}$ n/cm^2 at 20°C and with T(d,N) neutrons to $6x10^{16}$ n/cm^2 at 175°C are planned. 16 MeV proton irradiations at 175°C are planned.

VIII. PUBLICATIONS

1. R. H. Jones, D. L. Styris and E. R. Bradley, "Radiation Damage Effects in 16 MeV Proton and 14 MeV Neutron Irradiated Nickel and Niobium", 9th International Symposium on Effects of Radiation on Structural Materials, July 11th - 13th, 1978, Richland, WA.

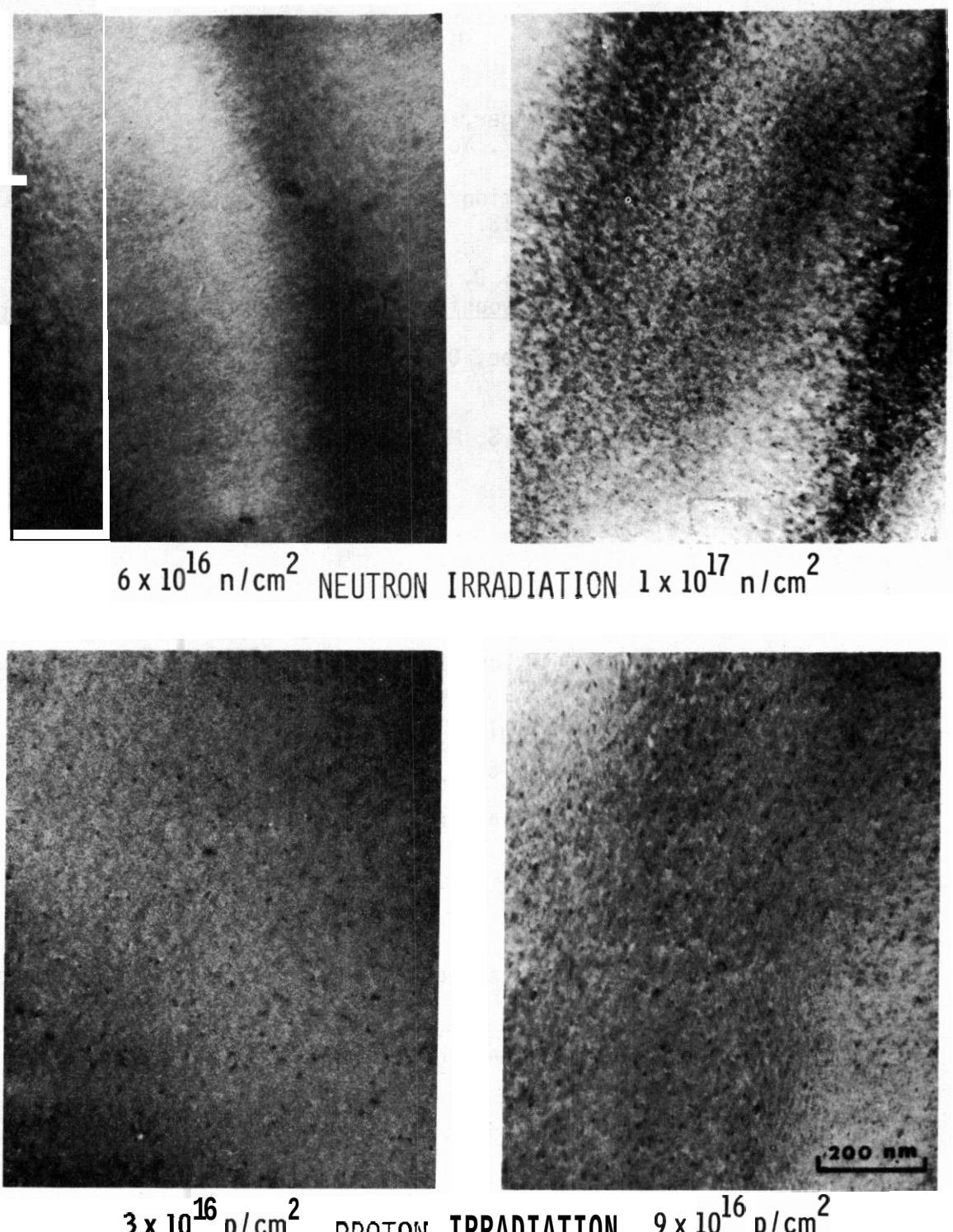

FIGURE 1. **Typical microstructures** of **neutron and proton irradiated nickel.**

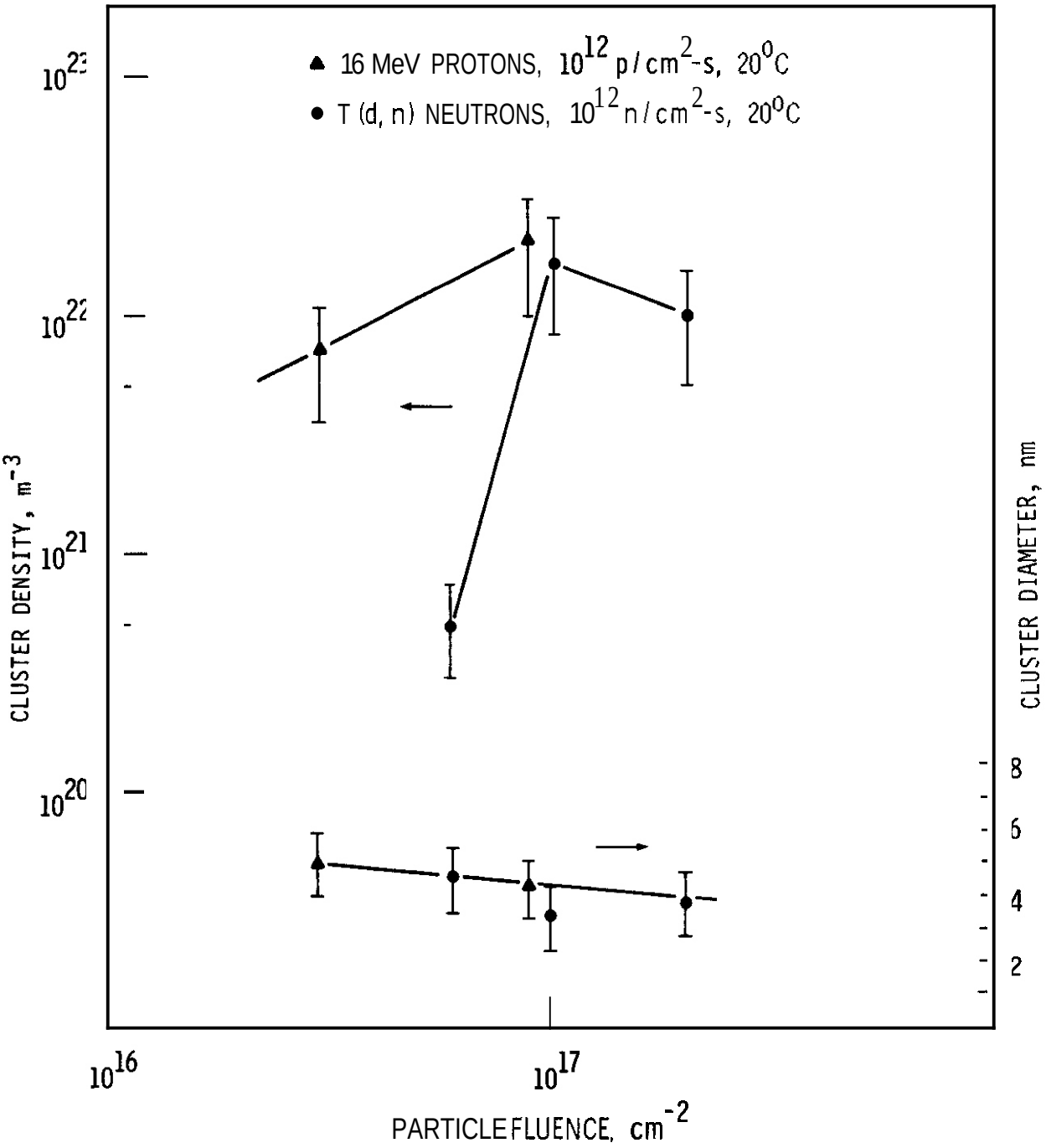

FIGURE 2. Comparison of the size and density of defect clusters in neutron and proton irradiated nickel as a function of particle fluence.

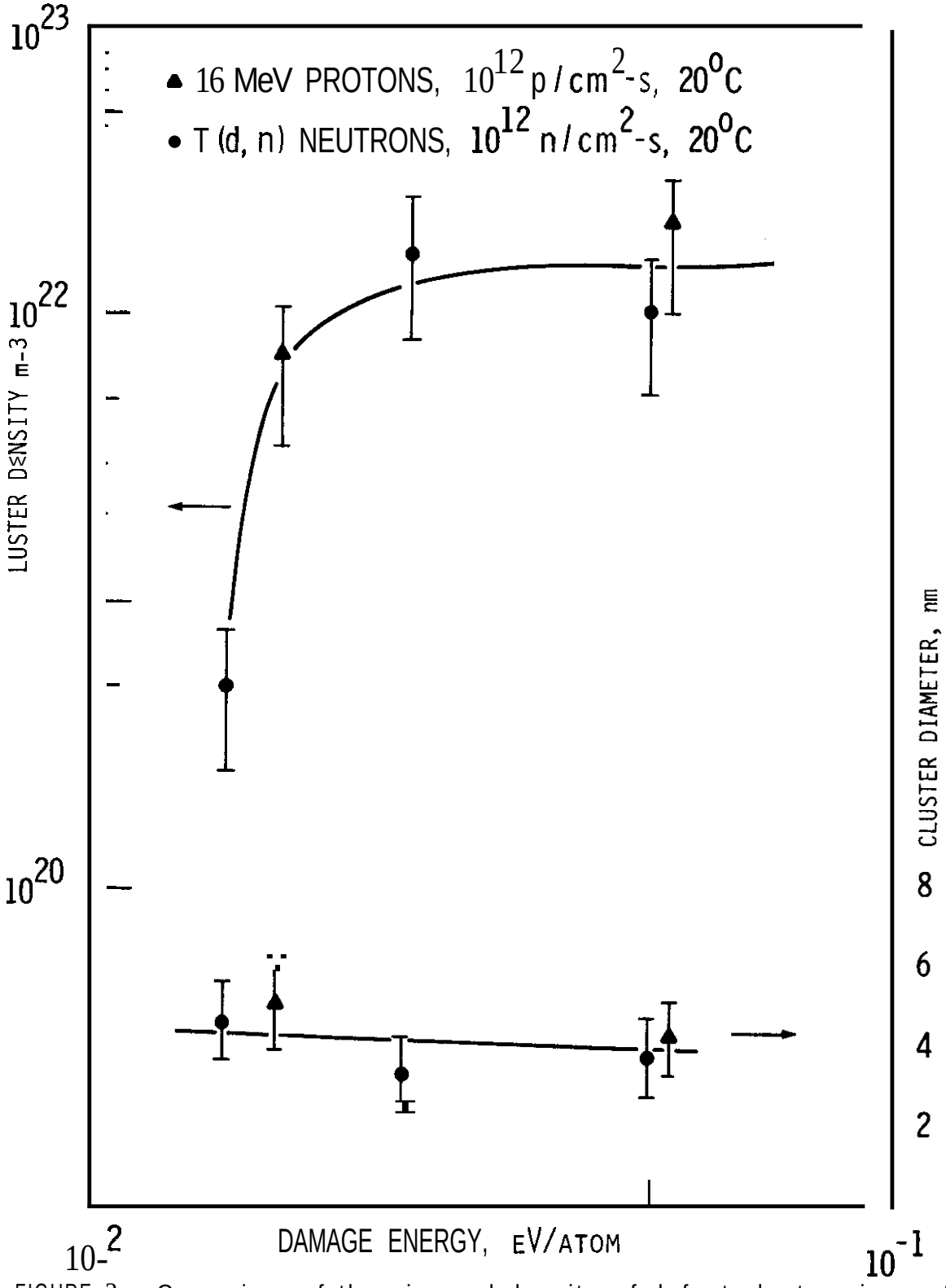

FIGURE 3. Comparison of the size and density of defect clusters in neutron and proton irradiated nickel as a function of damage energy per atom.

I. PROGRAM

Title: Effects of Near Surface Damage and Helium on the Performance of the First Wall

Principle Investigator: Θ. K. Harling

Affiliation: Nuclear Reactor Laboratory, Massachusetts Institute of Technology

II OBJECTIVE

The objective of this study is to understand and quantify the effects of near surface damage and implanted gas on the performance of the fusion reactor first wall.

III. RELEVANT DAFS PROGRAM TASK/SUBTASK

TASK II.C.5 Effects of Cycling on Microstructure

II.C.12 Effects of Cycling on Flow and Fracture

II.C.13 Effects of Helium and Displacements on Crack Initiation and Propogation

II.C.15 Effects of Near Surface Damage on Fatigue

IV. SUMMARY

An analysis has been carried out to obtain a semi-quantitative picture of the state of the surface/near surface region of the first wall in a Tokamak type FR. The charge state of particles incident upon the first wall was determined to be of major importance in assessing the resulting effects. This important result has not generally been appreciated previously. Using the results for the expected state of the near surface region of the first wall, a scoping experiment has been designed to determine the effect of near surface damage and implanted helium upon the performance of the first wall. Fatigue cracking will be studied in an environment which closely simulates the time dependent stresses and

the radiations expected at the first wall of a FR.

V. ACCOMPLISHMENTS AND STATUS

A. Near Surface Displacement Damage and Implanted Gas - H. Andresen (M. I. T./Hahn Meitner Inst.) and O. K. Harling (M. I. T.)

1. Introduction

The near surface region of the plasma vessel or first wall of FR's will probably be subjected to unusually high damage and gas implantation rates due to the ions which will leak from the plasma. The effect of a highly damaged and implanted layer on the performance of the first wall is not currently understood. That there is a significant potential problem can be deduced from the following considerations.

Assuming a (d,t) burning tokamak with neutron wall loading in the one Mw/m^2 range, with reasonable values for the machine parameters, the particle fluxes incident upon the first wall are approximately $\phi_{D,T} = 10^{15} - 10^{16}$ /cm^2 - sec, $\phi_n \sim 4 \times 10^{13}$ /cm^2 - sec and $\phi_{He} \sim 4 \times 10^{13}$ /cm^2 - sec. The hydrogen species will probably reach the wall as neutrals with a broad angular and energy distribution, the neutrons will, of course, reach the wall with 14.1 MeV and penetrate deeply into the first wall and blanket producing damage and transmutations. The helium particle flux will consist principally of low energy thermalized He particles whose charge and angular distribution is uncertain. A small fraction <1% of the alpha particles will reach the wall with high energies and these will be charged. If a divertor is used the hydrogen and high energy helium fluxes to the wall may not be drastically different.(1) There is some indication that the main effect of a divertor may be to prevent atoms of wall material from entering into and poisoning the plasma.

The concentration of helium and dpa which builds up in the near surface region of the first wall will depend upon the energy and

angle of the incident helium particles as well as upon first wall sputtering and redeposition rates. These effects cannot be adequately predicted at this time to determine unambiguously the situation which can be expected for the near surface of future FR's. A scenario based upon reasonable estimates indicates that there could be a high concentration of He and lattice damage in the first few microns. High concentrations of He in the range of 0.1 - 0.3 He atoms/wall atom and damage in the tens of dpa range might be reached in the near surface within about 100 days of reactor operation provided net erosion due to sputtering can be kept sufficiently small. Redeposition which has been observed in current experiments may greatly reduce the net removal of wall material expected on the basis of sputtering alone.

As a result of the near surface displacement damage and gas implantation, the expected fast neutron induced bulk damage and helium production and the cyclic stresses which will be applied to the structure by thermal cycling resulting from the intermittent power cycle, the following phenomena are considered possible. Considerable helium precipitation will occur, even at low temperature, producing mainly bubble hardening. The swelling of the near surface layer, due to implanted He, could readily occur only outward from the surface. This could produce compressive stresses in the surface layer. The subsurface layer will then be in a state of tension gradually decreasing in magnitude into the bulk to equilibrate the compressive stress in the near surface layer. This stress plus the cyclic stresses resulting from the temperature gradients of the normal FR power cycle could provide the driving force for crack propogation from the near surface region into and ultimately through the bulk.

A better understanding of the effect of the near surface region of the first wall upon the overall performance of this structure is a necessary prerequisite for FR design. In the present project we have begun to examine this problem. We report here the results of some of our initial analyses of the first wall environment. Also we report

the design of a fatigue cracking scoping experiment which simulates much of the relevant environment which is expected at the first wall of a FR.

2. The Near Surface Region of a CTR First Wall

A literature analysis was performed in order to obtain a semi-quantitative picture concerning the state of the first wall surface in a Tokamak type fusion reactor. Starting point was the assumption that the near surface layer will be stressed and embrittled by the impinging plasma particles while the underlying material will be embrittled by fast neutron induced displacements and helium production via (n,α) reactions and that this in combination with large temperature cycling, expected for pulsed mode reactors, might lead to crack initiation and propagation. The main points which had to be studied were judged to be (1) thickness, roughness and stress state of the affected near surface layer, and (2) temperature gradient across the first wall and thermal cycling.

Experimental evidence from different authors indicates that the result of continued bombardment of a material with helium is a porous layer in dynamic equilibrium with the bombarding species, blistering being only a possible initial process. (See e.g. [2]) The influence of such a layer on the underlying material can only be important, if considerable stresses are maintained and additionally, if the layer were sufficiently thick. The thickness of the affected layer is influenced mainly by the following parameters: 1. Energy and angular distributions of the helium particles; 2. Sputtering; 3. Redeposition. The rates of the helium implantation are only of secondary importance because this merely concerns the time until equilibrium is attained. While energy distribution and sputtering are covered by a large amount of literature, the angular distribution and the redeposition have generally been neglected. However, in a reactor with magnetic confinement the angular distribution is extremely different for ions and neutrals. While neutrals will have a broad angular distribution around the surface normal, this distribution will be sharply peaked near glancing incidence for charged particles.

From a survey of the relevant literature we have concluded that at almost glancing incidence the interaction phenomena change drastically compared to normal incidence. For example, Oen and Robinson calculated very large energy and particle reflection coefficients approaching 1 at angles above 80° for hydrogen and helium particles in the energy range 0.1 - 5 KeV.[3] Also the sputtering efficiency of particles increases with increasing angle. Computer simulations of Hoffman et al,[4] in very good agreement with measurements of Bohdansky, Bay and Roth[5] show that for incidence angles above 80° the sputtering is enhanced by factors of 6 for 1 KeV protons and up to a factor of 14 for 8 KeV protons. Blistering from glancing incidence helium bombardment at energies below 20 KeV is not expected to occur because of high reflection probabilities, high sputtering efficiencies and the small penetration depths of these particles. For high energy α's the prediction is more difficult, especially because blistering will depend sensitively on the actual peak in the angular distribution.

Particles with glancing incidence are preferentially reflected in the specular direction,[3,6] at energies below 10 KeV preferentially as neutrals.[7] Consequently they impinge on the surface several times before they are slowed down or undergo a big angle scattering event. The sputtering due to low energy helium then has to be multiplied by the average number of reflections of these particles. Thus the sputtering due to helium might well exceed hydrogen sputtering even if the flux from the plasma is more than an order of magnitude lower than that of hydrogen species. The angular distribution of the high energy α's escaping from the plasma has recently been calculated by different authors[8,9,10]. Bauer et al[10] calculated the distribution of these particles in stainless steel surfaces to be broad and extending to a depth of about 3 microns. We judge that this is the layer which should be considered for probable mechanical effects, because major stresses and severe embrittlement will develop there.

Stress cycling due to the normal power cycle of a Tokamak

power reactor is an important part of the stress environment at the surface of the first wall. The biggest temperature cycles are calculated for helium cooled reactors, where the first wall may be cycled between 300 and 550°C.[11] With lithium or water coolant smaller changes in the wall temperature are expected. In addition to this "routine-cycling" several authors have considered cycling due to accidental plasma breakdowns. Such control problems would result in even larger stresses and strain rates. The stresses which result from the temperature gradient across the first wall seem unavoidable. A reasonable rough number for the temperature difference, AT, of a liquid cooled reactor seems to be 30 - 50°C across a wall of 5 mm thickness (stainless steel), while a AT up to 100°C has been reported for a helium cooled reactor design.[11] The stresses in the thermal membrane have been analyzed by different authors and Liu has considered the connection with cyclic creep fatigue for a special design.[12] By analyzing the thermal bending stresses he identified the strain range during a full normal operating cycle to be 0.2 - 0.3%.

3. In-Reactor Fatigue Crack Propagation Experiment

The problem analysis showed that an influence of the surface on crack initiation and propagation is most probable from the high energy α's, less so from the wall bombardment by hydrogenic and helium particles with energies corresponding to the temperature of the plasma edge. In an experiment designed to simulate the influence of the surface on failure the two following conditions were judged to be the most important: 1) Surface bombardment by high energy a's to a depth of several microns at an appropriate rate; and, 2) Temperature and stress-cycling of the a-irradiated samples in simulation of the cycling expected for later fusion reactors. These conditions can be met using pressurized cylindrical capsules in the scoping experiment briefly described below.

The experiment will be carried out by irradiating a fatigue crack specimen in an existing irradiation facility in the core of the MIT research reactor. This specimen or specimens will be simultan-

eously irradiated by fast neutrons ($10^{14}/cm^2$ - sec) which will produce displacement damage and by high energy helium ions which will damage and implant the surfaces of the specimen. Slow neutrons impinging upon a ^{10}B coated foil surrounding the sample will produce the helium ion bombardment which simulates the high energy alpha bombardment expected at the first wall of a fusion reactor. Slow neutrons will also produce the helium in the bulk of the fatigue crack specimen by the double capture reaction on nickel and by the (n,α) reaction on boron dissolved in the stainless steel or high nickel alloy sample. Stress cycling will be accomplished by cycling the temperature and therefore the pressure of the helium gas which is sealed inside the hollow sample. A thin walled, variable wall thickness tube will probably be used for the fatigue crack sample. We have estimated that the stress in the sample can be varied in magnitude and in time in a manner which closely approximates the expected stress-time cycles in a fusion reactor. The test would continue until a fatigue crack results in a release of some of the pressurized helium within the hollow sample. Detection of a penetrating crack will probably be done by measuring the presence of a radioactive tracer gas, Ar or Xe, which will be incorporated into the He gas which is used to pressurize the interior of the specimen. It is intended to remove the samples at regular time intervals from the reactor for characterization of the surface by optical microscopy and a replica technique. Careful examination of the failed sample would be carried out with optical and electron microscopy to characterize the fatigue cracks in different parts (different stress Levels due to specimen design) of the fatigue crack samples. We would also examine the relevance and possibility of carrying out post irradiation mechanical property tests.

VI. REFERENCES

1. R. Behrisch, Critical Materials Problems in Energy Production, Academic Press, New York, San Francisco, London (1976):92-135

2. K. L. Wilson, L. G. Haggmark, R. A. Langley, Proc. Int. Symp. on Plasma Wall Interactions, Julich (1976) Pergamon Press, Oxford

(1977):401

3. O. S. Oen and M. T. Robinson, Nucl. Instr. Meth. 132 (1976): 647

4. T. J. Hoffman, H. C. Dodds, Jr., M. T. Robinson and D. K. Holmes *ANS* Winter Meeting, Nov. 29, 1977

5. J. Bohdansky, H. L. Bay and J. Roth, Proc. 7th Int. Vac. Congr. and 3rd Int. Conf. Solid Surfaces, 1977, Vienna

6. A. D. Marwick, M. W. Thompson, B. W. Farmery, and G. S. Harbinson, Rad. Effects 15 (1972):195

7. P. Meischner and H. Verbeek, J. Nucl. Mat. 53 (1974):276

8. V. S. Belikov, Ya. 1. Koleschenko and V. A. Yavorski, Sov. J. Plasma Phys. 3 (1977):104

9. G. H. Miley and L. M. Hively, 3rd Int. Conference on Plasma Surface Interactions in Controlled Fusion Devices, UKAEA Culham Lab., 3-7 April 1978

10. W. Bauer, K. C. Wilson, C. L. Bisson, L. G. Haggmark and R. J. Goldston, Sand J. J.-8757

11. D. W. Kearney, D. W. Culver, J. A. Dalessandro, S. N. Rosenwasser D. L. Vrable and C. Wong, Proc. 7th Symp. on Eng. Problems of Fusion Research, Knoxville, Tenn., Oct. 1977, p.1483

12. K. C. Liu, Proc. 7th Symp. on Eng. Problems of Fusion Research, Knoxville, Tenn., Oct. 1977, p. 1495

VII FUTURE WORK

Detailed design of an in-reactor fatigue cracking experiment will be completed, the experimental equipment for this test will be constructed and the experiment initiated.

I. PROGRAM

Title: The Depth Dependent Damage Profile in Nickel Irradiated with Nickel or Copper Ions

Principal Investigator: G.L. Kulcinski and P. Wilkes

Affiliation: University of Wisconsin

II. OBJECTIVE

To develop a fundamental understanding of the formation of voids, loops and precipitates in heavy ion and electron irradiated metals and alloys.

III. RELEVANT DAFS PROGRAM PLAN TASK/SUBTASK

II.C.6. Effects of Damage Rate and Cascade Structure on Microstructure.

IV. SUMMARY

High purity nickel samples have been irradiated with high energy (>14 MeV) heavy ions and the resultant microstructure examined in cross section (i.e., in a plane parallel to the incident ions). The material in the region near the ion end-of-range was found to swell less than the mid-range in both self-ion and copper ion irradiated samples. A 100 nm void denuded zone was observed at the front surface in samples irradiated at 525°C. and voids were observed at depths ≈15% greater than the calculated damage curves. There was no significant difference between copper and nickel irradiations. An irradiation at 200°C produced a loop lattice structure aligned along {001} with a spacing of ≈40 nm.

The steady-state rate equations were formulated and solved to give the depth dependent defect concentrations. The calculated void growth

rate was found to qualitatively fit the experimental results. A depth dependent radiation enhanced diffusion model predicted the result that for ion fluences used in this study, the injected copper impurities were confined to the end-of-range region.

V. ACCOMPLISHMENTS AND STATUS

J. B. Whitley, G. L. Kulcinski, P. Wilkes, H. V. Smith, Jr.
(University of Wisconsin-Madison, Madison, WI)

1. Introduction

In the past several years, simulation studies have become a useful tool in the study of the swelling behavior expected from high fluence, high temperature neutron irradiation metals.[1,2] Comparison of the final damage microstructure produced by heavy-ions to that in a neutron irradiated sample is clouded by several unique aspects of the former such as surface effects or effects due to the limited volume of material irradiated.[3] In addition, an accurate theoretical description of the damage process at the high displacement rates typical of simulation studies has proven to be elusive.[4] Without a proper description of the effect of dose rate on the swelling response of a material, the usefulness of high displacement-rate simulation studies as an indicator of material response to neutron irradiation will be greatly reduced.

To expand our understanding of the radiation damage process caused by heavy-ions, this experiment used a sample preparation technique which allowed the direct cross sectional viewing of the microstructure along the ion path.[5] This powerful technique, which is a modification of the procedure first applied by Spurling and Rhodes[6] to proton irradiated stainless steel, allows a detailed study of the depth variation in the irradiated microstructure. In this study, the effects of copper and nickel ion irradiations were compared. The steady-state rate equations for defect

concentrations were solved to give their spatial profiles for comparison with the experimental damage profiles. The final concentration profile of the incident copper ions was calculated by applying an appropriate enhanced diffusion model.[7]

2. Experimental Procedure

The material used throughout this study was Marz grade nickel obtained from Materials Research Corporation and of nominal purity 99.995% (substitutional impurities only). The sample lot analysis showed impurity levels of copper less than 3 wt-ppm. After machining the samples into the proper shape for irradiation, they were given a recrystallization anneal in an inert atmosphere for one hour at 1000°C and furnace cooled. The samples were then electropolished in a solution of 60% sulfuric acid with 40% water to give the cleanest possible surfaces prior to loading into the target chamber. The samples were then irradiated in a high temperature, ultra-high vacuum target chamber using high energy copper or nickel ions (14 MeV to 19 MeV) accelerated by a tandem Van de Graaff accelerator.[8]

The theoretical damage energy deposition rate as a function of depth was calculated using the updated version of the Brice code[9] which includes energy transport by secondary ions. The displacement energy was taken as 40 eV,[10] with the nuclear energy loss rate converted to displacements (i.e., dpa) using the ASTM standard.[11] An example of the results for 14 MeV nickel ions incident on a nickel target is shown in Figure 1. The right-hand axis gives the displacement rate typical of the ion fluxes used in this experiment. The depression of the curve near the front surface is due to energy transport by the secondary ions. There is approximately a factor of ten variation in the total dose and the dose rate from the near surface region to the peak, with the peak of the displacement curve occurring at a depth of 2.1 μm. Also shown is the relative range distribution of the incident ions. The displacement damage curve for 14 MeV copper ions is very similar to Figure 1, while the curve

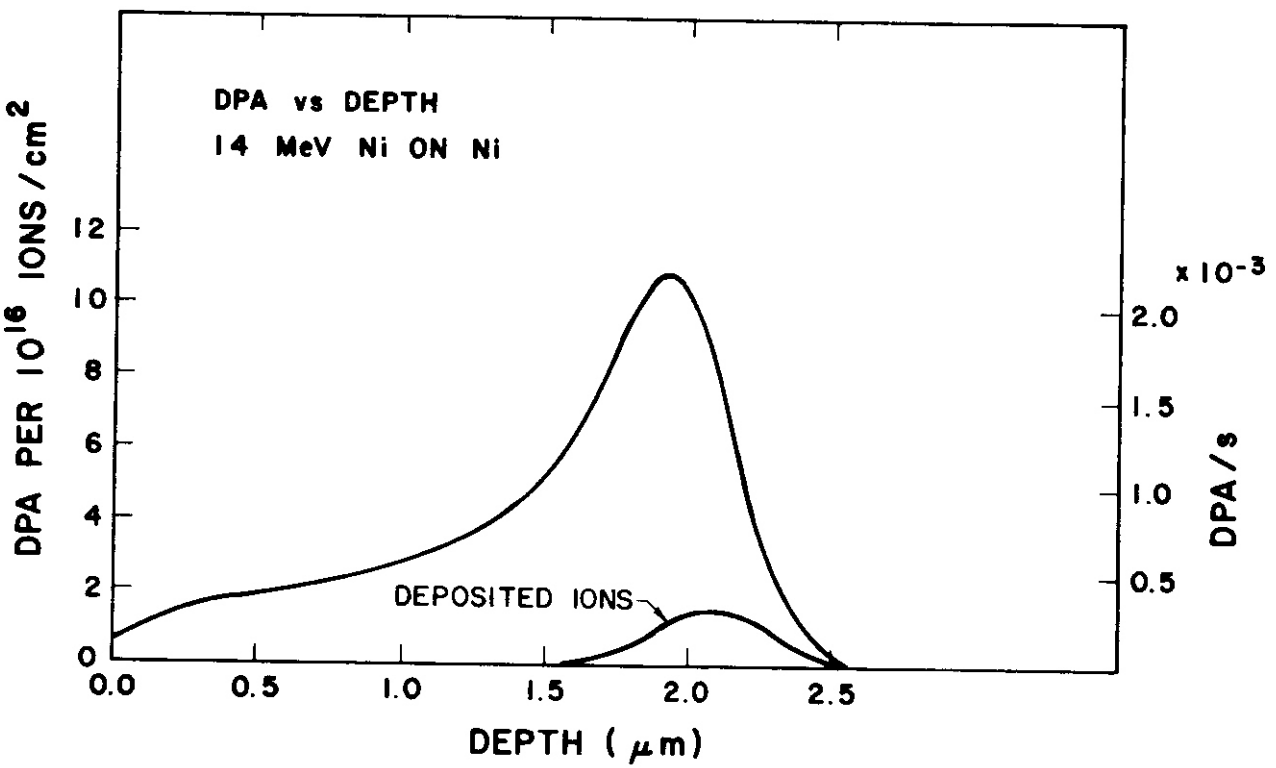

FIGURE 1. The Displacement Curve for 14 MeV Nickel Ions Incident on Nickel as Predicted by Brice[9]. The right-hand axis gives the displacement rate corresponding to the ion flux used in this experiment.

for 19 MeV copper ions has the same general shape and magnitude with the peak of the damage curve occurring at 2.5 μm.

After irradiation, the samples were prepared in cross section in a manner similar to Spurling and Rhodes[6] (Figure 2). The samples were first given an activation treatment in a solution of Wood's nickel[12] by making the sample anodic for 20 seconds at a current density of 25 mA/cm^2. This step was necessary to remove the metal oxide layer and assure a good bond. The amount of material removed by this process was estimated to be less than 0.05 μm by interference microscopy. After activation, the current was reversed in this same solution and a thin nickel strike applied. The sample was then transferred directly to a high chlorine nickel plating solution containing 150 g $NiSO_4$, 150 g $NiCl_2$ and 50 g boric acid in 1000 ml H_2O. Plating for ~24 hours in this solution at 50°C and a current density of 300 ma/cm^2 resulted in a final specimen thickness greater than 2 mm. The sample was then mounted in resin and sliced in cross section using a low speed diamond saw. Three millimeter discs were then cut from these slices and thinned for transmission electron microscopy (TEM) using a twin jet electropolishing unit. The actual region of the disc that contains the damage is rather small as is shown schematically in Figure 2. However, by careful alignment of the polishing unit at least one successful foil was usually obtained from the several slices produced from each irradiated region.

Analysis was carried out on a JEM 100B electron microscope operated at 120 KV. The depth distribution of the microstructure data was determined by dividing the micrograph into regions 0.25 μm wide parallel to the front surface. The *foil* thickness was determined using the standard stereo technique. Void size distributions were measured on a Zeiss comparator with swelling values calculated in a manner similar to Ryan.[10]

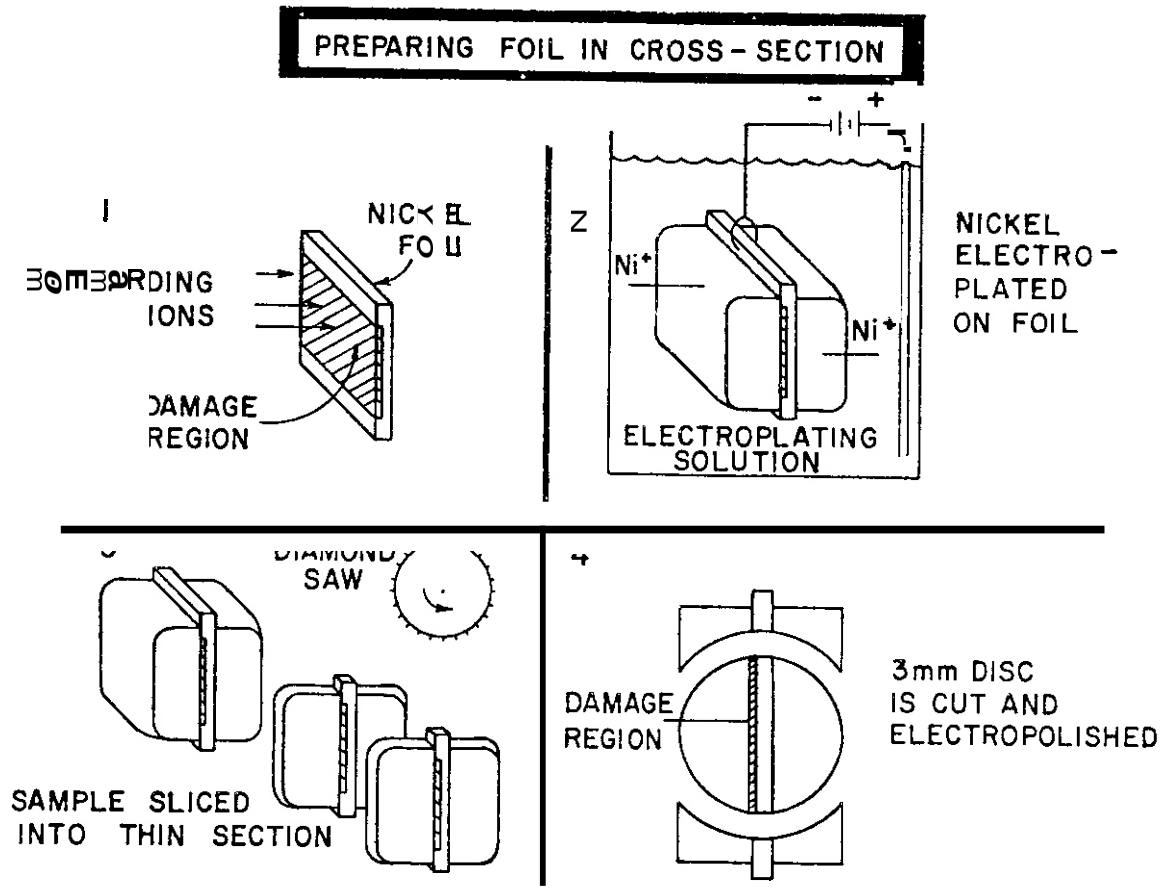

FIGURE 2 A Schematic Representation of the Cross Section Sample Preparation Procedure.

3. Experimental Results

The primary purpose of this study was a comparison of samples irradiated at 525°C to different fluence levels and using different ions. A typical micrograph obtained from a sample irradiated with 19 MeV copper ions to a fluence of 5×10^{15} ions/cm^2 and prepared in cross section is shown in Figure 3. Voids were observed to form quite readily in all samples even without prior helium injection. The original foil surface is visible at the left-hand-side of the micrograph, with the incident ions having travelled from left to right. There is a definite denuded region at the front surface with very few roids observed closer than ≈100 nm from the surface. This denuded area was followed by a region ≈150 nm wide of unusually large voids. Over the next micrometer, the void density rises while void size drops. The voids throughout the damage region were truncated octahedra with the degree of truncation increasing slightly with depth. Near the end-of-range the void density drops rapidly. In all samples, voids were observed at depths ≈15% greater than the damage range predicted by Brice.(9)

A limited dose scan with total ion fluence ranging from 3×10^{15} to 1×10^{16} ions/cm^2 was carried out at 525°C with 19 MeV copper ions. The micrographs of Figure 4 show the void microstructure development with dose. The void density in the end-of-range region is seen to increase with increasing dose, with relatively few voids seen at a depth of 3.6 μm in the low dose sample. The high dose sample, however, has a significant number in this region defining a rather sharp end-of-range. The variation from sample to sample showed the expected behavior with void size and void density increasing with dose.

Figure 5 shows the depth dependence of the void number densities determined for these samples using a 0.25 μm interval. Note that while the data would be strictly presented as a histogram, a smooth curve was drawn through the data points placed at the center of each

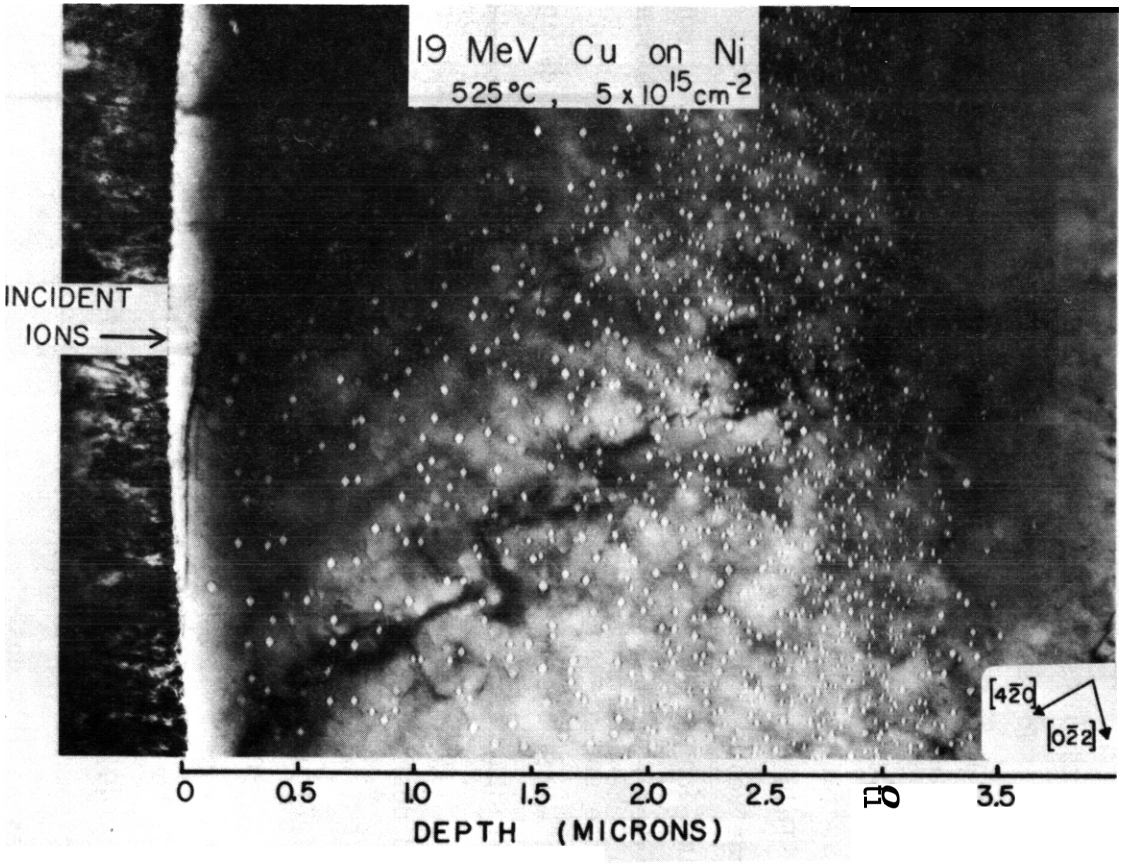

FIGURE 3. Micrograph of a Nickel Sample Irradiated at 525°C with 19 MeV Copper Ions to a Fluence of 5×10^{15} cm^{-2} and Prepared in Cross Section.

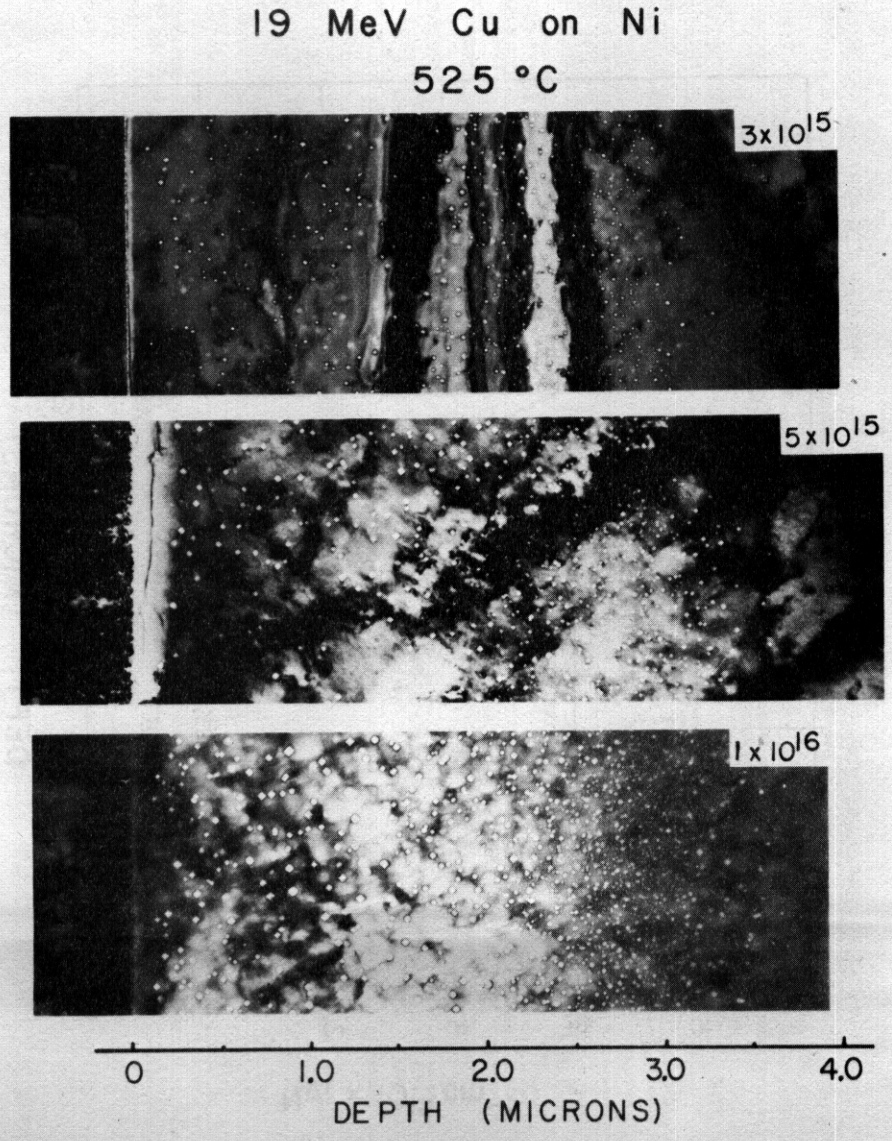

FIGURE 4. Micrographs of Nickel Samples Irradiated at 525°C with 19 MeV Copper Ions to Three Fluence Levels.

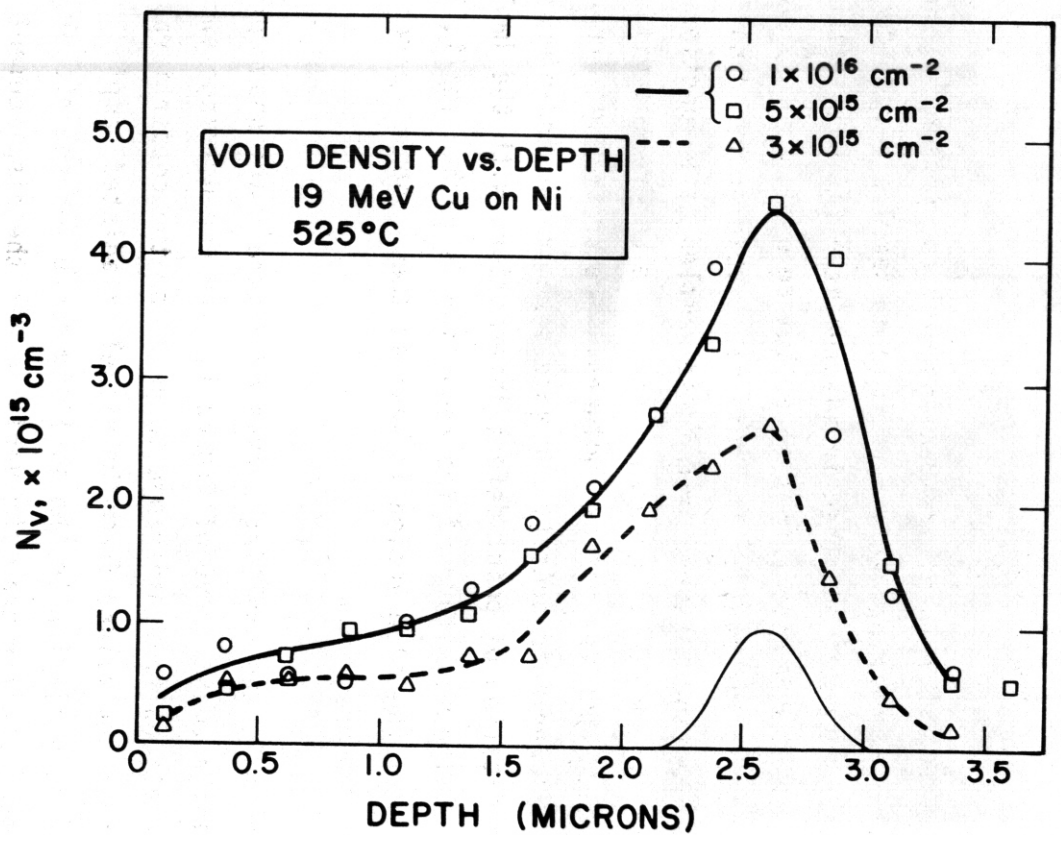

FIGURE 5 Void Density vs Depth Plots for Nickel Irradiated at 525°C to Three Fluence Levels

interval. In general, the void density curve follows the displacement curve rather closely. This result is not unexpected since the void nucleation rate is dose rate dependent. The void densities for the two high dose samples are the same within the experimental error indicating that the void density has saturated. This implies that the final void density at the end of nucleation is determined by the dose rate and not only by the total damage state.

To study the effects of irradiating with copper ions in the end-of-range region, irradiations were performed on samples given identical pre-irradiation treatments, and then irradiated at 525°C with either 14 MeV nickel ions or 14 MeV copper ions to a fluence of 1.3 x 10^{16} ions/cm^2 (i.e., ~15 dpa at the peak). The void size, void number density and the void volume fraction measured from these samples as a function of depth are shown in Figure 6. In general, there were no drastic differences observed between the two microstructures. The copper ion irradiated sample has a lower void density and void size in the end-of-range and this may be an indication of point defect interactions with the implanted copper ions. The magnitude of the reduction is rather small, however, indicating that the interaction is weak at these copper concentrations (≈2000 appm copper).

In Figure 7, the swelling curves of Figure 6 are shown plotted along with the displacement curve of Figure 1. The end-of-range swelling values and the variations' from mid-range to peak for the copper irradiated sample are lower than the values from the nickel irradiated sample. Note, however, that the variation in the swelling curve for the nickel irradiated sample is much smaller than the variation in the displacement curve in the equivalent depth range, indicating that even for self-ion,irradiations, the final swelling profile is not always directly related to the total damage level.

The dislocation structure observed in these samples consisted of dense network dislocations interacting with the voids with a few

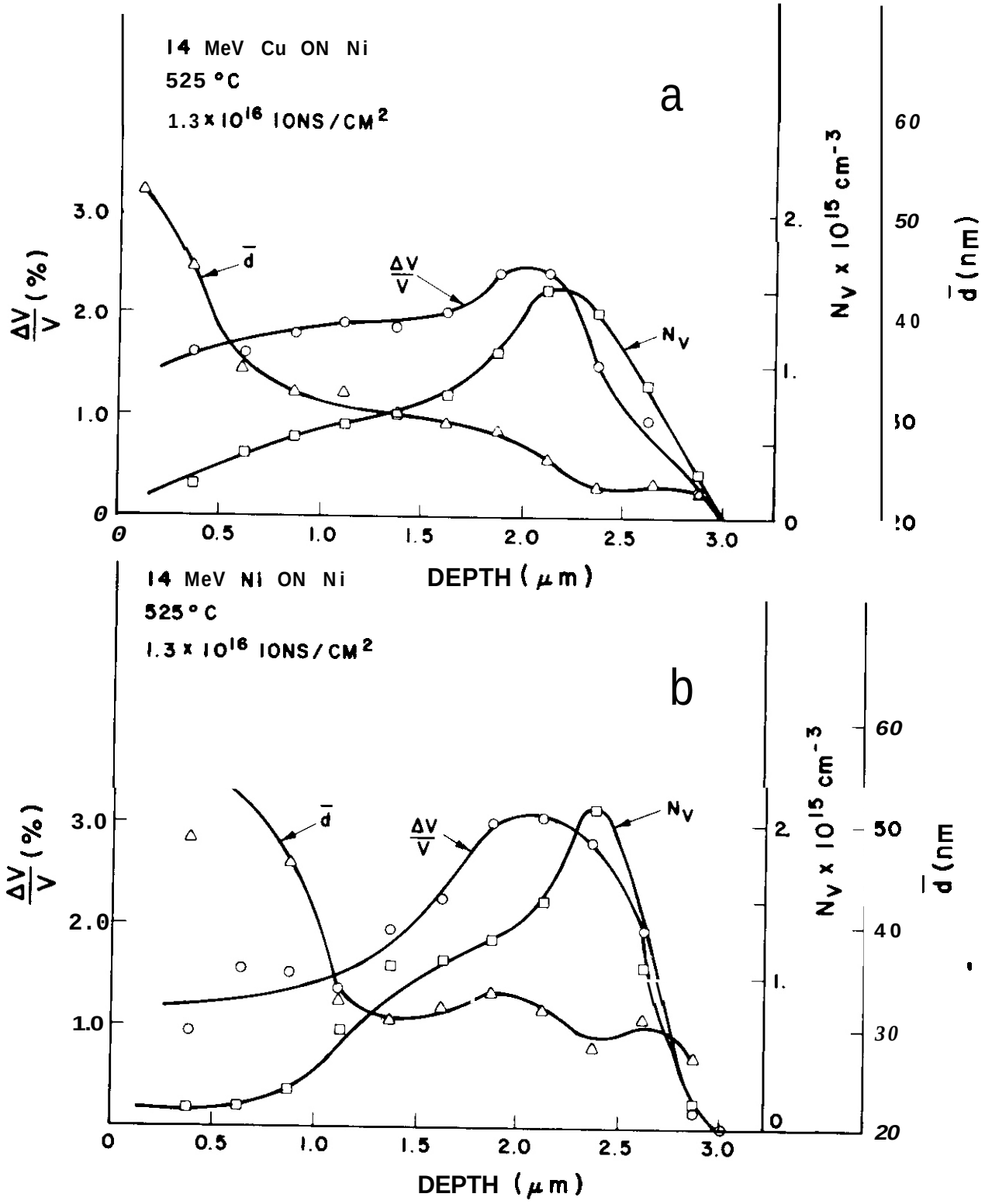

FIGURE E. Void Size, Void Density, and Void Volume as a Function of Depth in Nickel Irradiated at 525°C. a) After Irradiation with 14 MeV Copper Ions, b) After Irradiation with 14 MeV Nickel Ions. The Ion Fluence in Each Case was 1.3 x $10^{16} m^{-2}$.

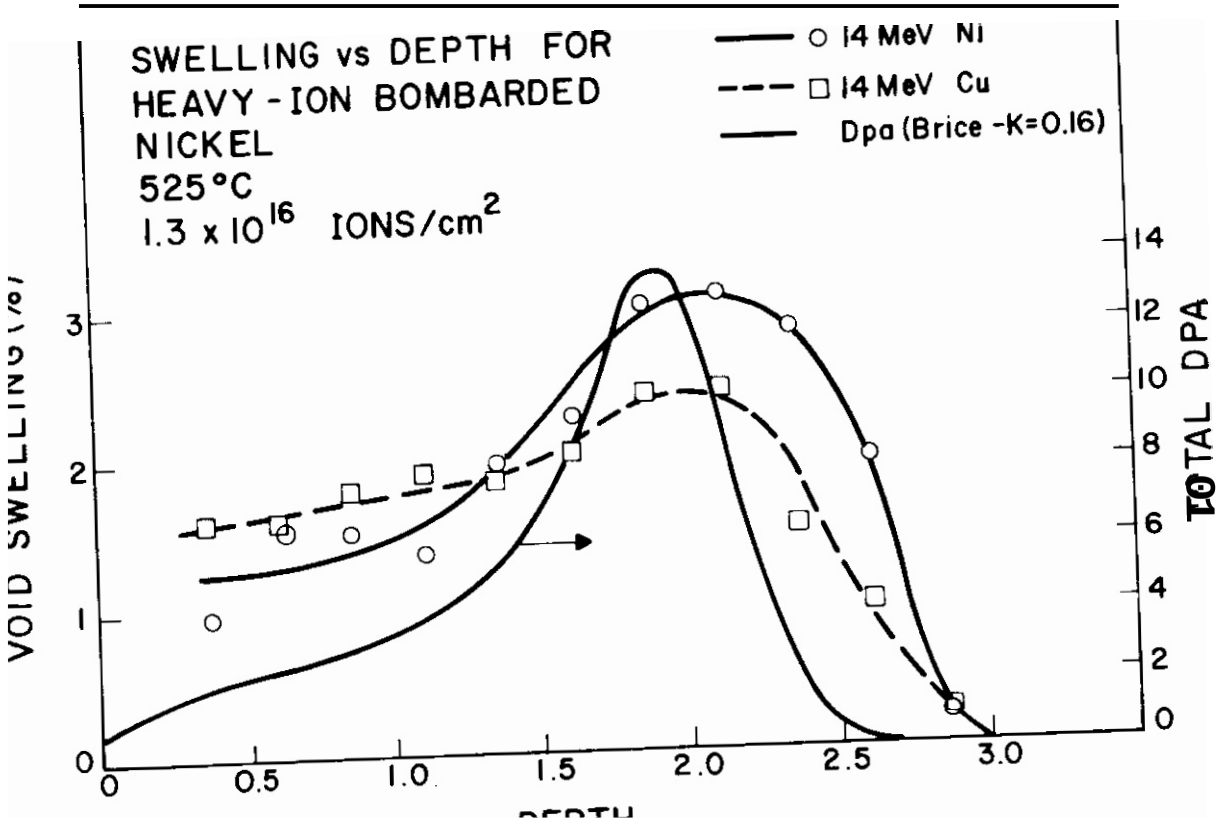

FIGURE 7. A Comparison of the Swelling Profile After Irradiation with 14 MeV Copper Ions to the Profile After Irradiation with 14 MeV Nickel Ions. The displacement curve shown is for 14 MeV nickel ions, but the 14 MeV copper ion curve would be similar.

dislocation loops scattered in the matrix. The typical dislocation structure near the end-of-range is shown in Figure 8. The total dislocation densities in these samples were about 5×10^9 cm^{-2} and did not vary strongly with depth.

An irradiation was also carried out at 200°C with 14 MeV nickel ions to study the development of the loop structure at low temperatures. A well-developed loop lattice formed along {100} directions with a spacing of ≈40 nm as is shown in Figure 9. This result is consistent with several other low temperature nickel irradiations[13,14,15] except that the lowest temperature that an aligned structure had been previously observed was 280°C. The loop structure in this study extended all the way to the foil surface without disordering. The loop lattice also extends well-beyond the area of peak damage, and can be observed at depths of 3 μm. The loop lattice spacing is approximately constant throughout the damage region and hence does not vary with the local dose rate.

4. Defect Profile Calculations

To assist in the interpretation of the experimental results, it is useful to know not only the depth profile of the defect production rate, but also the depth profiles of the vacancy and interstitial concentrations. If the ion beam is not the same chemical species as the target material, it is also important to know the final concentration profile of the incident ions and their concentration levels. The steady-state rate equations that describe the point defect concentrations are given by

$$\nabla D_i \nabla C_i + P_i - D_i C_k k_i^2 - \alpha C_i C_v = 0 \qquad (1)$$

or

$$\nabla D_v \nabla C_v + P_v - D_v C_v k_v^2 - \alpha C_i C_v = 0 \qquad (2)$$

where the subscripts i and v refer to interstitials and vacancies, respectively and the D's are diffusion coefficients, α the homogeneous

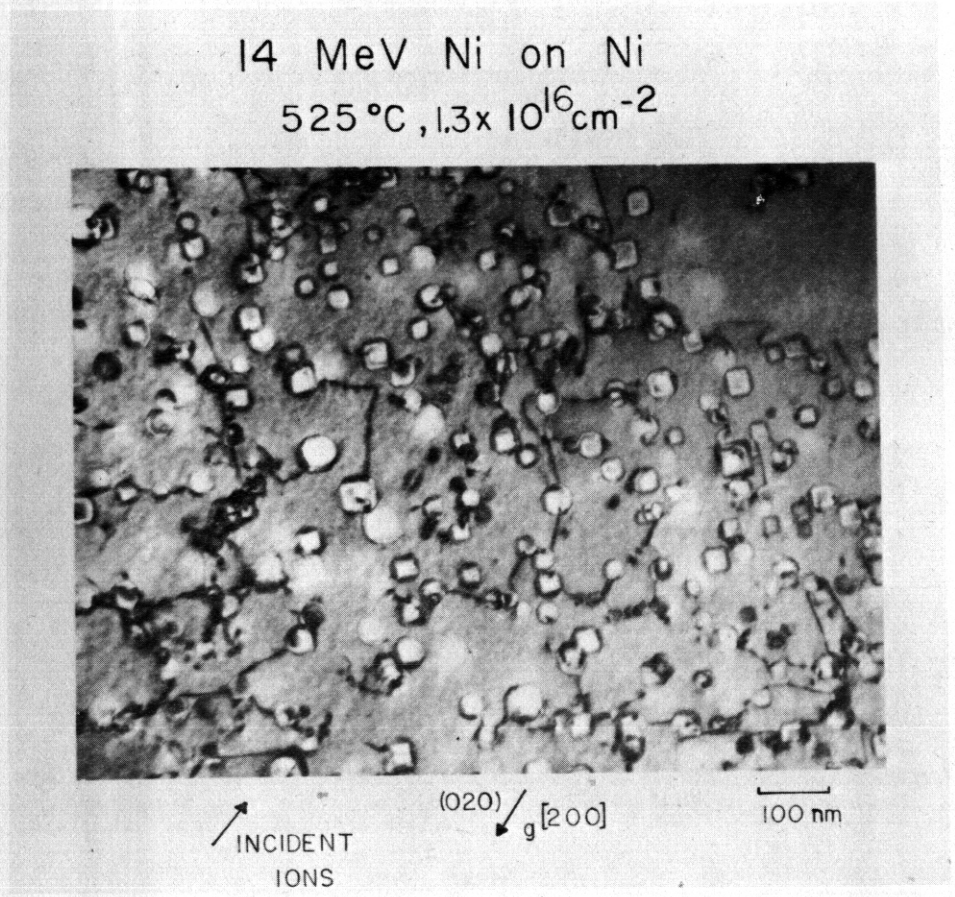

FIGURE 8. The Dislocation Structure in the End-of-Range Region of a Nickel Sample Irradiated at 525°C with 14 MeV Nickel Ions to a Fluence of 1.3 x 10^{16} cm^{-2}.

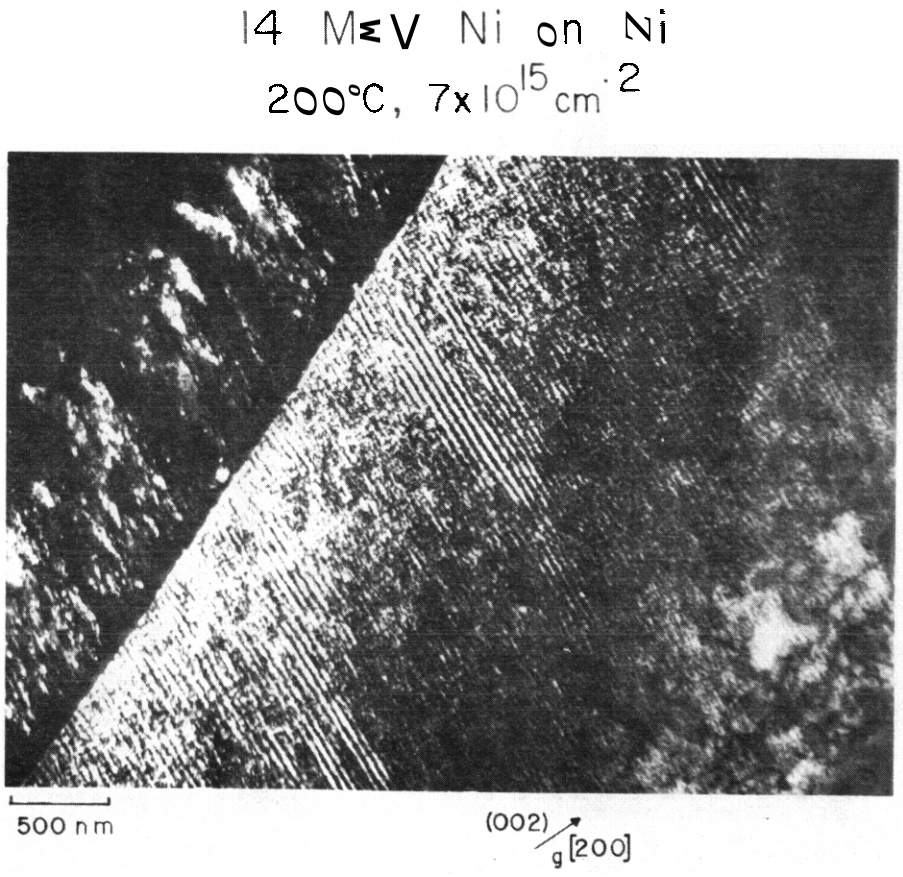

FIGURE 9. The Loop Lattice Structure Which Formed After Irradiation at 200°C with 14 MeV Nickel Ions to a Fluence of $\sim$ x 10^{15}cm^{-2}. The original foil surface is visible in the left half of the micrograph.

recombination coefficient, $\underline{P}_i$ the interstitial production rate which includes the excess interstitials produced by the incident ion coming to rest, and $\underline{P}_v$ the vacancy production rate which includes vacancy emission from sinks.[16] The $\underline{k}_v^2$ and $\underline{k}_i^2$ are the total sink density terms which will generally be depth dependent [a]

These equations were formulated in a one-dimensional manner similar to Myers, et al.,[17] and solved using a modified Gauss-Siedel iterative technique.[7] $\underline{D}_i$, $\underline{D}_v$ and α were assumed not to vary with depth or with the local defect concentration. The defect production rates were taken from the Brice code,[**]) and if voids were present in the microstructure, the ion range and energy loss rates were modified in the manner of Odette.[18] Figure 10 shows the vacancy and interstitial concentration obtained for the case of 14 MeV nickel ions incident on a nickel target Several features of the curves *of* Figure 10 are important in interpreting the depth dependent microstructure of heavy ion irradiated samples. First, the front surface is a perfect defect sink, and as such it reduces both the vacancy and interstitial concentrations in this region, altering both void nucleation and void growth rates. The width of this zone will be dependent both on temperature and sink density. The defect concentrations also show less variation in magnitude from the midrange to the peak range than does the defect production rate curve. This behavior is due to the non-linear response of the defect recombination rate which leads to a larger fraction of the defects recombining as the steady-state defect concentrations increase. This is illustrated by the curves of Figure 11, where the fractions of defects lost to sinks, recombination and by diffusion out of depth zones are shown for the curves of Figure 10. For the parameters used in this case, recombination dominates except near the front surface. Diffusion of defects beyond the production curve does give significant defect concentrations in this "undamaged" region. In this particular case the vacancy concentration at 3.0 μm was still about five orders of magnitude greater than the equilibrium value.

a. Note that cascade collapse into vacancy loops is <u>not</u> included in this formulation.

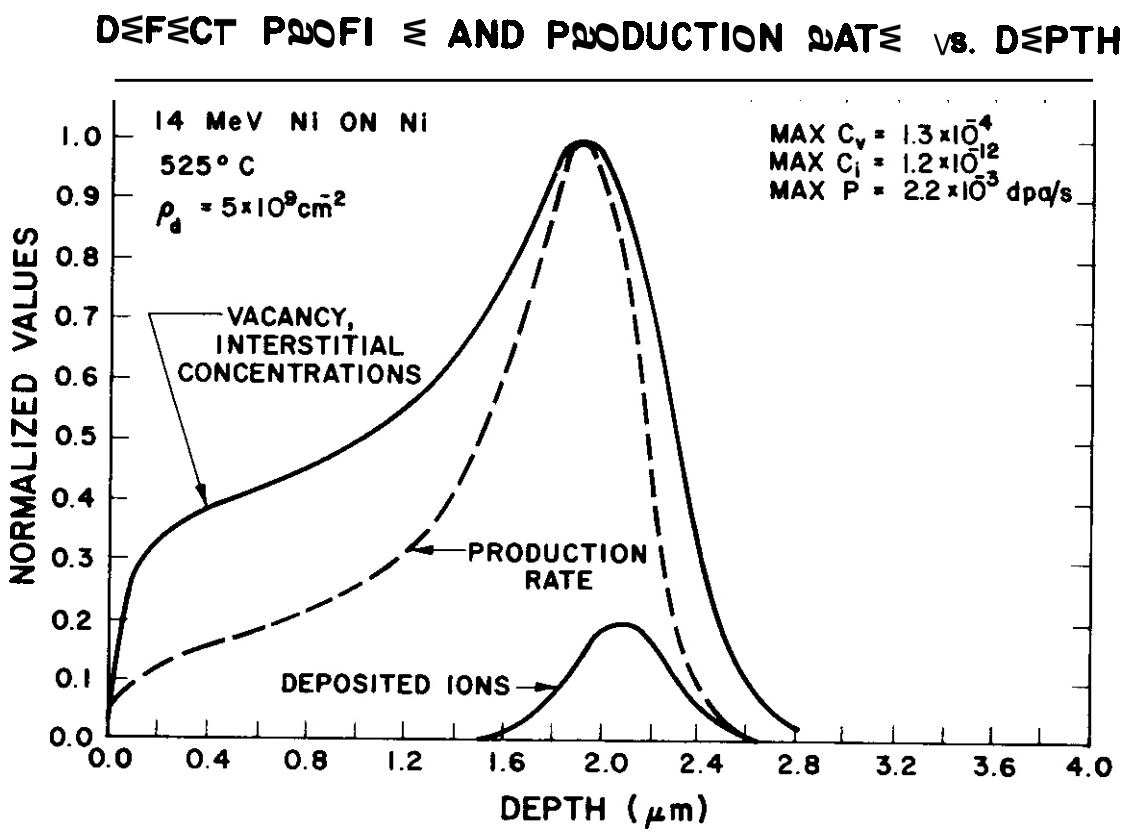

FIGURE 10 Vacancy and Interstitial Concentration Profiles for 14 MeV Nickel Ions Incident on Nickel Using the Parameters Given in Table 1. The defect production curve and the relative range distribution of the incident ions are also shown. Note that all the curves except the range curve are normalized to the peak values given in the Figure.

Table 1

INPUT PARAMETERS USED IN SOLVING EQ. 1 AND 2.
MOST MATERIAL PARAMETERS ARE FROM REF. 10

Temperature	525°C
Dislocation density	5×10^{9} cm^{-2}
Surface energy	1000 mJ/m^2 (erg/cm^2)
Vacancy migration energy	1.38 eV
Interstitial migration energy	0.15 eV
Vacancy formation pre-exponential	4.48
Interstitial formation pre-exponential	5.0
Vacancy diffusion coefficient pre-exponential	0.062 cm^2/s
Interstitial diffusion coefficient pre-exponential	0.12 cm^2/s
Vacancy formation energy	1.39 eV
Interstitial formation energy	4.08 eV
Recombination factor, α/D_i	1×10^{15} cm^{-2}
Dislocation bias	2.0%
Ion flux	2×10^{12} $ions/cm^2/s$

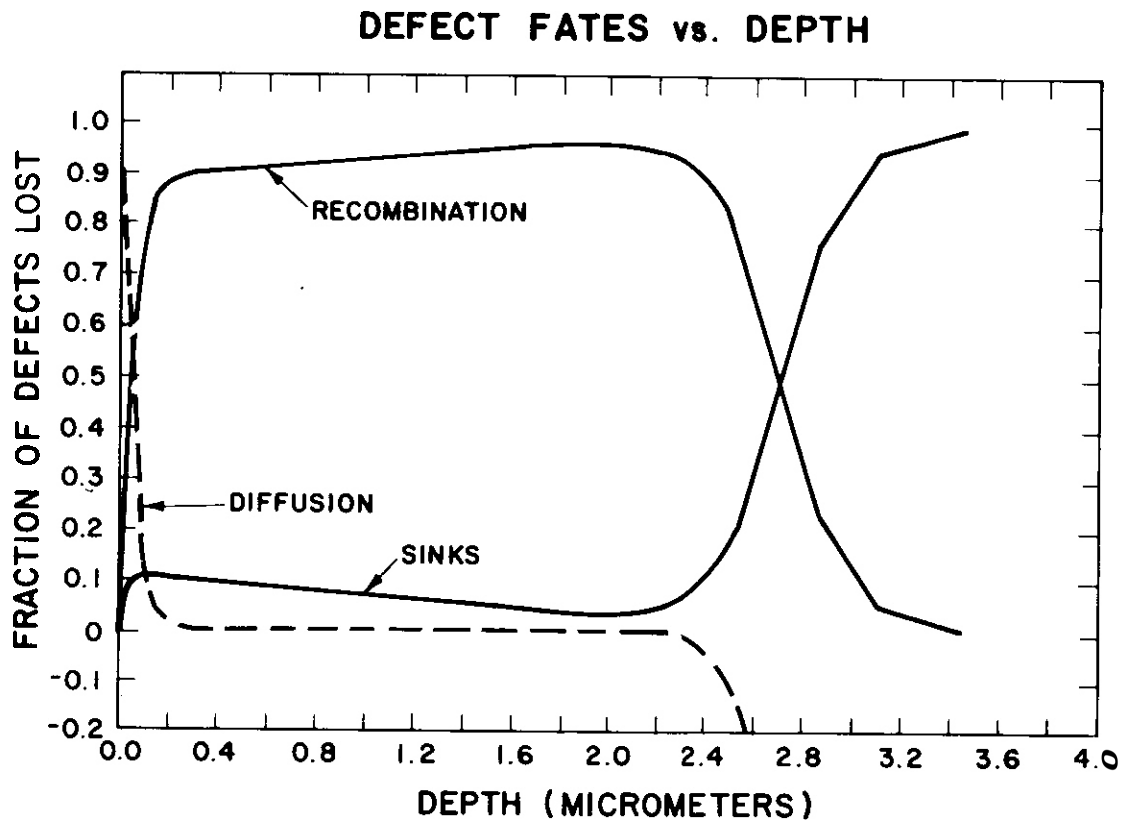

FIGURE 11. The Fractions of Defects Lost by Absorption at Sinks, by Recombination, and by Diffusing from a Depth Region. A negative diffusion fraction is obtained when a region has a net influx of defects.

In interpreting the end-of-range microstructure of the copper ion irradiated samples, it is important to know the resultant impurity distribution. The concentration of an impurity is described by

$$\frac{\partial C_A}{\partial t} = \nabla D_A \nabla C_A + S_A \qquad (3)$$

where S_A is the source term for the impurity and will be depth dependent in this case. C_A is the concentration of the impurity A in the matrix, and D_A its radiation enhanced diffusion coefficient assumed to be of the form[16]

$$D_A = \sum_K FK\ DK\ CK \qquad (4)$$

where the sun is over all mobile defects and defect clusters, and the F_K are correlation factors. Note that this model of radiation enhanced diffusion does not apply to interstitial impurities and neglects solute drag effects.

To model the ion irradiation case, the steady-state solutions for the vacancy and interstitial concentrations were found from equations 1 and 2 ana substituted into equation (4) to give the depth dependent diffusion constant (now that mobile defect clusters such as di-vacancies were ignored in this solution). This diffusion constant was then used to solve equation 3 in one-dimension. The vacancy and interstitial correlation factors were taken as 0.78 and 0.4, respectively.[19]

Results of this calculation for 14 MeV copper ions incident on nickel are shown in Figure 12. The radiation enhanced diffusion spreads the impurity predominately towards the front surface while lowering the peak of concentration. At the low ion fluence typical of this study, the range of influence of the copper is still confined to the end-of-range region (Figure 12a). Even in this case, however, the peak copper concentration exceeds 0.2 atomic percent. In the high fluence case (Figure 12b) the

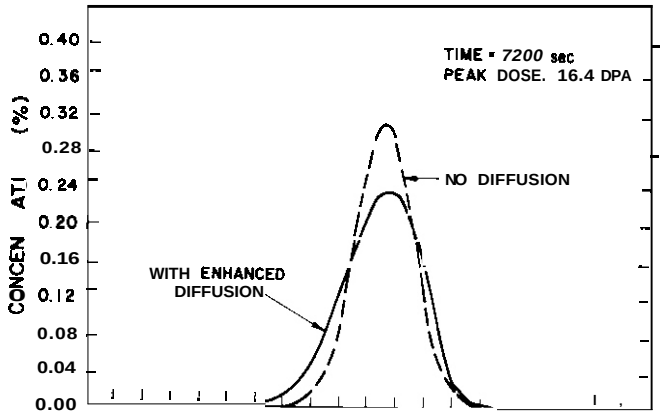

(a)

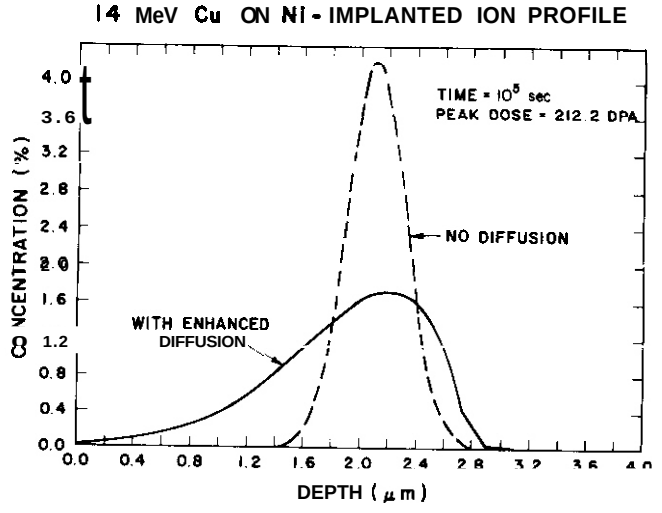

(b)

FIGURE 12. The Final Distribution of Copper After Irradiating an Initially Pure Nickel Foil at 525°C with 14 MeV Copper Ions. The concentration profile without radiation enhanced diffusion is also shown. a) After an ion fluence of 1.4 x 10^{16} cm^{-2}, b) After an ion fluence of 2 x 1017cm-2.

copper has spread throughout the damage region of the sample and reached peak concentration values exceeding 1.5 atom percent.

5. Discussion

a. Utility of Cross Sectioning Technique

Due to the large amount of data extracted by this sample preparation technique, it is important to understand its relative strengths and weaknesses. First, for a given sample, such variables as sample heat treatment history, handling, irradiation temperature, ion flux and ion fluence are all identical. While the absolute values of void statistics are no better with this technique than in conventional sample preparation, the relative error between intervals of a given sample is reduced since microscope magnification errors are eliminated and foil thickness errors are reduced.

The interpretation of the observed structure is complicated, however, by the depth variation of features such as dose rate, total dose, impurity levels, internally generated stress levels, surface effects, and the changing primary-knock-on (PKA) spectrum. The changing differential nuclear scattering cross section for nickel on nickel is shown for two depths in Figure 13a. As the ion slows down, cascades initiated by high energy PKA's are eliminated and the bulk of the displacement events are caused by lower energy, and hence smaller, cascades. This is shown more clearly in Figure 13b. Over 10 percent of the displacements at the surface are caused by recoils of energy greater than 1 MeV, while there are virtually no cascades of this size at a depth of 2 μm. Within our present understanding of the radiation damage process, it has not been possible to correlate this changing PKA spectrum with microstructural features, even though the cascade size could be expected to affect the fraction of defects surviving immediate recombination in the cascade. It is also possible that the cascade distribution could affect such mechanisms as cascade collapse into vacancy clusters.[21]

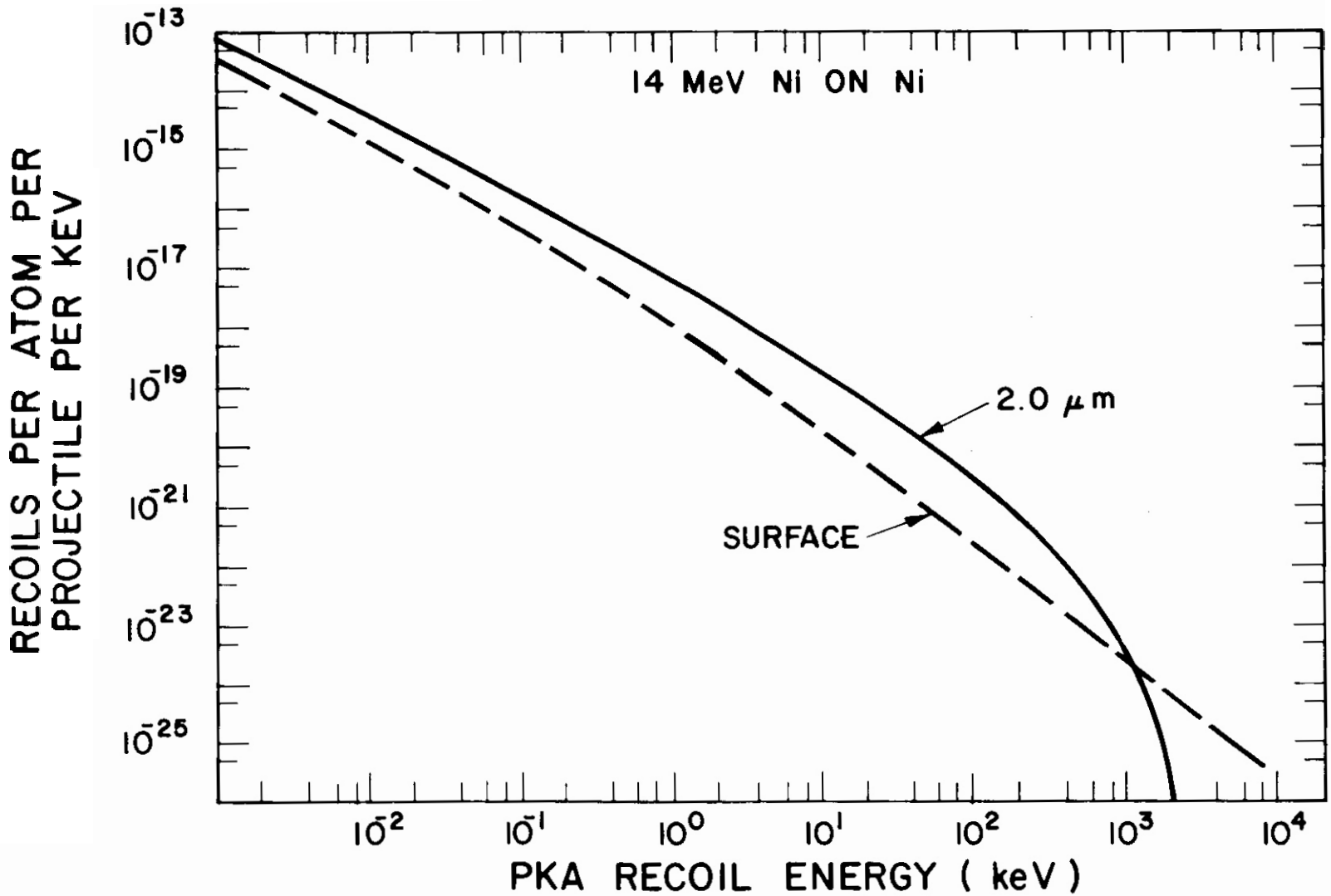

FIGURE 13a. The Differential Scattering Cross Section for 14 MeV Nickel Ions Incident on Nickel at the Surface and at a Depth Corresponding to the Peak Damage.

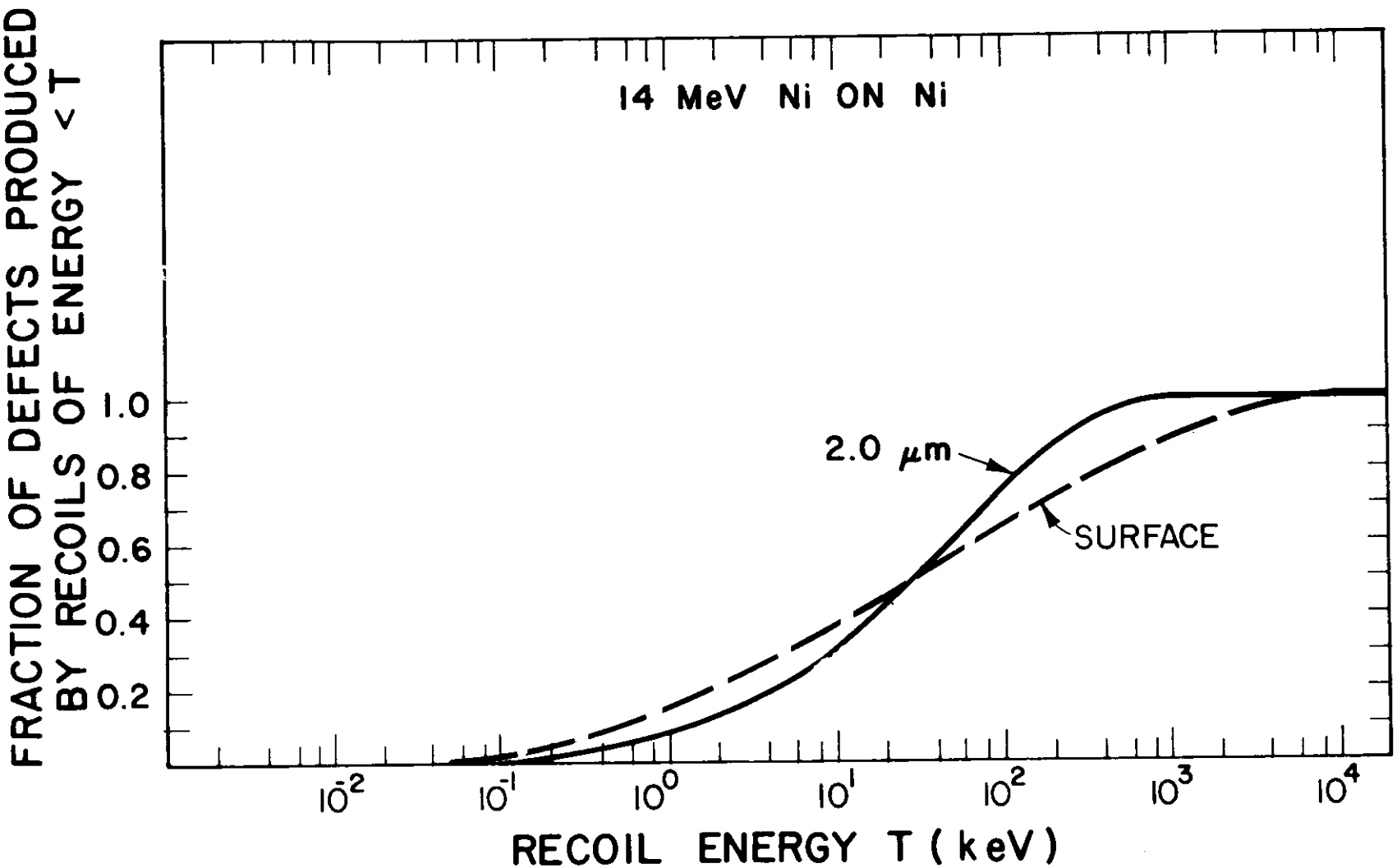

FIGURE 13b. The Function $F(\underline{T}<)$ at These Same Two Depths Where $F(\underline{T}<)$ is Taken After Marwick[17] and is Defined as the Fraction of Displacements Produced by Recoils of Energy Less Than $\underline{T}$.

To avoid smearing out microstructural data that may be affected by these rapidly varying features, it was necessary to restrict the depth interval size to the relatively small value of 0.25 μm. This restriction leads to the primary problem with this technique, namely that of counting statistics. In a sample or region of a sample that has a low defect density, it may be difficult to include enough defects within an interval to give an acceptable statistical uncertainty. In this study, the samples had high enough void densities to reduce this problem except in the first one or two depth intervals, but this technique would be very limited as a method of measuring the depth dependence of defects with densities below $\approx 5 \times 10^{13}$ cm^{-3}.

b. Microstructure Observations

In all samples which were examined in this study, voids were observed at depths from 15–20 percent greater than the end-of-range predicted by Brice[**] or Manning and Mueller.[22] The void density peak was also shifted beyond the predicted damage peak, but generally by only ≈10 percent. These results are consistent with earlier results[5] and with the observations of Narayan, et al.,[23,24] in heavy ion irradiated copper and nickel. The latter found better agreement between the observed defect density peak and the damage peak given by Manning and Mueller if the coefficient of the Lindhard electron energy loss term was reduced at low ion energies. By reducing the rate of electronic energy loss and correspondingly increasing the nuclear stopping power, the damage curve was shifted away from the front surface and the total number of displacements increased. An error in the range straggling calculation would also extend the damage region, as would channelling of either the incident ion or a high energy recoil atom. The diffusion of vacancies into this region could lead to void formation without extending the damage curve as was shown in the calculations of Figure 10. No definite conclusion, therefore could be drawn as to the cause of the range deviation in the present work but this discrepancy should be carefully studied in future work.

The front surface of these samples showed a void denuded region of ≈100 nm at 525°C. There was a slight increase in void size immediately adjacent to the denuded region, but the amount of increase varied between samples and was generally less noticeable than the increase observed next to the void denuded regions of grain-boundaries. Due to the relatively large grain size of these samples, only a few grain boundaries were observed and these usually showed evidence of grain boundary migration during the irradiation, making an accurate comparison of denuded zone width impossible. Voids in different grains of a sample showed no noticeable difference in either the size or density profiles or in the extent of the void region. Hence, from this study, there is no evidence that the grain orientation has any strong influence on the damage microstructure.

c. End-of-Range Effects

The computer calculations for the final copper concentration profile showed that for this study, the copper impurities were confined to the end-of-range region. This implies that any modifications in swelling behavior due to the presence of the copper will only occur in this region. However, the effects of copper impurities on void swelling is still somewhat uncertain. Brimhall and Kissinger[25] and Mazey and Menzinger[26] both found a 2% copper, 98% nickel alloy to swell less than a pure nickel control sample, while Smidt and Sprague[27] found a 1% copper alloy to swell more. All these workers did observe a decreased void density and an increased void size with alloying, however. Brimhall and Kissinger also observed a higher density of prismatic loops in the alloy system, possibly indicating a reduction in the stacking fault energy with alloying. In this study, the copper seems to have lowered both the void density and the void size. In fact the different shapes of the swelling curves of Figure 7 show a reduced swelling rate in the end-of-range region of the copper irradiated sample. An even more dramatic effect would be expected if the sample were irradiated to a higher damage level.

The swelling behavior of the self-ion irradiated samples (Figure 7) does not directly follow the displacement curve. Specifically, the variation from mid-range to the peak swelling value is much smaller than the corresponding variation in the damage curve. In Figure 14, this shelling value is shown plotted along with the net flux of vacancies into a distribution of test voids calculated from the data of Figure 11. This "growth fluid"[b] is a valuable aid in interpreting void growth data. (While these curves are not exactly equivalent in that the growth fluid is a swelling rate, the discrepancy is minor since the small incubation dose of pure materials allows one to approximate a swelling rate by a single swelling value.) The good qualitative agreement between these curves indicate that the reduced swelling value per dpa in the peak region can be at least partially explained by the enhanced recombination and the excess interstitials deposited in the end-of-range region. Note that this result is similar to that obtained by the internal temperature shift at temperatures below the peak swelling temperature as described by Garner and Guthrie.[3] In calculating the growth fluid, however, a void distribution was assumed, while the experimental temperature shift includes the temperature and rate variations in void nucleation.

6. Conclusions

The cross sectioning method of post-irradiation sample preparation for heavy ion bombarded nickel has proven to be a valuable aid in understanding the irradiation microstructure produced by this simulation technique. This study has found:

1. The swelling rate per dpa in the end-of-range region was decreased significantly for both copper and nickel ion irradiations compared to the mid-range values. The copper ion irradiated sample displayed a somewhat lower variation than the self-ion bombarded specimen.

b. The growth fluid is defined by Garner[3] as $D_v C_v - D_i C_i - D_v C_v^*$, where C_v^* is the vacancy concentration at the void surface with no irradiation.

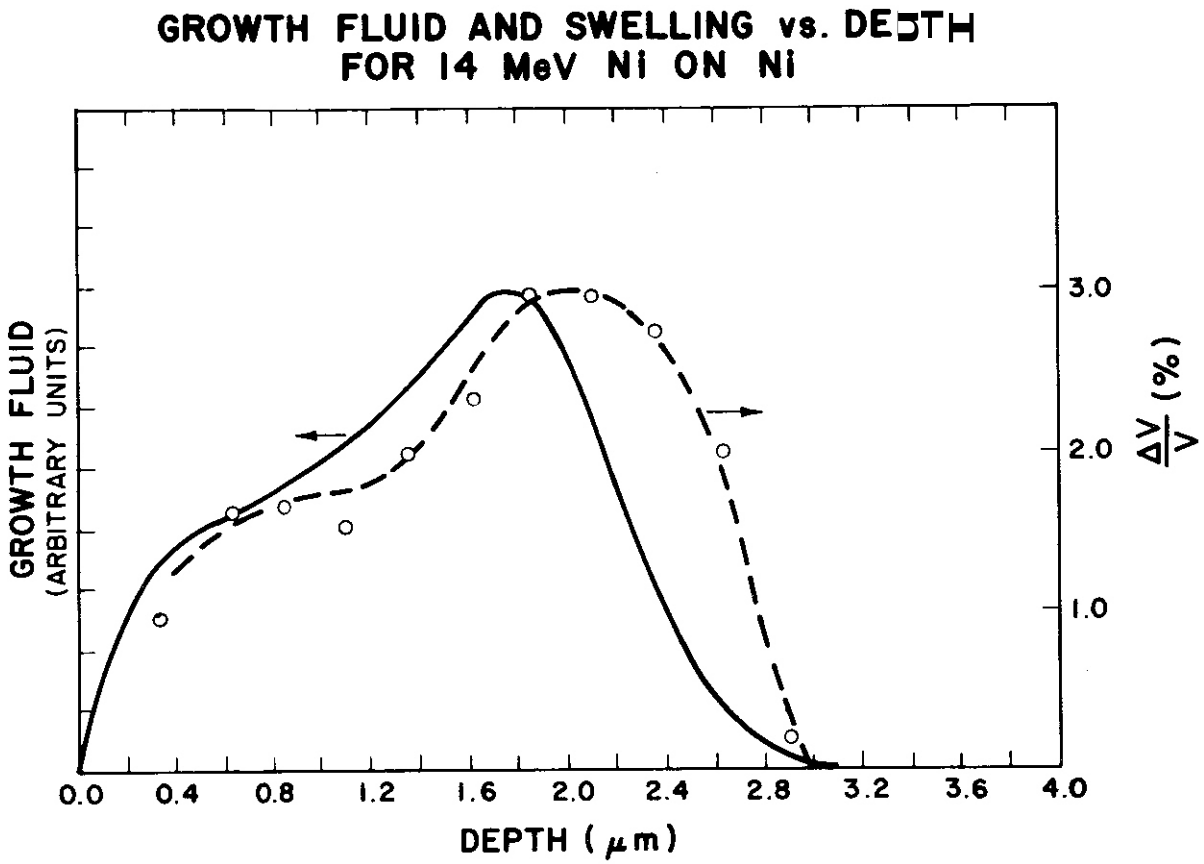

FIGURE 14. The Net Flux of Vacancies into a Given Void Distribution (i.e., Growth Fluid) is Shown for the Calculations of Figure 10 along with the Swelling Curve of Figure 6b.

2. Calculations of the steady-state defect concentrations showed a decreased swelling rate at the end-of-range of the incident ions due to the higher recornhination rate.

3. By modeling the radiation enhanced diffusion of the implanted copper ions, it was shown that for the samples of this study, the copper was confined to the end-of-range region.

4. A void denuded region of ≈100 nm was observed at the front surface at 525°C, and voids were observed at depth ~15 percent greater than the extent of the predicted damage curve.

5. A loop lattice with a lattice spacing of 40 nm was observed after irradiation at 200°C, and the lattice spacing was not found to be dose rate or otherwise depth dependent.

VI. REFERENCES

1. G.L. Kulcinski, Applications of Ion Beams to Metals, Plenum Press, NY, p. 613 (1974).

2. W.G. Johnston and J.H. Rosolowski, Applications of Ion Beams to Materials, 1975, p. 228 (1975).

3. F.A. Garner and G.L. Guthrie, Int. Conf. on Rad. Effects and Tritium Technology for Fusion Reactors, CONF-750989 p. 1-491 (1976).

4. F. Menzinger and F. Sacchetti, J. Nucl. Mat. 57, p. 193 (1975).

5. J.B. Whitley, P. Wilkes, G.L. Kulcinski, UWFDM-159, Nuc. Engr. Oept., Madison, WI (1976).

6. R.A. Spurling and C.G. Rhodes, J. Nucl. Mat. 44, p. 341 (1972).

7. J.B. Whitley, G.L. Kulcinski, UWFOM-241, Nuc. Engr. Dept., Madison, WI (1987).

8. H.V. Smith and R.G. Lott, Nuc. Ins. and Methods 143, p.125 (1977).

9. D.K. Brice, SAND75-0622, Sandia Laboratories, Albuquerque, NM (July 1977).

10. T.O. Ryan, Ph.D. Thesis, Univ. of Mich. (1975).

11. Recommended practice for neutron damage simulation by charged particle irradiation, E521-76 (Prepared under ASTM Committee E-10, Subcommittee E10.08) (1974).

12. T.M. Rodgers, Handbook of Practical Electroplating, p. 225, Macmillian Co., NY (1959).

13. G.L. Kulcinski and J.L. Brimhall, Effects of Rad. on Substructure and Mech. Prop. of Metal and Alloys, ASTM STP 529, (1973) p. 258.

14. J.A. Sprague, J.E. Westmoreland, F.A. Smidt, Jr., and P.R. Malmberg, J. Nuc. Mat. 54, p. 286 (1974).

15. J.E. Westmoreland, J.A. Sprague, F.A. Smidt, Jr., and P.R. Malmberg, Rad. Eff. 26, p. 1 (1975).

16. A.D. Brailsford and R. Bullough, J. Nuc. Mat. 44, p. 121 (1972).

17. S.M. Myers, D.E. Amos, D.K. Brice, J. App. Physics, No. 5, p. 1812 (1976).

18. G.R. Odette, D.M. Schwartz, and A.J. Ardell, Rad. Eff. 22, p. 217 (1974).

19. Y. Adda, M. Beyeler, and G. Brebec, Thin Solid Films 25, p. 107 (1975).

20. A.D. Marwick, Consultant Symposium on The Physics of Irradiation Produced Voids, Harwell, p. 39 (1975).

21. R. Bullough, Consultant Symposium on The Physics of Irradiation Produced Voids, Harwell, p. 275 (1975).

22. I. Manning and G.P. Mueller, Computer Phys. Comm. 7, p. 85 (1974).

23. J. Narayan and O.S. Oen, J. Nuc. Mat. 66, p. 158 (1977).

24. J. Narayan, O.S. Oen, and T.S. Noggle, J. Nuc. Mat. 71, p. 160 (1977).

25. J.L. Brimhall and H.E. Kissinger, Rad. Eff. 15, p. 259 (1972).

26. D.J. Mazey and F. Menzinger, J. Nuc. Mat. 48, p. 15 (1973).

27. F.A. Smidt and J.A. Sprague, NRL Mem. Report #2998, p. 39 (March 1975).

VII. FUTURE WORK

The effect Al and carbon ions on the displacement damage produced in high purity nickel will be studied at 525°C up to 2 x 10^{16} ions/cm^2.

VIII. PUBLICATION

1. G.L. Kulcinski, "Progress in Materials Research for Fusion Reactors", IAEA Conf. on Reactor Design, Madison, 1977 to be published in Nuc. Fusion.

2. J.B. Whitley, G.L. Kulcinski, P. Wilkes and H.V. Smith, Jr., "The Depth Dependent Damage Profile in Nickel Irradiated with Nickel or Copper Ions", submitted to J. Nuc. Materials.

3. J.B. Whitley, G.L. Kulcinski, P. Wilkes and H.V. Smith, Jr., "Effects of Bombarding Ions on the Void Swelling Profile in Nickel", 9th ASTM International Symposium on Effects of Radiation on Structural Materials", Richland, WA, 1978.

I. PROGRAM

Title: 14 MeV Neutron Irradiation Studies
Principal Investigator: Richard R. Vandervoort
Affiliation: Lawrence Livermore Laboratory

II. OBJECTIVE

This project has the following principal objectives: 1) to characterize 14 MeV neutron damage; 2) to compare radiation damage from 14 MeV neutrons, Be(D,n) neutrons, and fission reactor neutrons; and 3) to evaluate the effect of helium on the mechanical properties of Nb and Nb-1%Zr.

III. RELEVANT DAFS PROGRAM PLAN TASK/SUBTASK

SUBTASK	II.C.6.3	Low Fnergy-High Energy Neutron Correlations
	II.C.7.1	Helium Injection Experiments
	II.C.11.4	High Energy Neutron Irradiations
	II.C.18	Relating Low and High Exposure Microstructures

IV. SUMMARY

A. 14 MeV Neutron Damage

Tensile specimens of Nb-1%Zr were irradiated at room temperature by high-energy neutrons from the Rotating Target Neutron Source (RTNS-I) and by lower-energy neutrons from the Livermore Pool-Type reactor (LPTR). After being irradiated, specimens were tensile tested, and the increases in their 0.2%-offset yield strengths were related to the neutron fluences. In this alloy, about 11 times as great a fluence of neutrons ($E > 0.5eV$) from the LPTR was required to produce the same increase in yield strength as RTNS 14 MeV neutron fluences above $10^{17} n/cm^2$. In terms of yield-strength increase versus displacement

damage energy (eV/atom), the results showed that the radiation strengthening in this alloy was essentially identical for the RTNS and LPTR neutrons.

Irradiation of Nb and Nb-1%Zr with 14 MeV neutrons at 700°C and 600°C respectively produced no changes in yield strength for fluences of about $10^{17} n/cm^2$.

B. Effect of Helium on the Mechanical Properties of Nb and Nb-1%Zr

Niobium and Nb-1Zr specimens have been doped with helium from 25 to 500 appm using the "tritium trick". This process was described in the previous progress report.(1)

As helium content increases in Nb and Nb-1Zr materials, the tensile strength increases and the ductility decreases progressively.(1) In the as-doped condition, the loss in ductility was not deleterious at any helium content studied. But the ductility of niobium with 500 appm ^3He dropped essentially to zero as a result of an additional 50 hour heat treatment at 1200°C after charging. Fracture occurred in a brittle fashion and was completely intergranular. TEM evidence showed that this high temperature treatment had caused gross redistribution of helium from the matrix into the grain boundaries.

Creep tests on base line niobium give an apparent activation energy of 52 kcal/mol in the temperature region 800" to 1000°C. The stress dependence of creep rate at 800°C is given by $\dot{\varepsilon} = K\sigma^n$ where K is a constant and n-10.

V. ACCOMPLISHMENTS AND STATUS

A. 14 MeV Neutron Damage -- J. B. Mitchell

1. Introduction

Fusion neutrons will create a larger number of atom displacements per primary collision than lower energy (1-2 MeV) fast fission neutrons and internal helium generation from (n,α) reactions will be substantially greater for fusion neutrons than for fast fission neutrons. Thus, we expect that the deleterious effects of radiation damage that have been experienced in fission-reactor materials will be even more severe in fusion reactors.

Studies are in progress to determine the characteristics and effects of 14 MeV neutron damage and to compare the nature and magnitude of these effects with radiation damage from Be(D,n) neutrons and fission reactor neutrons.

2. Specimens and Experimental Procedure

Small tensile specimens of Nb-1%Zr were machined from 0.5 mm thick (0.020 in.) sheet stock. Overall specimen length was 28.6 mm. The gage section was 6.35 mm long and 1.57 mm wide. Interstitial impurities in the alloy are shown in Table I.

TABLE I CHEMICAL ANALYSIS OF INTERSTITIAL IMPURITIES IN Nb-1%Zr

Element	Concentration (appm)
C	92
O	185
N	40

The specimens were annealed for 1 hour at 1550°C in a vacuum of 0.13 Pa (~ 10^{-9} torr). This annealing treatment was selected to obtain grain sizes that would give at least ten grains over the 0.5 mm specimen thickness to insure reproducible polycrystalline tensile behavior.

Specimens were irradiated at the Rotating Target Neutron Source (RTNS-I) and at the Livermore Pool Type Reactor (LPTR). For elevated temperature irradiations the tensile specimens were enclosed along with dosimeter foils in an evacuated platinum capsule. The capsule was heated by a spot lamp heater. After irradiation, the specimens were tested in an Instron testing machine at about 23°C and a crosshead rate of 0.05 mm/min (0.002 in./min). The 0.2% offset yield stress was determined using the Instron crosshead motion as the sample extension.

3. Results and Discussion

The increase in 0.2%-offset yield stress versus neutron fluence for Nb-1%Zr is shown in Fig. 1. It is apparent from this graph that the high-energy neutrons from the RTNS are more effective than the lower-energy neutrons from the LPTR in strengthening this alloy.

The ratio of neutron fluences from the LPTR (E > 0.5 eV) and RTNS to produce the same increase in yield strength in Nb - 1%Zr is about 11 (or about 5.5 when counting LPTR neutrons above E > 0.1 MeV). This ratio is about half that for the Nb, V, and Cu.[1] It appears that this reduced ratio can be accounted for solely by the greater radiation strengthening produced by the LPTR in Nb-1%Zr.

Fig. 2 shows that the yield-strength increase produced by the RTNS and LPTR neutron scales with damage energy. This result is different from that for Cu, Nb, and V. It appears that the enhanced radiation strengthening of Nb-1%Zr results from trapping of the point defects by the higher content of impurities.

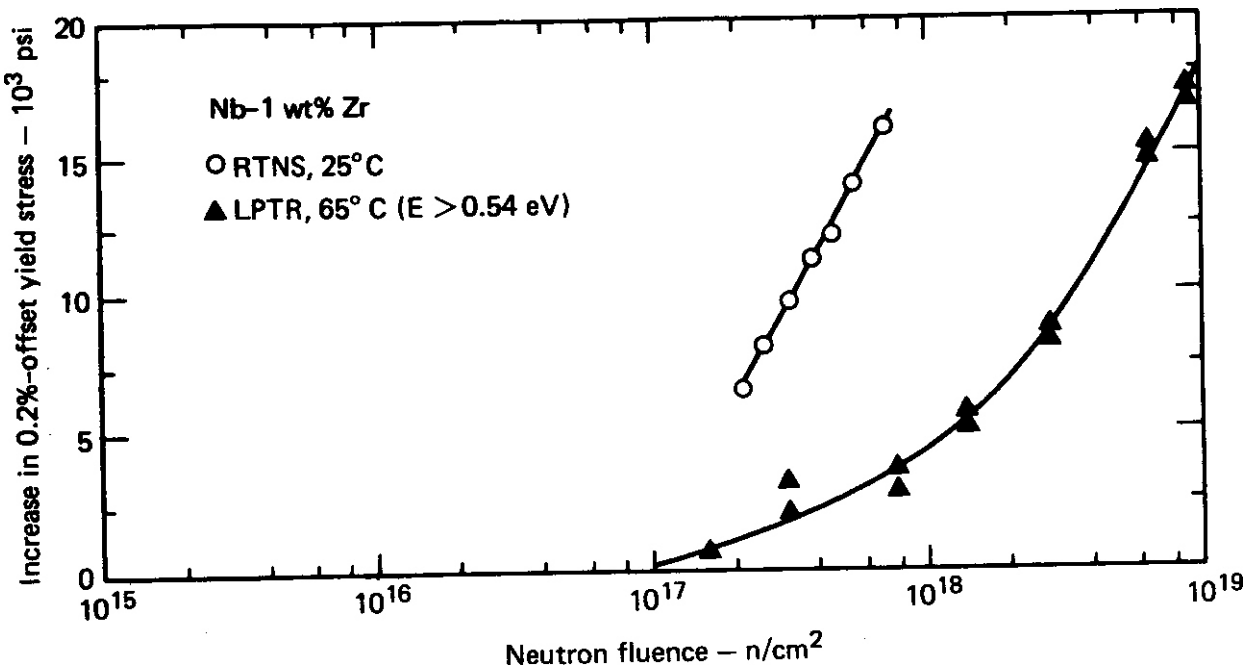

Figure 1 Increase in 0.2%-offset Yield Stress as Neutron Fluence for RTNS and LPTR Irradiations of Nb-1 w % Zr

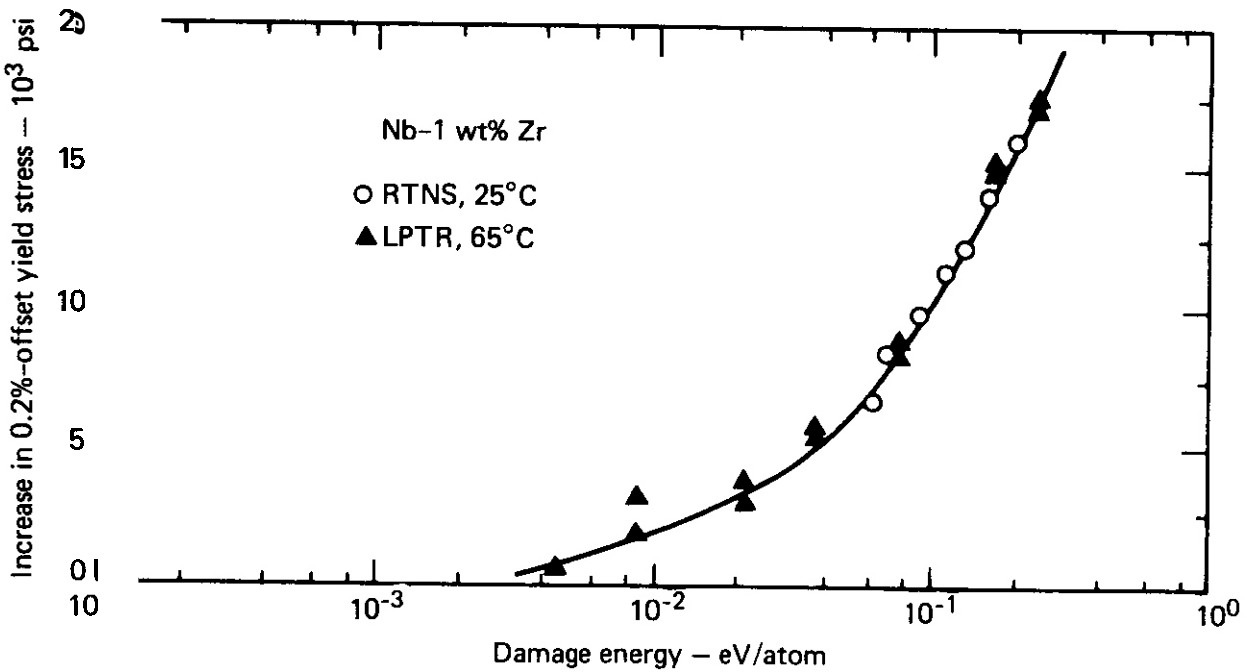

Figure 2 Increase in 0.2%-offset Yield Stress vs Damage Energy for Neutron-irradiated Nb-1 wt% Zr.

RTNS irradiations of Nb at 700°C and fluences UD to about 10^{17} n/cm^2. and of Nb-1%Zr at 600°C and 2.5 X 10^{17} n/cm^2, produced no observable radiation strengthening. At these elevated temperatures, apparently annealing of the displacement damage moves the threshold for observable strengthening to a significantly higher fluence.

B. Effect of Helium on the Mechanical Properties of Nb and Nb-1%Zr

-- W. L. Barmore and R. R. Vandervoort

1. Introduction

High energy (E ~ 14 MeV) neutron radiation from fusion reactors will cause enhanced damage to the microstructures of component materials. The displacement damage per incident 14 MeV neutron is greater, and cross sections for (n,α) reactions also are higher for fusion neutron irradiation than for fission neutron irradiation.

Mechanical properties of component materials are changed by large concentrations of internally generated helium. Because of high (n,α) cross sections significant quantities of helium will be produced in fusion reactor materials irradiated by 14 MeV neutrons in a relatively short time span. A concentration of 25-50 appm helium will be produced internally in niobium by a fusion neutron flux of ~ 10^{18} neutrons m^{-2}sec^{-1} with one year's exposure. Helium atoms produced at a high concentration in a host matrix having low helium solubility, are thermodynamically unstable and have a high driving force to coalesce in the microstructure at various defects. Thus, helium atoms tend to migrate to dislocations, precipitates, grain boundaries impurity particles and microcracks where they coalesce to form bubbles. These helium-induced defects generally cause embrittlement.

Changes in the mechanical properties of Nb and Nb-1%Zr doped with ^{3}He by the "tritium trick" method to as high as 500 appm are under investigation.

2. Results and Discussion

As helium content increases, the strength increases and ductility decreases progressively for specimens tensile tested at 23°C. The fracture ductility of the niobium base material compared with niobium containing 500 appm helium was reduced from 60% to 30%. After annealing 50 hours at 1200°C, the fracture ductility of niobium with 500 appm helium was essentially zero, and the fracture mode was completely intergranular.

The microstructure was examined by TEM to elucidate this drastic loss in ductility. Helium in as-charged specimens was randomly distributed in the matrix as bubbles and very small clusters less than 10 nm in size. Helium in specimens charged and annealed 50 hours at 1200°C formed large bubbles preferentially on grain boundaries with a few isolated groups of bubbles located heterogeneously in the matrix. Bubbles in annealed specimens were geometrically shaped and were as large as 150 nm. Bubbles can be interpreted as dodecahedrons with {110} faces.

The results show that annealing of helium-charged niobium enhances bubble growth, promotes gross movement of helium to grain boundaries, and causes pinning of dislocations at helium bubbles in the matrix. This redistribution of helium hardens the matrix to plastic deformation by dislocation motion and weakens grain boundaries to intergranular fractures.

Thus, analysis of the microstructure demonstrates conclusively that formation of helium bubbles on grain boundaries embrittles niobium when tested at 23°C, a temperature where niobium is normally very ductile.

Creep of niobium at 800°C and above can be described by the relation $\dot{\epsilon} = f(s)\sigma^n e^{-\frac{AH}{RT}}$

where: $\dot{\varepsilon}$ = creep rate
$f(s)$ = a function of the microstructure
σ = axial stress
n = stress exponent constant
ΔH = the apparent activation energy for creep
R = gas law constant
T = absolute temperature

ΔH is determined by analyzing creep rate data at several temperatures where stress and $f(s)$ are constant, the stress exponent, n, is obtained from creep rate data at various stress levels where $f(s)$ and temperatures are constant. The structure function, $f(s)$, includes factors of grain size and morphology, precipitate concentration and distribution, dislocation, density etc. The classic shape of creep curves is determined by the structure function; $f(s)$ decreases in the primary creep region, is constant in the secondary creep region and increases in the tertiary creep region.

Helium effects should result primarily in modifying $f(s)$ where the same deformation mechanism is creep rate controlling.

At a stress of 55 MPa (~8 ksi), the apparent activation energy for creep of niobium is 52 kcal/mol in the temperature region 800" to 1000°C.

The stress exponent for the Nb baseline material is ~10 at 800°C.

VI. REFERENCES

1. DAFS Quarterly Report, Jan. - Mar., 1978.

VII. FUTURE WORK

A. 14 MeV neutron Damage - Determine changes in tensile properties of 316 stainless steel irradiated with 14 MeV neutrons.

B. Effect of Helium on Mechanical Properties *of* Nb and Nb-1%Zr - Determine the stress law for Nb doped with helium.

I. PROGRAM

Title: Simulating the CTR Environment in the HVEM
Principal Investigator: D. Kuhlmann-Wilsdorf
Affiliation: University of Virginia

II. OBJECTIVE

The objective of this work is to evaluate the effects of irradiation with helium ions and neutrons on the fracture of 304 and 316 stainless steel.

111. RELEVANT DAFS PROGRAM TASK/SUBTASK

Subtask II.C.8.2 Post Irradiation Testing

IV. SUMMARY

In-situ HVEM tensile tests were made on samples of un-irradiated 316 stainless steel, neutron irradiated 304 stainless steel from EBR-II, and 80 keV helium irradiated 316 stainless steel. These were performed at room temperature and at 600°C.

The most important results obtained concern the two types of neutron irradiated samples which were tested at high temperatures. These samples, one containing a high void density and the other a high dislocation (loop) density were irradiated in the EBR-II under unspecified neutron irradiation history. Fracture tests of these samples (performed under the same experimental conditions) produced two distinct types of fracture as follows: the samples containing voids fractured in a ductile mode, somewhat transgranularly, and those without voids but with a high loop density fractured in a brittle intergranular mode.

Another significant result obtained involved the annealed 316 stainless steel irradiated with 80 keV helium ions and tested at room temperature. After being irradiated to a fluence of 2.6 X 10^{17} ions cm^{-2} with a flux of 3.3 x 10^{14} ions cm^{-2} sec^{-1}, the sample was fractured. In addition to failing in a ductile mode, the sample exhibited very large, regularly spaced, radiation induced slip steps on its sides adjacent to the fracture surface.

V. ACCOMPLISHMENTS AND STATUS

A. In-situ HVEM Tensile Tests of Irradiated and Un-irradiated Stainless Steel -- J. I. Bennetch, J. A. Horton, W. A. Jesser, D. Kuhlmann-Wilsdorf, R. A. Johnson, and H. G. F. Wilsdsorf, (University of Virginia, Charlottesville, VA)

1. Introduction

In our experimental set-up, described previously[1] a light ion accelerator, attached to a 500 keV HVEM, directs an ion beam into the specimenarea of our 500 keV electron microscope in its lens gap, oriented normal to the electron beam. In this arrangement, the magnetic field of the objective lens provides the final mass separation of the ions with the result a very pure beam of 3 X 10^{14} ions cm^{-2} sec^{-1} can be directed to the sample. 'The specimen, while under observation and being ion bombarded, can also be simultaneously heated to controlled temperatures up to about 700°C and be stressed mechanically to fracture if desired. Thus a wide range of in-situ observations are possible.

2. Experimental Data

The equipment and the sample preparation were both described in the Spring 1978 DAFS Progress Report.[2] Table I below summarizes the tests made in the current report period. From here on, samples and tests will be referred by their number in Table I.

The EBR-II neutron irradiated samples of experiments 10 and 12 were punched out of the same sheet of material as that of experiment 5. These samples had a high loop density ($4 \times 10^{14} cm^{-3}$) whose size was too small to be resolved; voids were practically nonexistent in their microstructure. Sample 4, punched from a different sheet of material, contained a large void population (10^{14} cm^{-3}) of 30 nm size. No information on the neutron irradiation history was specified.

TABLE 1

IN-SITU HVEM TENSILE EXPERIMENT

Experiment	Material (s.s.)	Testing Temp.	Pretreatment
4 (Ref. 2)	304 s.s.	600°	neutron irrad.
5 (Ref. 2)	304 s.s.	room T	neutron irrad.
6	316 s.s.[a]	600°	unirrad.
7	316 s.s.[a]	600°	unirrad.
8	316 s.s.[a]	600°	unirrad.
9	316 s.s.[a]	600°	neutron irrad.
10	304 s.s.	600°	neutron irrad.
11	316 s.s.[a]	room T	helium irrad.
12	304 s.s.	600°	neutron irrad

[a] Each 316 stainless steel sample was annealed at 1000°C for 1 hour

3. Results and Discussion

Three neutron irradiated samples (i.e. 5, 10, and 12) were prepared from the same sheet of material provided by J. O. Steigler at ORNL and pulled with similar elongation rates, one at room temperature and the other at 600°C. These samples have a high density (4×10^{14} cm^{-3}) of very small loops ($\leq$ 20 nm in diameter), but few, if any, voids.

Sample 5 was fractured at room temperature. It exhibited a relatively ductile mode of fracture. In the thinnest areas, up to ~ 0.1 μm, the cracks propagated along light bands or faults, tentatively identified as slip bands. Evidently, plastic deformation precedes the crack tip since the material ahead thins out and vigorous dislocation motion can be discerned. Further, the same sequences of holes which are typical for this kind of fracture were observed to form in front of the crack.[3] Also quite typically, as the crack widened thin ligaments with crystallographic sides were pulled out of the crack flank.[4]

The fracture behavior when tests 10 and 12 were performed at 600°C was dramatically different from the room temperature test (as described above). Now pronounced brittle, intergranular fracture occurred.

In experiment 10, the main crack formed in the thicker area immediately surrounding the electropolished hole in the sample. This crack grew to a 60 μm length with only a 2 μm width in the initial stages of deformation. Simultaneously, other cracks formed at grain boundaries which intersected the electropolished hole. These cracks were also long and narrow. While the crack tip radii of about 0.1 μm did not differ significantly from those in test 5 at room temperature as well as from previous experiments with unirradiated high temperatures s.s. 316 (which all showed a ductile mode) (') the

extraordinary fact that such a relative profusion of cracks initiated dramatically proves the great embrittlement of these samples at the testing temperature.

The characteristic, very evident differences among the above samples will be further discussed in conjunction with SEM micrographs showing the typical fracture surfaces.

Figure 1.a shows a micrograph of the fracture surface of sample 10 fractured at 600°C. A closer look at surface details (see figure 1.b) reveals small dark spots. We believe these to be precipitates, but identification has not yet been completed, pending micro-analysis to ascertain the chemical composition.

In performing the tensile experiments, the samples are heated and their temperature is allowed to stabilize for approximately a half hour, before the actual test is begun. As samples 10 and 12 had been neutron irradiated at 375°C for extended periods, one might think that (n,a) produced helium would migrate to the grain boundaries during the described heating of the rather higher test temperature of 600°C. It is more than tempting to hypothesize that this is responsible for the brittle fracture. However, no bubbles were observed in the HVEM during the test and no differences were observed in the thinnest areas where the surface would act as the major sink.

These results are in general conformity with those by Clausing and Bloom[5] who reported similar fracture results in 304 s.s. irradiated at 370°C and pulled at 550°C. These authors surmised that since no helium bubbles were visible in the TEM, any bubbles at the grain boundaries must have been too small to be resolved ($\leq$ 20 nm), or the helium collected in the form of a partial monolayer at the boundary.

Figure 2, in contrast to Figure 1, shows a SEM fracture surface of ductile nature of the kind which is formed if the

test is performed at room temperature. In fact, Figure 2 was obtained from tensile test #4 at 600°C on a neutron irradiated sample with a stable void population. The type of fracture surface in Figure 2 offers a striking comparison with Figure 1.

Direct HVEM observation and micrographs obtained in test 4 indicated that the crack in that case was initiated in a void and that it propagated through voids. Remarkably, the behavior of the same stainless steel, i.e. 304 s.s., albeit with a different pre-irradiation history and microstructure, but pulled at the same temperature (600°C) under the same conditions, can be totally different. In this case, even though the pre-irradiation was conducted to a higher dose in sample 4 than in samples 5, 10 and 12, the ductile fracture of Figure 2 was observed whereas Figure 1 exhibits the brittle fracture of samples 10 and 12 as discussed. Surprisingly, therefore, the many voids in sample 4 did cause by far less extreme embrittlement than is seen in the void-free samples 10 and 12.

We may tentatively conclude (presumably in line with the thoughts of many others) that the disposition of the helium is the critical factor, i.e. being relatively harmless when aggregated into voids but disastrous when concentrated at grain boundaries.

To further elucidate the role of helium migration in the fracture mechanism, experiments were done using in-situ 80 kV helium ion irradiations on the tensile specimens. Figure 3 shows a scanning micrograph of a sample helium irradiated and subsequently fractured at room temperature. The pretreatment is described in the legend to Figure 3.

Note the very prominent regularly spaced slip steps in Figure 3 of about 1 μm. These steps could be a result of

preferential sputtering, since the ion beam is inclined at 60^{o} to the surface. However, it is also well possible that these lines are rather regularly spaced pronounced slip lines. Such lines are known to occur in material with a high concentration of point defects. They are formed because any moving dislocation sweeps up point defects in its path, thereby softening the material in its wake and causing a concentration of further deformation there.(6,7,8)

Since the lattice is saturated with helium the sweeping out effect caused by the dislocations moving through the lttice and leaving depleted regions could thus be connected specifically with the helium.

The chisel fracture edge seen in Figure 3 is characteristic of ductile fracture. Also the TEM observations of this experiment showed the typical features of ductile fracture, much the same as those of a well annealed sample pulled at room temperature.

Not visible in Figure 3 are some of the thicker areas which showed ion induced blistering while the thinner areas adjacent to the fracture did not reveal this feature. Further tests with helium irradiations but at higher temperatures, for correlation with the already discussed effect of high temperature on helium embrittlement, are planned.

Also planned are investigations on helium irradiation to produce void or bubble filled samples and compare their ductility at high temperature to that of a helium saturated sample having no voids or bubbles. Voids or bubbles of a small size (2.5 - 5.0 nm in diameter) have been produced with a density of 10^{11} in 316 s.s. at 600^{o} in the HVEM ion irradiation facility.

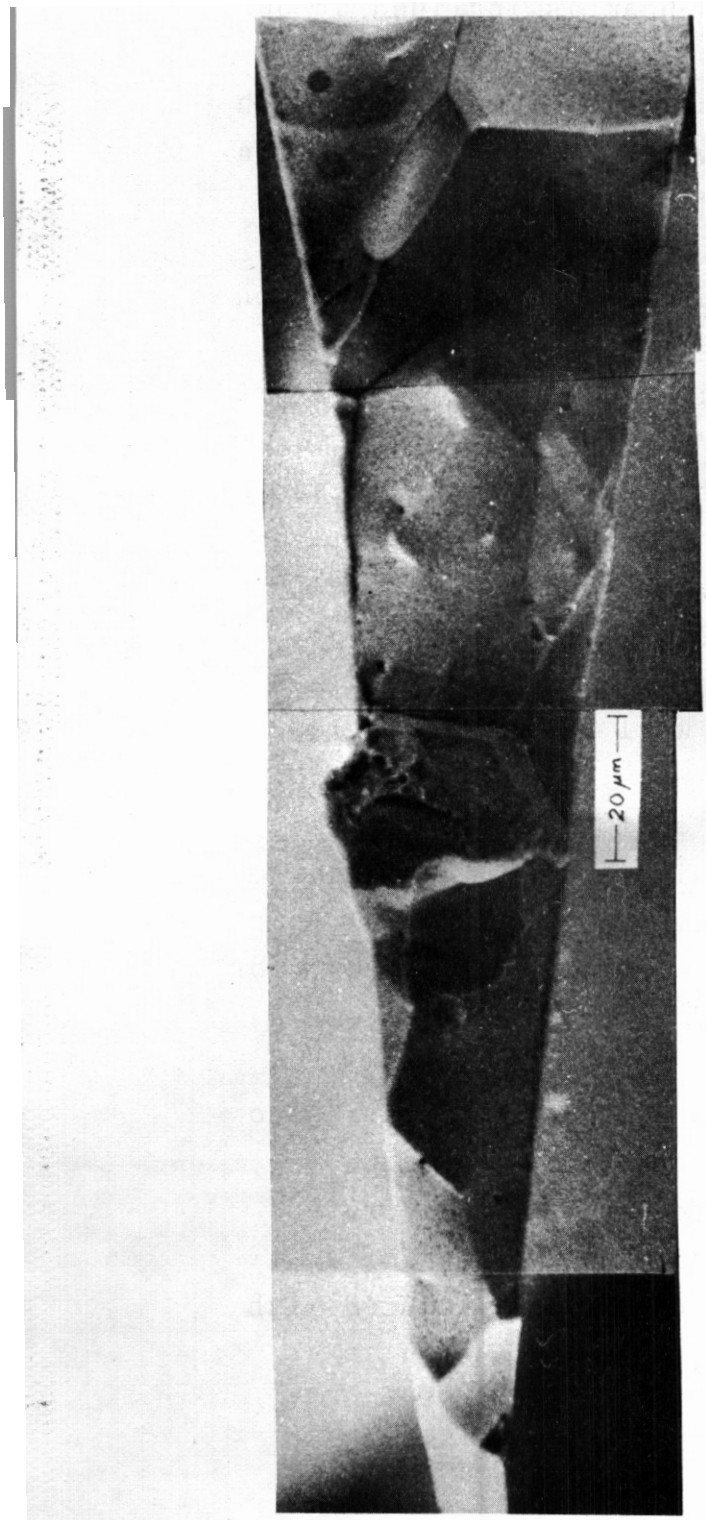

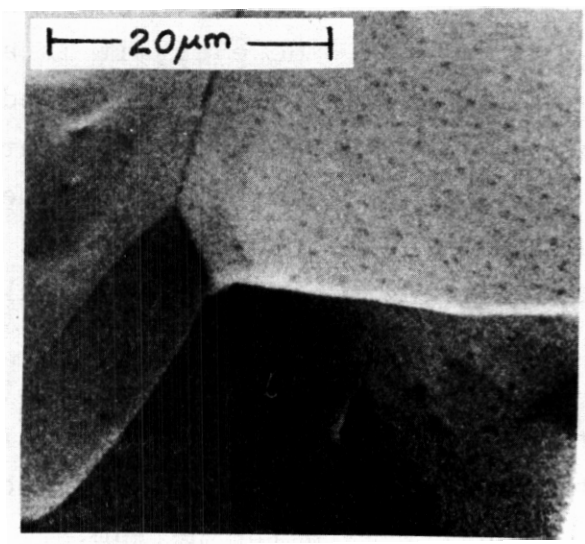

Figure 1.a SEM micrograph of the fracture surface of a neutron irradiated **304** stainless steel sample fractured at 600°C showing a brittle intergranular failure.
Figure 1.b Magnified area of the same sample showing black spots on the fracture surface.

Figure 2
SEM micrograph of the fracture surface of a neutron irradiated 304 stainless steel sample containing many voids. The sample was pulled at 600°C and shows a ductile fracture surface.

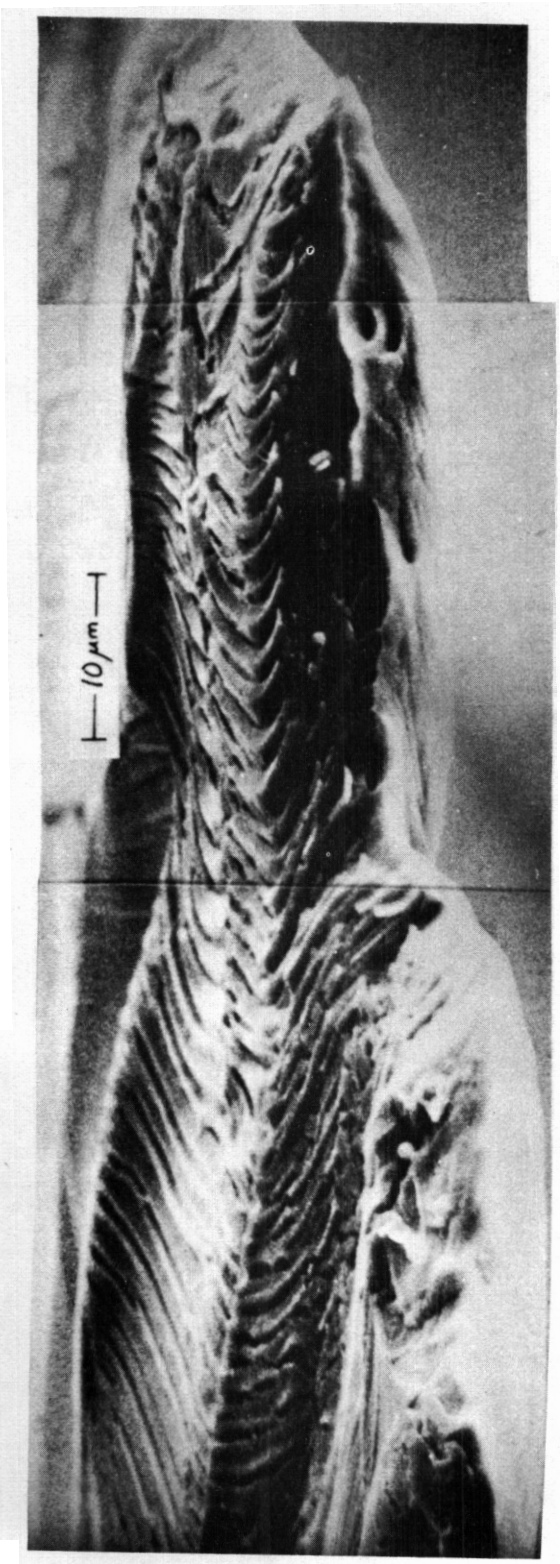

Figure 3
SEM micrograph of annealed 316 stainless steel irradiated with 80 kV helium at a 'flux of 3.3 x 10^{14} ions/cm2sec to a fluence of 2.6 x 1017ions/cm2 sec and then fractured.

VI. REFERENCES

1. J. I. Bennetch, J. A. Horton, W. A. Jesser, "Ion accelerator-HVEM link", Proc. 35th Annual Meeting EMSA. G. W. Bailey, ed.. Claitor's Pub. Div. Baton Rouge, (1977) p. 96.

2. W. A. Jesser, J. A. Horton, J. I. Bennetch, "In-situ HVEM tensile tests of irradiated and unirradiated stainless steel", Quarterly Technical Progress Report DAFS, D. G. Doran, ed., Hanford Eng. Div. Laboratory, (Spring 1978), p. 204.

3. R. W. Bauer, H. G. F. Wilsdorf, "The mechanical behavior in tension and fracture characteristics of stainless steel thin rolled foils", Proc of Int'l. Conf. on Dynamic Crack Propagation, G. C. Sih, ed., Noordhoff Int. Pub., Leyden, (1972) p. 197.

4. R. L. Lyles, Jr., H. G. F. Wilsdorf, "Microcrack nucleation and fracture in silver crystals", Acta Metallurgica, 23, (1975) p. 269.

5. R. E. Clausing, E. E. Bloom, "Auger spectroscopy of fracture surfaces in irradiated type 304 stainless steel", Grain Boundaries in Engineering Materials, J. L. Walter, J. H. Westbrook, D. H. Woodford, eds., Claitors Pub. Div. Baton Rouge, (1975) p. 491.

6. H. G. F. Wilsdorf and D. Kuhlmann-Wilsdorf, Phys. Rev. Lett. 3 (1959) p. 170-172.

7. D. Kuhlmann-Wilsdorf, R. Maddin, and H. G. F. Wilsdorf Strengthening Mechanisms in Solids, J. J. Harwood, ed., Am. Soc. Metals, Metals Park, OH (1962) pp. 137-178.

8. I. G. Greenfield and H. G. F. Wilsdorf, Naturwiss. (1960), p. 395-396.

ACKNOWLEDGEMENTS

The pre-irradiated samples investigated in this research have been provided by J. O. Stiegler of Oak Ridge National Laboratory through the good offices of T. C. Reuther (Mat. and Rad. Effects Branch, DOE). This invaluable aid is greatly appreciated.

VII. FUTURE WORK

As indicated in the main body of this work, tensile tests of similar samples will continue. In addition to the experimental work described above, a computer modeling study has been initiated to calculate interstitial, vacancy, and helium concentrations under irradiation conditions similar to those used in the experiments.

DISTRIBUTION FOR DAFS QUARTERLY REPORTS

UC-20 (117)
UC-20c (78)
APPROVED SPECIAL DISTRIBUTION (82)

Argonne National Laboratory (5)
9700 South Cass Avenue
Argonne, Illinois 60439

L. R. Greenwood
S. D. Harkness
V. H. Maroni
F. V. Nolfi, Jr.
H. Wiedersich

Atomics International (1)
Component Engineering and Technology Division
North American Rockwell
8900 DeSoto Avenue
Canoga Park, California 91304

H. Farrar, IV

Battelle-Northwest (5)
P. O. Box 999
Richland, Washington 99352

J. L. Brimhall
A. B. Johnson
R. H. Jones
L. C. Schmid
D. Styris

Brookhaven National Laboratory (2)
Associated Universities
Upton, New York 11973

Chairman, Department of Nuclear Energy
A. N. Goland

DISTRIBUTION (cont'd.)

Department of Energy
Washington, D.C. 20545

Office of Fusion Energy (6)
J. F. Clarke, ETM
F. E. Coffman, ETM
N. A. Oavies, ETM
J. F. Decker, ETM
E. E. Kintner, ETM
M. Roberts, ETM

Materials and Radiation Effects Branch, ETM (25)

Assistant Director for Materials Technology, RRT (2)
J. W. Bennett
P. B. Hemmig

General Atomic Company (3)
P. O. Box 81608
San Oiego, California 92138

G. R. Hopkins
S. Rosenwasser
L. Rovner

Lawrence Livermore Laboratory (2)
University of California
P. O. Box 808
Livermore, California 94550

M. W. Guinan
C. M. Logan

Los Alamos Scientific Laboratory (3)
University of California
P. O. Box 1663
Los Alamos, New Mexico 87544

D. J. Dudziak
W. Green
D. M. Parkin

Massachusetts Institute of Technology (2)
Cambridge, Massachusetts 02139

O. K. Harling
K. C. Russell

McDonnell-Douglas Astronautics (2)
P. O. Box 516
St. Louis, Missouri 63166

J. Davis
D. Kurnner

Mound Laboratory (1)
P. O. Box 32
Miamisburg, Ohio 45342

Manager, Technology Applications and Development

Naval Research Laboratory (3)
Metallurgy Division, Code 6390
Washington, D. C. 20375

I. Manning
F. A. Smidt
J. A. Sprague

North Carolina State University (1)
Department of Nuclear Engineering
Raleigh, North Carolina 26707

J. R. Beeler, Jr.

Oak Ridge National Laboratory (6)
P. O. Box Y
Oak Ridge, Tennessee 37830

Director, Thermonuclear Division, Bldg. 9201-2
L. A. Berry
R. J. Colchin, Bldg. 9201-2
F. G. Perey
C. Weisbin

DISTRIBUTION (cont'd)

Plasma Physics Laboratory (3)
Princeton University
P. O. Box 451
Princeton, New Jersey 08540

C. Osgood
W. Price
K. Wakefield

Sandia Laboratories (2)
Albuquerque, New Mexico 87115

F. L. Vook

Sandia Laboratories (3)
Livermore, California 94550

W. Bauer (2)
W. Wilson

University of Michigan (1)
Nuclear Engineering Department
College of Engineering
Ann Arbor, Michigan 48105

T. Kammash

Westinghouse Electric Corporation (3)
Research and Development Center
Beulah Road
Pittsburgh, Pennsylvania 15234

J. Choyka
H. R. Holland
J. A. Spetznagel

*U.S. GOVERNMENT PRINTING OFFICE : 1979 0-281-704/40